Measurement of Picosecond Electron Bunches in a Linear Accelerator

Dissertation
zur Erlangung des Doktorgrades
des Fachbereichs Physik
der Universität Hamburg

vorgelegt von
Klaus Hanke
aus Bonn

Hamburg

1997

Gutachter der Dissertation:	Prof. Dr. P. Schmüser Priv. Doz. Dr. M. Tonutti
Gutachter der Disputation:	Prof. Dr. P. Schmüser Prof. Dr. E. Lohrmann
Datum der Disputation:	2. Dezember 1997
Dekan des Fachbereichs Physik und Vorsitzender des Promotionsausschusses:	Prof. Dr. B. Kramer

Abstract

Future high energy linear colliders require sophisticated diagnostic tools for measurement of beam size and position. Diagnostic devices have been developed according to these specifications. They form parts of the linear collider test facilities that are presently being commissioned or already operated in various high energy physics laboratories.
This thesis presents monitoring systems for the longitudinal charge distribution of the electron pulses. Since the specified short pulse lengths are at the limit of time resolving electronics, measuring techniques for the frequency domain have been developed. The experimental techniques are discussed and measurements presented.

Zusammenfassung

Zukünftige Hochenergie-Lineareollider erfordern anspruchsvolle Strahldiagnoseinstrumente für die Messung der Strahldimensionen sowie der Strahlposition. Diagnoseinstrumente wurden diesen Anforderungen entsprechend entwickelt. Sie bilden Teile der Linearcollider Testanlagen, die gegenwärtig in mehreren Hochernegiephysiklabors in Betrieb genommen oder bereits betrieben werden.
Diese Arbeit stellt Messanordnungen für die longitudinale Ladungsverteilung der Elektronenpulse vor. Da die angestrebten kurzen Pulslängen den Grenzbereich zeitauflösender Elektronik darstellen, wurden Messmethoden für den Frequenzraum entwickelt. Die experimentellen Techniken werden diskutiert und Messungen vorgestellt.

Contents

List of Figures

List of Tables

Introduction

With the operation of LEP[1] at a center of mass energy of 200 GeV, the limit for circular e^+e^- accelerators will be reached. In order to extend the physics of electron-positron annihilation to higher energies, the development of linear colliders is crucial.

Hadron colliders are well suited for explorative studies since they cover a wide energy range. However, to understand new physics and new particles, detailed studies at e^+e^- colliders are essential. A fine example is the discovery of the J/Ψ as narrow resonance J in hadron collisions in Brookhaven. Its interpretation as a charm-anticharm state Ψ was only possible due to detailed studies at e^+e^- storage rings.

Electron-positron annihilation has the immense advantage, that the parameters of the initial state are very well defined. Electrons can be considered as point-like particles down to 10^{-18} m. Their energy, polarization etc. can be measured with high precision. The event topology of e^+e^- collisions is simple compared to hadronic collisions. Hadrons consist of quarks and gluons. Their momentum is distributed among the constituents according to the structure functions. Hence the initial state is not well defined. In addition, proton-proton collisions produce an immense hadronic background. A typical event at the 14 TeV pp collider LHC[2] will contain several hundred hadronic tracks and, moreover, the high design luminosity of 10^{34} cm^2s^{-1} will result in the superposition of about 25 events per bunch crossing. The search for rare events is therefore an extremely difficult task.

While in the case of e^+e^- collisions the experiments and the analysis are much easier, here the accelerator itself is a very challenging project. Storage rings with a higher center of mass energy than LEP cannot be operated at reasonable costs, since losses due to synchrotron radiation increase dramatically. The alternative route was first proposed by M. Tigner in 1965 [1]: electrons and positrons from two linear accelerators are brought to head-on collision. This idea has been thoroughly studied during the last years by working groups all over the world. The

[1]Large Electron Positron Collider
[2]Large Hadron Collider

first working high energy e^+e^- linear collider was the SLC[3] machine which is presently running at a center of mass energy of 91 GeV. Building a machine with a center of mass energy of 500 GeV and a luminosity of 10^{33} cm^2 s^{-1} would be a first step towards TeV energies. Such a machine could be used for detailed studies of the top quark system, for finding or excluding the Higgs boson up to a mass of about 350 GeV and for the search for supersymmetric particles.

Various technical approaches to the problem of a high energy e^+e^- linear collider are presently being evaluated with respect to their feasibility at reasonable costs. They differ mainly in accelerating frequency, time structure and beam dimensions. Conventional, normalconducting accelerating structures such as the 3 GHz technology already used at SLC, can be extrapolated as proposed for the SBLC[4]. Higher frequencies are envisaged for the NLC[5], JLC[6] and VLEPP[7] machines. The wakefield accelerator CLIC[8] is to be operated at 30 GHz. The TESLA[9] design is the only linear accelerator based on superconducting cavities. Its accelerating frequency of 1.3 GHz is comparatively low [2].

Test facilities for linear accelerators are presently being commissioned or already operated in various high energy physics laboratories. The layout of these prototype linacs should resemble that of a future 500 GeV machine as closely as possible. Measuring the parameters of the electron beam will then show if the specifications can be achieved.

In addition to the high energy physics potential, some machine designs offer the possibility to drive a free-electron laser (FEL). Such a high-brillance X-ray source is proposed for example both for the TESLA test facility linac (TTFL) [3] as well as for the TESLA machine [2]. Beam parameters such as bunch dimensions, bunch charge and emittance are in this case even more important and the tolerances tighter than for the high energy physics option. If the beam does not fulfill these very strict requirements, a free-electron laser will not work at all.

Beam diagnostics has been developed for the TESLA test facility to determine the beam emittance, current, position and dimensions. These devices are installed at the TESLA test facility linac to monitor its performance. Some of the beam monitors themselves, for example the bunch length monitors, had to be developed and are therefore themselves subject to experiments.

[3]Stanford Linear Collider
[4]S-Band Linear Collider
[5]Next Linear Collider
[6]Japanese Linear Collider
[7]Vstrechnie (Colliding) Lineinye (Linear) Electron Positron Puchki (Beams)
[8]Compact Linear Collider
[9]TeV Energy Superconducting Linear Accelerator

One possibility to obtain information about the bunch size is the use of transition radiation. The optical part of its spectrum can be used to measure the transverse beam profile. As an example for its application to beam diagnostics, a setup for optical transition radiation at a particle accelerator is presented and some possible measurements are discussed.

To obtain the bunch length, time resolving techniques (streak cameras) can be used. For the short bunch length of an electron linear accelerator, the resolution limit of streak cameras is reached. If measurements in the time domain are no longer possible, a principally different measurement technique must be applied. The alternative is to measure in the frequency domain rather than in the time domain. This method is based on the fact that the long wavelength part of the radiation spectrum of a bunch carries the information about the bunch length and shape. This argument holds for wavelengths of the order of the bunch length and longer. The experimental problem is then the measurement of spectra in the long wavelength range. For bunches of a few picoseconds, the relevant part of the spectrum is found at wavelengths of several millimeters. For shorter bunches as proposed for FEL option, the wavelength range shifts to the far-infrared. Since spectroscopy becomes easier at shorter wavelengths, these methods work the better the shorter the bunches are.

In this thesis, transition radiation has been used for electron beam diagnostics. First the formalism for radiation processes due to a moving point charge as well as for a bunch of charged particles is developed. Quasi-optical techniques for electromagnetic radiation at wavelengths of several millimeters are presented. Two types of spectrometers for millimeter waves have been developed for use at the TESLA test facility linac. They are described in Chapter 3. Chapter 4 deals with the application of radiation in the optical frequency range for beam diagnostics. A setup was built in the DESY transfer line to evaluate the potential of transition radiation for optical diagnostics. Measurements of the transverse beam parameters are presented. Chapter 5 deals with the application of millimeter-wave radiation to beam diagnostics. These measurements refer to the longitudinal bunch dimension. Bunch length measurements carried out at the CLIC test facility at CERN, at the S-DALINAC facility in Darmstadt and at the TESLA test facility at DESY are presented.

Chapter 1

Radiation from Charged Particles

Electromagnetic radiation is emitted by charged particles under various circumstances. These various sorts of radiation, although similar in certain aspects, are due to entirely different physical processes and each of them requires specific formal treatment.

Synchrotron radiation is the only kind of radiation that can be emitted while the particle is travelling in vacuum. This happens only if the particle is accelerated. If a particle travels at constant speed in a homogeneous medium, Čerenkov radiation is the only form of radiation that can be emitted. This happens under the condition, that the velocity of the particle is larger than the phase velocity of light in the medium (Čerenkov condition). If the medium is not homogeneous or varies in time, transition radiation is emitted. This kind of radiation is due to boundary conditions at the interface of media with different dielectric properties.

1.1 Radiation from a Moving Point-Charge

Consider a point-charge e moving on an arbitrary trajectory $\mathbf{r}(\mathrm{t})$ at arbitrary velocity $\mathbf{v}(\mathrm{t})$ in a homogeneous and infinite medium with permittivity ε_r. The following treatment is based on the Liénard-Wiechert potentials for a moving point-charge that are derived in textbooks, e.g. [4]. We will only consider the case sketched in Fig. 1.1, where $\mathbf{r} \ll \mathbf{R}_0$ (far-field approximation):

$$R \approx R_0 - \mathbf{r} \cdot \mathbf{n}. \tag{1.1}$$

In this case, the vectors $\mathbf{E}$ and $\mathbf{H}$ at the observation point are transverse and the Poynting vector $\mathbf{S}$ is directed along $\mathbf{n}$:

$$\begin{aligned} \mathbf{S} &= \mathbf{E} \times \mathbf{H} \\ &= \frac{\sqrt{\mu_0}}{\sqrt{\varepsilon_0 \varepsilon_r}} \left|\mathbf{H}\right|^2 \mathbf{n}. \end{aligned} \tag{1.2}$$

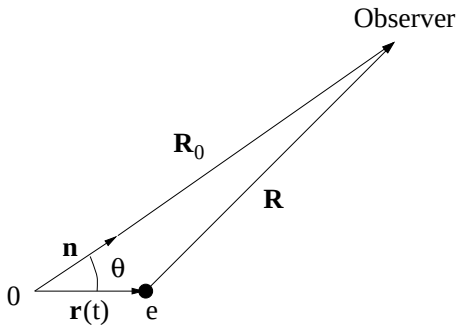

Figure 1.1: Notation used to derive the equations for radiation from a moving point-charge e.

The vector potential $\mathbf{A}$ is given by the Liénard-Wiechert potential[1]:

$$\mathbf{A}(\mathbf{r},t) = \left[\frac{\mu_0 ec\boldsymbol{\beta}}{4\pi(1-\sqrt{\varepsilon_r}\boldsymbol{\beta}\cdot\mathbf{n})R}\right]_{ret}. \tag{1.3}$$

It is convenient to consider the spectral decomposition of $\mathbf{A}(\mathbf{r},t)$:

$$\mathbf{A}(\omega) = \frac{\mu_0 ec}{8\pi^2}\int\left[\frac{\boldsymbol{\beta}}{(1-\sqrt{\varepsilon_r}\boldsymbol{\beta}\cdot\mathbf{n})R}\right]_{ret}\exp\{i\omega t\}dt. \tag{1.4}$$

We now make the substitution

$$\begin{aligned} t &= t' + \frac{R(t')}{c/\sqrt{\varepsilon_r}} \qquad (1.5)\\ \Rightarrow dt &= dt' + \frac{\sqrt{\varepsilon_r}}{c}\frac{dR(t')}{dt'}dt' \\ &= (1-\sqrt{\varepsilon_r}\boldsymbol{\beta}\cdot\mathbf{n})dt' \end{aligned}$$

and obtain using (1.1)

$$\mathbf{A}(\omega) = \frac{\mu_0 ec}{8\pi^2}\int\frac{\boldsymbol{\beta}}{R}\exp\{i(\omega t' + \frac{\omega\sqrt{\varepsilon_r}}{c}R_0 - \frac{\omega\sqrt{\varepsilon_r}}{c}\mathbf{r}\cdot\mathbf{n})\}dt'. \tag{1.6}$$

We can then make the simplification that the term $(R_0 - \mathbf{r}\cdot\mathbf{n})^{-1}$ varies very slowly compared to $\exp\{-i\frac{\omega\sqrt{\varepsilon_r}}{c}\mathbf{n}\cdot\mathbf{r}\}$:

$$\mathbf{A}(\omega) = \frac{\mu_0 ec}{8\pi^2}\frac{1}{R_0}\exp\{\frac{i\omega\sqrt{\varepsilon_r}}{c}R_0\}\int\boldsymbol{\beta}\exp\{i(\omega t' - \frac{\omega\sqrt{\varepsilon_r}}{c}\mathbf{n}\cdot\mathbf{r}(t'))\}dt'. \tag{1.7}$$

[1]The derivation is based on the vector potential for the magnetic field which makes the calculation more convenient than in the case of the electric field.

To simplify this expression we define the wave vector $\mathbf{k}$ by

$$\mathbf{k} = \frac{\omega\sqrt{\varepsilon_r}}{c}\mathbf{n} \tag{1.8}$$

and write t instead of t':

$$\mathbf{A}(\omega) = \frac{\mu_0 ec}{8\pi^2}\frac{\exp\{i\mathbf{k}\cdot\mathbf{R}_0\}}{R_0}\int \boldsymbol{\beta}\exp\{i(\omega t - \mathbf{k}\cdot\mathbf{r}(t))\}dt. \tag{1.9}$$

From this, $\mathbf{H}(\omega)$ can be obtained:

$$\begin{aligned}\mathbf{H}(\omega) &= \frac{1}{\mu_0}\nabla\times\mathbf{A}(\omega)\\ &= \frac{ec}{8\pi^2}\frac{\exp\{i\mathbf{k}\cdot\mathbf{R}_0\}}{R_0}\frac{i\omega\sqrt{\varepsilon_r}}{c}\int(\mathbf{n}\times\boldsymbol{\beta})\exp\{i(\omega t - \mathbf{k}\cdot\mathbf{r}(t))\}dt.\end{aligned} \tag{1.10}$$

We obtain then a general equation from which the radiated energy per unit frequency and unit solid angle for the various radiation processes can be calculated[2]:

$$\begin{aligned}\frac{d^2W}{d\omega d\Omega} &= SR^2\\ &= 4\pi\sqrt{\frac{\mu_0}{\varepsilon_r\varepsilon_0}}\left|\mathbf{H}(\omega)\right|^2 R^2\\ &= \frac{e^2\omega^2\sqrt{\varepsilon_r}}{16\pi^3\varepsilon_0 c}\left|\int(\mathbf{n}\times\boldsymbol{\beta})\exp\{i(\omega t - \mathbf{k}\cdot\mathbf{r}(t))\}dt\right|^2.\end{aligned} \tag{1.11}$$

Equation (1.11) is a fundamental equation for all radiation processes caused by a moving point-charge in the far-field approximation.

Starting from this, now the special case of uniform and linear motion with $\mathbf{r}(t) = \mathbf{v}t$ will be considered. Using

$$|\mathbf{n}\times\boldsymbol{\beta}| = \beta\sin\theta \tag{1.12}$$

and

$$\mathbf{k}\cdot\mathbf{r}(t) = \omega t(\beta\sqrt{\varepsilon_r}\cos\theta), \tag{1.13}$$

(1.11) can be written as

$$\frac{d^2W}{d\omega d\Omega} = \frac{e^2\omega^2\sqrt{\varepsilon_r}}{16\pi^3\varepsilon_0 c}\beta^2\sin^2\theta\left|\int\exp\{i\omega(1-\beta\sqrt{\varepsilon_r}\cos\theta)t\}dt\right|^2. \tag{1.14}$$

The integration boundaries have to be set according to the specific problem. Starting from (1.14) we will now consider various radiation processes in detail.

[2]Note, that only positive frequencies have a physical interpretation and therefore $\int_{-\infty}^{\infty}|\mathbf{H}|^2 dt = 4\pi\int_0^{\infty}|\mathbf{H}(\omega)|^2 d\omega$.

1.2 Čerenkov Radiation

Čerenkov radiation is the only kind of radiation that can be emitted by a charge with uniform and linear motion in a homogeneous, infinite medium.
The case of an infinite trajectory corresponds to evaluating the integral in (1.14) from -∞ to +∞:

$$\frac{d^2W}{d\omega d\Omega} = \frac{e^2\omega^2\sqrt{\varepsilon_r}}{16\pi^3\varepsilon_0 c}\beta^2\sin^2\theta \lim_{T\to\infty}\left|\int_{-T/2}^{+T/2}\exp\{i\omega(1-\beta\sqrt{\varepsilon_r}\cos\theta)t\}dt\right|^2. \quad (1.15)$$

For $|T| \to \infty$, the integral yields

$$2\pi T\omega^{-1}\delta(1-\beta\sqrt{\varepsilon_r}\cos\theta) \quad (1.16)$$

and the radiated power is given by

$$\frac{d^2P}{d\omega d\Omega} = \frac{e^2\omega\sqrt{\varepsilon_r}}{8\pi^2\varepsilon_0 c}\beta^2\sin^2\theta\ \delta(1-\beta\sqrt{\varepsilon_r}\cos\theta). \quad (1.17)$$

The delta function determines the Čerenkov angle:

$$\cos\theta = \frac{1}{\sqrt{\varepsilon_r}\beta}. \quad (1.18)$$

Radiation is only emitted if

$$v > \frac{c}{\sqrt{\varepsilon_r}}, \quad (1.19)$$

that is if the velocity of the particle is higher than the velocity of light in the medium (Čerenkov condition).

1.3 Transition Radiation

Transition radiation is emitted as a charged particle moves through or close to an inhomogeneous medium or if the medium varies in time. A purely formal derivation of the equations for transition radiation can be found in e.g. [5], [6], [7]. In order to provide a more intuitive physical derivation rather than solving Maxwell's equations with boundary conditions, the relevant formulas are here developed following [8].

1.3.1 Derivation of the Ginzburg-Frank Formulas

The here relevant case, that a point-charge moves from a medium with permittivity ε_r to vacuum ($\varepsilon_r = 1$) can be treated analytically (the inverse process follows directly as will be seen). We will in the following derivation assume that the

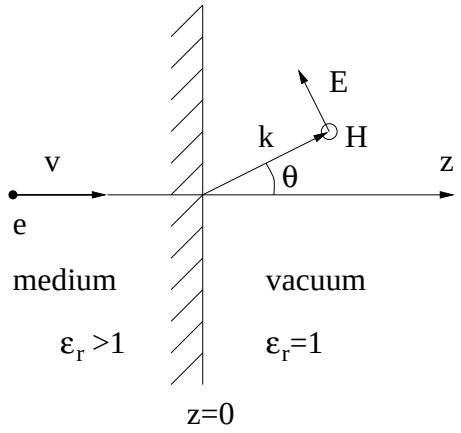

Figure 1.2: Point-charge e escaping from a medium with permittivity ε_r into vacuum ($\varepsilon_r = 1$). The emission of forward transition radiation is indicated by the wave vector $\mathbf{k}$ and the electric field vector $\mathbf{E}$. The observation point is in the vacuum at an angle θ with respect to the velocity of the particle. The problem is symmetric in $\mathbf{x}$ and $\mathbf{y}$.

velocity of the particle is uniform and linear and that the Čerenkov condition is not fulfilled. The velocity $\mathbf{v}$ of the charge is taken to be normal to the interface, say along the z-axis as sketched in Fig. 1.2.

It is convenient to treat the two half spaces seperately. The equations for the fields and the radiated energy have to be integrated from 0 to $+\infty$ for the right half space (vacuum) or from -∞ to 0 for the other half space (dielectric or metallic medium).

Let us consider the right half space in Fig. 1.2. The total magnetic field observed at a large distance is given by the superposition of three contributions:

$$\mathbf{H}(\omega) = \mathbf{H}_1(\omega) + \mathbf{H}_2(\omega) + \mathbf{H}_3(\omega). \tag{1.20}$$

As sketched in Fig. 1.3 and 1.4, $\mathbf{H}_1(\omega)$ is the magnetic field of the wave that is emitted into the vacuum after refraction at the interface, $\mathbf{H}_2(\omega)$ is the field of the wave directly emitted in the vacuum and $\mathbf{H}_3(\omega)$ is the field of the wave that is emitted in the vacuum and reaches the observation point after reflection at the interface.

$\mathbf{H}_2(\omega)$ can directly be obtained by integrating (1.10) from 0 to $+\infty$ with $\varepsilon_r = 1$:

$$\mathbf{H}_2(\omega) = \frac{e}{8\pi^2 c} \frac{\exp\{i\mathbf{k}_2 \cdot \mathbf{R}_0\}}{R_0} i\omega \int_0^\infty (\mathbf{n}_2 \times \mathbf{v}) \exp\{i(\omega - \mathbf{k}_2 \cdot \mathbf{v})t\} dt. \tag{1.21}$$

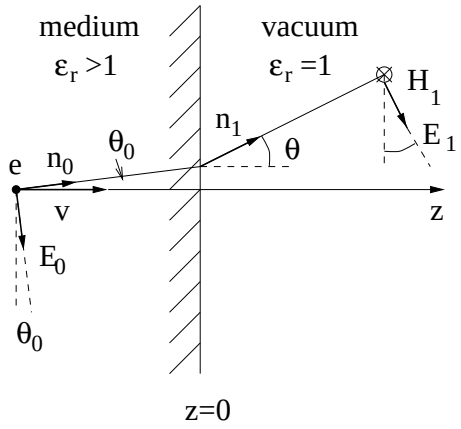

Figure 1.3: Magnetic and electric fields, that are emitted inside the medium and reach the observer in the vacuum after refraction at the interface.

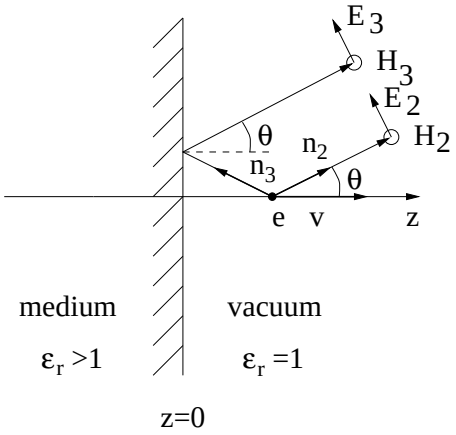

Figure 1.4: Fields contributing to the total intensity radiated into the vacuum half. $\mathbf{E}_2$ and $\mathbf{H}_2$ are directly emitted in the direction of the observer, $\mathbf{E}_3$ and $\mathbf{H}_3$ reach the observer after reflection at the interface.

The field $\mathbf{H}_3(\omega)$ is given by a corresponding expression multiplied with the reflection coefficient $r_\parallel$ for a magnetic field orientated in the plane of incidence:

$$\mathbf{H}_3(\omega) = r_\parallel \cdot \frac{e}{8\pi^2 c} \frac{\exp\{i\mathbf{k}_3 \cdot \mathbf{R}_0\}}{R_0} i\omega \int_0^\infty (\mathbf{n}_3 \times \mathbf{v}) \exp\{i(\omega - \mathbf{k}_3 \cdot \mathbf{v})t\} dt, \quad (1.22)$$

where

$$r_\parallel = \frac{\varepsilon_r \cos\theta - \sqrt{\varepsilon_r - \sin^2\theta}}{\varepsilon_r \cos\theta + \sqrt{\varepsilon_r - \sin^2\theta}}. \quad (1.23)$$

More care must be taken with the calculation of the field $\mathbf{H}_1$, which reaches the observer after refraction at the interface as sketched in Fig. 1.3.

We first calculate the electric field due to a moving charge in the vacuum. Its amplitude in the vacuum is given by

$$E = c\mu_0 H, \quad (1.24)$$

where $\mathbf{H}$ is given by

$$\mathbf{H}(\omega) = \frac{e}{8\pi^2 c} \frac{\exp\{i\mathbf{k}_2 \cdot \mathbf{R}_0\}}{R_0} i\omega \int_0^\infty -(\mathbf{n}_2 \times \mathbf{v}) \exp\{i(\omega - \mathbf{k}_2 \cdot \mathbf{v})t\} dt. \quad (1.25)$$

The electric field is emitted into the medium in direction of $-\mathbf{n}_2$, undergoing refraction at the interface. Its amplitude is obtained by multiplying the field in the vacuum with the Fresnel coefficient $t_\parallel/\sqrt{\varepsilon_r}$ for the transmitted magnetic field orientated perpendicular to the plane of incidence, where

$$t_\parallel = \frac{2\varepsilon_r \cos\Theta}{\varepsilon_r \cos\Theta + \sqrt{\varepsilon_r - \sin^2\Theta}} \quad (1.26)$$

and

$$1 + r_\parallel = t_\parallel. \quad (1.27)$$

The inverse process, that a moving charge inside the medium causes a field in the vacuum, can now be calculated using the reciprocity theorem [6]:
if $\mathbf{j}_A$ and $\mathbf{j}_B$ are current densities at points A and B, and $\mathbf{E}_A(B)$ is the field due to $\mathbf{j}_A$ at point B and vice versa, then we have

$$\int \mathbf{j}_A \mathbf{E}_B(A) dV_A = \int \mathbf{j}_B \mathbf{E}_A(B) dV_B. \quad (1.28)$$

For the problem discussed here, the current densities in the medium and in vacuum are

$$\mathbf{j}_A = \mathbf{j}_B = e\mathbf{v}. \quad (1.29)$$

We have calculated the amplitude of the electric field E_0 in the medium, and can therefore obtain the amplitude of the electric field E_1 at the observation point. Taking into account the angle of refraction we obtain

$$|\mathbf{E}_1| \sin\theta = |\mathbf{E}_0| \sin\theta', \tag{1.30}$$

where

$$\begin{aligned} |\mathbf{n}_0 \times \mathbf{v}| &= v \sin\theta' \\ |\mathbf{n}_1 \times \mathbf{v}| &= v \sin\theta. \end{aligned} \tag{1.31}$$

We obtain then the field $\mathbf{E}_1$ at the observation point. Using (1.24) the magnetic field $\mathbf{H}_1$ is given by

$$\mathbf{H}_1(\omega) = -\frac{t_\parallel}{\sqrt{\varepsilon_r}} \frac{e}{8\pi^2 c} \frac{\exp\{i\mathbf{k}_0 \cdot \mathbf{R}_0\}}{\mathbf{R}_0} i\omega \int_0^\infty (\mathbf{n}_1 \times \mathbf{v}) \exp\{i(\omega - \mathbf{k}_0 \cdot \mathbf{v})t\} dt. \tag{1.32}$$

We have now calculated all three fields that contribute to the total magnetic field. From the total magnetic field, the radiated energy per unit frequency and unit solid angle is obtained according to (1.11):

$$\begin{aligned} \frac{d^2W}{d\omega d\Omega} &= \frac{4\pi}{\sqrt{\varepsilon_r}\varepsilon_0 c} \left|\mathbf{H}_1(\omega) + \mathbf{H}_2(\omega) + \mathbf{H}_3(\omega)\right|^2 R^2 \\ &= \frac{e^2\beta^2 \sin^2\theta}{16\pi^3 \varepsilon_0 c} \left| \frac{1}{1-\beta\cos\theta} + \frac{r_\parallel}{1+\beta\cos\theta} - \frac{t_\parallel}{\varepsilon_r} \frac{1}{1-\beta\sqrt{\varepsilon_r - \sin^2\theta}} \right|^2 . \end{aligned} \tag{1.33}$$

Using the expressions for the Fresnel coefficients as given above, one obtains for the intensity radiated into the right half space (vacuum):

$$\frac{d^2W}{d\omega d\Omega} = \frac{e^2\beta^2}{4\pi^3\varepsilon_0 c} \frac{\sin^2\theta\cos^2\theta}{(1-\beta^2\cos^2\theta)^2} \left| \frac{(\varepsilon_r - 1)(1 - \beta^2 - \beta\sqrt{\varepsilon_r - \sin^2\theta})}{(\varepsilon_r \cos\theta + \sqrt{\varepsilon_r - \sin^2\theta})(1 - \beta\sqrt{\varepsilon_r - \sin^2\theta})} \right|^2 . \tag{1.34}$$

Here, θ is the angle between $\mathbf{v}$ and $\mathbf{k}$, such that $\theta = 0$ corresponds to radiation directed along the positive z-axis. The radiation emitted into the half space which the particle is entering is called forward transition radiation.

The corresponding relation for the case of a point charge entering a medium from vacuum is simply obtained by replacing β by -β as sketched in Fig. 1.5. The radiation emitted into the vacuum is then given by

$$\frac{d^2W}{d\omega d\Omega} = \frac{e^2\beta^2}{4\pi^3\varepsilon_0 c} \frac{\sin^2\theta\cos^2\theta}{(1-\beta^2\cos^2\theta)^2} \left| \frac{(\varepsilon_r - 1)(1 - \beta^2 + \beta\sqrt{\varepsilon_r - \sin^2\theta})}{(\varepsilon_r \cos\theta + \sqrt{\varepsilon_r - \sin^2\theta})(1 + \beta\sqrt{\varepsilon_r - \sin^2\theta})} \right|^2 , \tag{1.35}$$

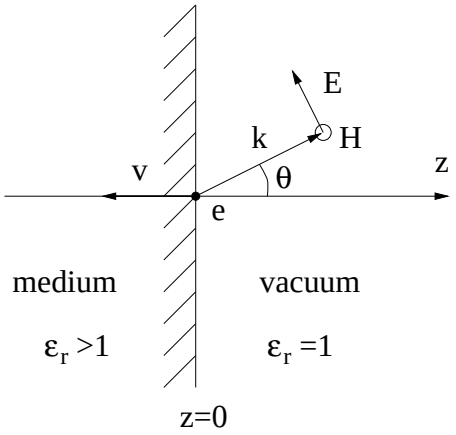

Figure 1.5: Point-charge e entering a medium with permittivity ε_r from vacuum ($\varepsilon_r = 1$). Backward transition radiation is emitted into the vacuum at an angle θ between $\mathbf{k}$ and the negative velocity of the particle. The problem is symmetric in $\mathbf{x}$ and $\mathbf{y}$.

where θ is now the angle between -$\mathbf{v}$ and $\mathbf{k}$.

Equations (1.34) and (1.35) are known as the Ginzburg-Frank formulas for transition radiation at the interface between an arbitrary medium and vacuum. Transition radiation is also emitted into the medium. The corresponding equations can be obtained by exchanging the two media in the preceding derivation while leaving the direction of the $\mathbf{v}$ unchanged.

Some conclusions can be drawn so far. Transition radiation is produced both due to the entry process from vacuum into a medium and due to the exit process from a medium into vacuum. From either process, both forward and backward transition radiation are produced. The spectral composition of the radiation is determined by the value of $\varepsilon_r(\omega)$. The radiated intensity is proportional to $|\varepsilon_r - 1|^2$.[3] The more the dielectric function of the medium differs from $\varepsilon_r = 1$, the more transition radiation is emitted. Transition radiation is polarized with the electric vector lying in the plane defined by $\mathbf{k}$ and $\mathbf{v}$ (observation plane).

1.3.2 Special Case: Interface Vacuum-Metal

Based on the general formalism, we will now discuss some special cases of the Ginzburg-Frank formulas. In particular, we will restrict the discussion to the case of the interface between vacuum and a metal.

[3] In the most general case of two arbitrary media, the radiated intensity is proportional to $|\varepsilon_{r1} - \varepsilon_{r2}|^2$. The more the dielectric functions differ, the more transition radiation is emitted.

The dielectric function of a metal depends on the frequency range of interest. For frequencies not higher than in the optical range, in general metals can be regarded as perfect conductors with $\varepsilon_r = \infty$. This formula can be applied for the here relevant optical and lower frequencies. Since these waves do not propagate in a metal, they are only emitted into vacuum.

For higher frequencies, ε_r must be obtained from

$$\varepsilon_r = 1 - \frac{\omega_p^2}{\omega^2} \tag{1.36}$$

where ω_p is the plasma frequency of the metal.

In the following sections, only frequencies for which the metal is a perfect conductor will be considered.

1.3.3 Normal Incidence: Non-Relativistic Limit

In the non-relativistic limit ($\beta \ll 1$ and $\beta \ll 1/\sqrt{\varepsilon_r}$), one obtains from (1.33) and (1.27)

$$\frac{d^2W}{d\omega d\Omega} = \frac{e^2\beta^2}{16\pi^3\varepsilon_0 c}\sin^2\theta \left|\frac{t_\parallel}{\varepsilon_r}(1-\varepsilon_r)\right|^2. \tag{1.37}$$

The radiation from the entry process into a medium and from the exit process into vaccuum is identical. For the special case of a metal-vacuum interface and frequencies, for which the metal is a perfect conductor, (1.37) becomes

$$\frac{d^2W}{d\omega d\Omega} = \frac{e^2\beta^2\sin^2\theta}{4\pi^3\varepsilon_0 c}. \tag{1.38}$$

1.3.4 Normal Incidence: Ultrarelativistic Limit

We will now consider the ultrarelativistic limit ($\beta \approx 1$). To simplify the discussion, we again consider the case $\varepsilon_r = \infty$. For small angles θ, equation (1.33) simplifies to

$$\frac{d^2W}{d\omega d\Omega} = \frac{e^2\beta^2}{16\pi^3\varepsilon_0 c}\frac{\sin^2\theta}{(1-\beta\cos\theta)^2}. \tag{1.39}$$

The corresponding expression for the transition from vacuum into a medium is given by

$$\frac{d^2W}{d\omega d\Omega} = \left|r_\parallel\right|^2 \frac{e^2\beta^2}{16\pi^3\varepsilon_0 c}\frac{\sin^2\theta}{(1-\beta\cos\theta)^2} \tag{1.40}$$

and differs from (1.39) only by the reflectivity $R_\parallel = \left|r_\parallel\right|^2$. For $\varepsilon_r = \infty$, we have $R_\parallel = 1$ and the radiation from both processes is again identical.

In the ultrarelativistic case, the radiation has its maximum at angles

$$\theta \approx \frac{1}{\gamma} = \sqrt{1-\beta^2}. \tag{1.41}$$

We can therefore write

$$\begin{aligned} \sin^2\theta &\approx \theta^2 \\ \cos^2\theta &\approx 1 - \frac{\theta^2}{2} \end{aligned} \tag{1.42}$$

and obtain from (1.39) for the radiated energy

$$\frac{d^2W}{d\omega d\Omega} = \frac{e^2\beta^2}{4\pi^3\varepsilon_0 c}\frac{\theta^2}{[\theta^2+(1-\beta^2)]^2}. \tag{1.43}$$

Integrating over the solid angle yields the total emitted energy per unit frequency [6]:

$$\frac{dW}{d\omega} = \frac{e^2}{4\pi^2\varepsilon_0 c}\ln\frac{1}{1-\beta^2}. \tag{1.44}$$

1.3.5 Oblique Incidence on a Single Surface

So far, we have discussed the case where the particle trajectory is normal to the interface. We will now consider the case, where the particle moves through an interface at an arbitrary angle. Without loss of generality, we can let the particle trajectory be inclined by an angle ψ with respect to the z-axis as sketched in Fig. 1.6.

The plane of incidence is defined by $\mathbf{v}$ and the vector normal to the interface. The observation plane is defined as before by $\mathbf{n}$ and the vector normal to the interface. The calculation is done as before, but we have now to calculate the components parallel and perpendicular to the observation plane separately:

$$\frac{d^2W}{d\omega d\Omega} = \left(\frac{d^2W}{d\omega d\Omega}\right)_{\parallel} + \left(\frac{d^2W}{d\omega d\Omega}\right)_{\perp}. \tag{1.45}$$

In general, the parallel and perpendicular components are not equal and the total radiation seen at the observation point is elliptically polarized.

We consider the projection of the vectors on the observation plane as sketched in Fig. 1.7. For the component parallel to the observation plane we obtain the expression

$$\left(\frac{d^2W}{d\omega d\Omega}\right)_{\parallel} = \frac{e^2}{16\pi^3\varepsilon_0 c}\left|\frac{\boldsymbol{\beta}_{\parallel}\times\mathbf{n}_2}{1-\boldsymbol{\beta}\cdot\mathbf{n}_2} + r_{\parallel}\frac{\boldsymbol{\beta}_{\parallel}\times\mathbf{n}_3}{1-\boldsymbol{\beta}\cdot\mathbf{n}_3} - \frac{t_{\parallel}}{\sqrt{\varepsilon_r}}\frac{\boldsymbol{\beta}_{\parallel}\times\mathbf{n}_1}{1-\boldsymbol{\beta}\cdot\mathbf{n}_1\sqrt{\varepsilon_r}}\right|^2, \tag{1.46}$$

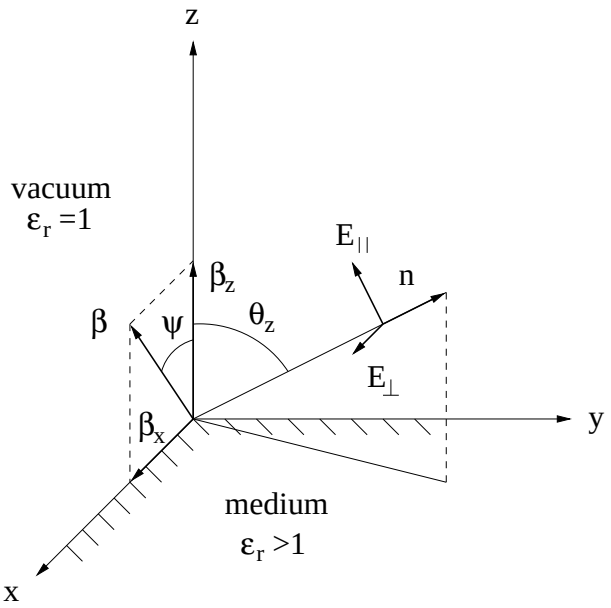

Figure 1.6: Particle travelling from a medium into vacuum. The particle trajectory is inclined by an angle ψ with respect to the z-axis.

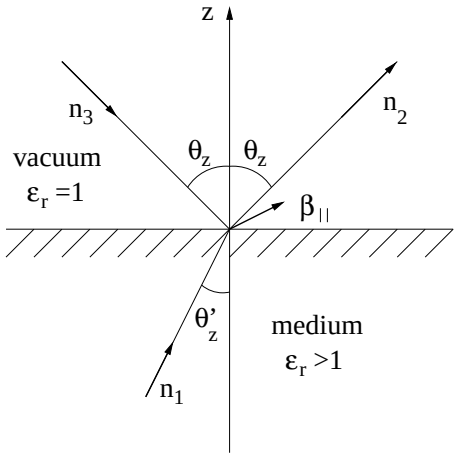

Figure 1.7: Projection of the vectors $\mathbf{n}_1$, $\mathbf{n}_2$, $\mathbf{n}_3$ and β in the observation plane.

where $\beta_\parallel$ is the projection of β in the observation plane. The Fresnel coefficients are given by (1.23), (1.26) and (1.27), where we have to write θ_z instead of θ.

The component perpendicular to the observation plane is given by

$$\left(\frac{d^2W}{d\omega d\Omega}\right)_\perp = \frac{e^2}{16\pi^3\varepsilon_0 c}\beta_\perp^2 \left| \frac{1}{1-\boldsymbol{\beta}\cdot\mathbf{n}_2} r_\perp + \frac{1}{1-\boldsymbol{\beta}\cdot\mathbf{n}_3} - \frac{t_\perp}{\sqrt{\varepsilon_r}} \frac{1}{1-\boldsymbol{\beta}\cdot\mathbf{n}_1\sqrt{\varepsilon_r}} \right|^2 \tag{1.47}$$

with

$$r_\perp = \frac{\cos\theta_z - \sqrt{\varepsilon_r - \sin^2\theta_z}}{\cos\theta_z + \sqrt{\varepsilon_r - \sin^2\theta_z}}, \tag{1.48}$$

$$t_\perp = \frac{2\sqrt{\varepsilon_r}\cos\theta_z}{\cos\theta_z + \sqrt{\varepsilon_r - \sin^2\theta_z}}, \tag{1.49}$$

$$1 + r_\perp = \frac{t_\perp}{\sqrt{\varepsilon_r}}. \tag{1.50}$$

Equations (1.46) and (1.47) are the general expressions for oblique incidence. For $\beta_\perp = 0$ and $\beta_\parallel = \beta$ they yield again the Ginzburg-Frank formulas for normal incidence derived before.

1.3.6 Oblique Incidence: Non-Relativistic Limit

Neglecting the terms $(\boldsymbol{\beta}\cdot\mathbf{n}_1)$, $(\boldsymbol{\beta}\cdot\mathbf{n}_2)$ and $(\boldsymbol{\beta}\cdot\mathbf{n}_3)$ in (1.46) yields

$$\begin{aligned} \left(\frac{d^2W}{d\omega d\Omega}\right)_\parallel &= \frac{e^2}{16\pi^3\varepsilon_0 c}\left|\boldsymbol{\beta}_\parallel \times (\mathbf{n}_2 + r_\parallel \mathbf{n}_3 - \frac{t_\parallel}{\sqrt{\varepsilon_r}}\mathbf{n}_1)\right|^2 \\ \left(\frac{d^2W}{d\omega d\Omega}\right)_\perp &= 0. \end{aligned} \tag{1.51}$$

We can as well write (1.51) as

$$\begin{aligned} \frac{d^2W}{d\omega d\Omega} = \left(\frac{d^2W}{d\omega d\Omega}\right)_\parallel &= \frac{e^2}{16\pi^3\varepsilon_0 c}\beta_z^2\sin^2\theta_z \left|1 + r_\parallel - \frac{t_\parallel}{\sqrt{\varepsilon_r}}\right|^2 \\ &= \frac{e^2}{4\pi^3\varepsilon_0 c}\beta_z^2|\varepsilon_r - 1|^2 \frac{\sin^2\theta\cos^2\theta}{|\varepsilon_r\cos\theta + \sqrt{\varepsilon_r - \sin^2\theta}|^2}. \end{aligned} \tag{1.52}$$

For $\varepsilon_r = \infty$, we obtain again

$$\frac{d^2W}{d\omega d\Omega} = \frac{e^2\beta_z^2\sin^2\theta}{4\pi^3\varepsilon_0 c}. \tag{1.53}$$

Writing β instead of β_z, this is the same result as obtained for normal incidence in the non-relativistic limit. The radiation from the entry and the exit process is identical.

1.3.7 Oblique Incidence: Ultrarelativistic Limit

Again, we consider the case $\varepsilon_r = \infty$. We have to treat the transition from the medium into vacuum and the inverse process separately.

Neglecting the second and third term in (1.46) and (1.47) leads to

$$\begin{aligned}\left(\frac{d^2W}{d\omega d\Omega}\right)_{\parallel} &= \frac{e^2}{16\pi^3\varepsilon_0 c}\left(\frac{\boldsymbol{\beta}_{\parallel}\times\mathbf{n}_2}{1-\boldsymbol{\beta}\cdot\mathbf{n}_2}\right)^2\\ \left(\frac{d^2W}{d\omega d\Omega}\right)_{\perp} &= \frac{e^2}{16\pi^3\varepsilon_0 c}\left(\frac{\boldsymbol{\beta}_{\perp}\times\mathbf{n}_2}{1-\boldsymbol{\beta}\cdot\mathbf{n}_2}\right)^2.\end{aligned} \tag{1.54}$$

The total intensity is given by

$$\begin{aligned}\frac{d^2W}{d\omega d\Omega} &= \left(\frac{d^2W}{d\omega d\Omega}\right)_{\parallel}+\left(\frac{d^2W}{d\omega d\Omega}\right)_{\perp}\\ &= \frac{e^2}{16\pi^3\varepsilon_0 c}\frac{(\boldsymbol{\beta}_{\parallel}\times\mathbf{n}_2)^2+(\boldsymbol{\beta}_{\perp}\times\mathbf{n}_2)^2}{(1-\boldsymbol{\beta}\cdot\mathbf{n}_2)^2}\\ &= \frac{e^2}{16\pi^3\varepsilon_0 c}\frac{(\boldsymbol{\beta}\times\mathbf{n}_2)^2}{(1-\boldsymbol{\beta}\cdot\mathbf{n}_2)^2}.\end{aligned} \tag{1.55}$$

The radiated energy is in this approximation independent of the angle of incidence and of the permittivity of the medium.

For the transition from the vacuum into the metal, we obtain a different result. In equations (1.46) and (1.47), the second term becomes most important since $(\boldsymbol{\beta}\cdot\mathbf{n}_3)$ is close to unity. This has the important consequence, that the most of the radiation is emitted at the angle of reflection. We obtain

$$\begin{aligned}\left(\frac{d^2W}{d\omega d\Omega}\right)_{\parallel} &= \frac{e^2}{16\pi^3\varepsilon_0 c}\left|r_{\parallel}\frac{\boldsymbol{\beta}_{\parallel}\times\mathbf{n}_3}{1-\boldsymbol{\beta}\cdot\mathbf{n}_3}\right|^2\\ \left(\frac{d^2W}{d\omega d\Omega}\right)_{\perp} &= \frac{e^2}{16\pi^3\varepsilon_0 c}\beta_{\perp}^2\left|r_{\perp}\frac{1}{1-\boldsymbol{\beta}\cdot\mathbf{n}_3}\right|^2.\end{aligned} \tag{1.56}$$

The total intensity is given by

$$\begin{aligned}\frac{d^2W}{d\omega d\Omega} &= \left(\frac{d^2W}{d\omega d\Omega}\right)_{\parallel}+\left(\frac{d^2W}{d\omega d\Omega}\right)_{\perp}\\ &= \frac{e^2}{16\pi^3\varepsilon_0 c}\left[R_{\parallel}\left(\frac{\boldsymbol{\beta}\times\mathbf{n}_3}{1-\boldsymbol{\beta}\cdot\mathbf{n}_3}\right)^2+\frac{\beta_{\perp}^2(R_{\perp}-R_{\parallel})}{(1-\boldsymbol{\beta}\cdot\mathbf{n}_3)^2}\right].\end{aligned} \tag{1.57}$$

Note, that for normal incidence ($R_{\perp} = R_{\parallel}$), the same result is obtained as before (1.40).

1.3.8 Transition Radiation from a Foil

Finally we will consider the case of a metal foil in vacuum, that is the case of two parallel surfaces. The problem can be treated by deriving the general formulas as done for a single surface before. The formalism becomes exceedigly complicated since multiple reflections at the interfaces must be taken into account [7].

Again, we will consider the case of a metal foil in vacuum and frequencies not higher than in the optical range. In this case, no radiation can propagate inside the foil. The entry and the exit process are completely independent and the formulas obtained for a single interface can be applied.

Figure 1.8 shows the emission of transition radiation for the case of normal incidence on a perfectly conducting foil. Backward transition radiation from the entry process of the particle into the foil is emitted centered around the negative z-axis. Forward transition radiation from the exit process out of the foil is emitted centered around the positive z-axis.

Figure 1.9 shows the very important case where the foil is inclined with respect to the particle trajectory. While the direction of the forward transition remains unchanged, backward transition radiation is now emitted at the angle of reflection. For an angle of 45^o with respect to the particle trajectory, backward transition radiation is emitted at 90^o with respect to $\mathbf{v}$. This allows to separate the radiation from the electron beam and make use of it for all sort of measurements.

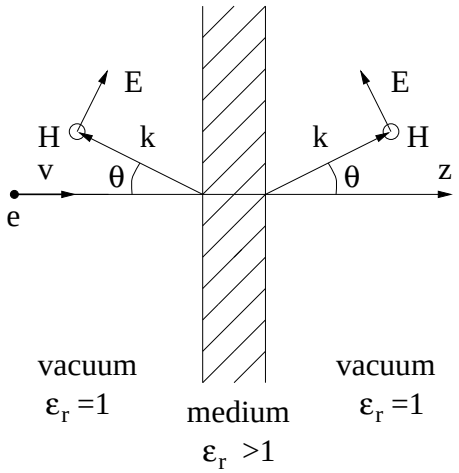

Figure 1.8: Transition radiation from a metal foil surrounded by vacuum. The foil is normal to the particle trajectory. Forward transition radiation is centered around the positive z-axis and backward transition radiation is centered around the negative z-axis.

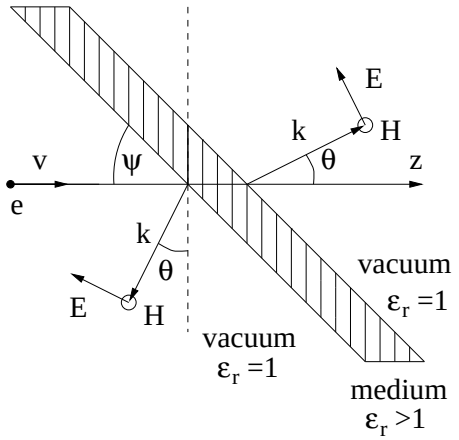

Figure 1.9: Transition radiation from a metal foil surrounded by vacuum. The foil is inclined by an angle ψ with respect to the particle trajectory. Forward transition radiation is still centered around the positive z-axis while backward transition radiation is now centered around the angle of reflection.

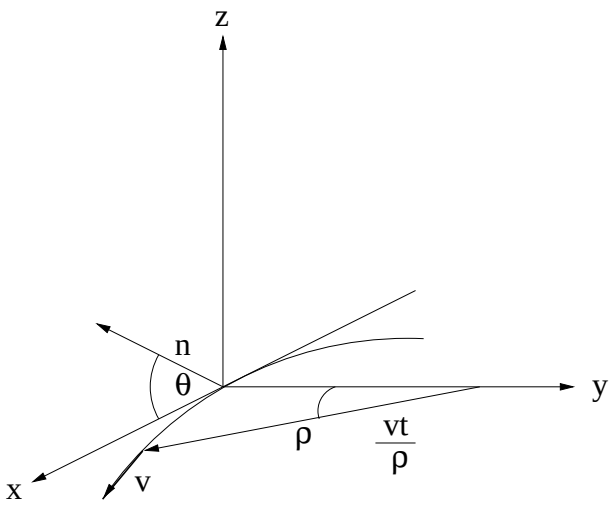

Figure 1.10: Notation used do derive the formalism for synchrotron radiation.

1.4 Synchrotron Radiation

We will now consider the case, where a point-charge is travelling in vacuum. If the particle is travelling linearily at constant speed, no radiation process is possible. If the particle is moving on a non-linear trajectory, synchrotron radiation is emitted.

We start again from the general equation for the radiation field of a point charge moving on an arbitrary trajectory (1.11). We will restrict the discussion to a circular orbit with radius of curvature ρ (Fig.1.10). We further use the approximation that the particle is moving at $\beta \approx 1$, and therefore the radiation is emitted at small angles $\theta \approx 1/\gamma$. The observer sees a radiation pulse during the short time $t \approx \rho/(c\gamma)$. The evaluation of the integral in the general equation (1.11) is complicated and can be found in e.g. [4], [9]. The radiated energy per unit frequency and unit solid angle is

$$\frac{d^2W}{d\omega d\Omega} = \frac{e^2}{3\pi^2\varepsilon_0 c}\left(\frac{\omega\rho}{c}\right)^2\left(\frac{1}{\gamma^2}+\theta^2\right)^2\left[K_{2/3}^2(\xi)+\frac{\theta^2}{(1/\gamma^2)+\theta^2}K_{1/3}^2(\xi)\right]. \quad (1.58)$$

Here, $K_{2/3}^2(\xi)$ and $K_{1/3}^2(\xi)$ are modified Bessel functions. The first term in the brackets corresponds to radiation polarized in the plane of deflection, the second term corresponds to radiation polarized perpendicular to the plane of deflection. From the properties of the Bessel functions one can conclude, that the radiation is mainly found in the plane of deflection. It is sharply peaked at a small angle in forward direction. The radiated energy scales with γ^4.

The total power emitted by an ultrarelativistic electron on a circular trajectory

is given by [10]

$$P_0 = \frac{1}{4\pi\varepsilon_0}\frac{2}{3}\frac{ce^2\gamma^4}{\rho^2}. \tag{1.59}$$

The spectral distribution is given by

$$\frac{dP}{d\omega} = \frac{P_0}{\omega_c} S\left(\frac{\omega}{\omega_c}\right) \tag{1.60}$$

where the critical frequency is defined by

$$\omega_c = \frac{3}{2}\frac{c\gamma^3}{\rho} \tag{1.61}$$

and the function $S\left(\frac{\omega}{\omega_c}\right)$ by

$$S\left(\frac{\omega}{\omega_c}\right) = \frac{9\sqrt{3}}{8\pi}\left(\frac{\omega}{\omega_c}\right)\int_{\omega/\omega_c}^{\infty} K_{5/3}(\xi)d\xi. \tag{1.62}$$

1.5 Multiparticle Coherence Effects

In the previous sections we have developed equations for the radiated intensity emitted by a single particle due to various processes. At particle accelerators, large numbers of particles are accumulated in bunches. This can lead to coherence effects at wavelengths that exceed the bunch size. The arguments developed here hold for any kind of radiation.

1.5.1 Multiparticle Coherence Calculations

We will denote the radiation intensity emitted by a single electron at a wavelength λ by $I_1(\lambda)$ and the intensity emitted by a bunch of N particles by $I_{tot}(\lambda)$. In order to obtain the total radiation emitted by a bunch of N particles, the radiated intensity of each single particle has to be summarized. In a naive treatment, the result is simply

$$I_{tot}(\lambda) = NI_1(\lambda). \tag{1.63}$$

In a full calculation however, the fields of the single particles have to be summed paying attention to the phase [11],[12],[13]. Figure 1.11 shows the notation used for the following derivation. We consider a symmetric bunch centered at $r = 0$. The distance between the center of the bunch and the detector is R. We assume that the relative position of the electrons does not change during the emission. The electric field from the j^{th} electron seen by the detector is given by

$$E_j(\lambda) = E_0(\lambda) \exp\{2\pi i \mathbf{n}_j \cdot \mathbf{r}_j/\lambda\}, \tag{1.64}$$

where $E_0(\lambda)$ is the field due to a reference electron at $r = 0$ and $\mathbf{n}_j$ is the unit vector directed from the detector to the j^{th} electron. Summing over all electrons in the bunch yields

$$E_{tot}(\lambda) = E_1(\lambda) \sum_{j=1}^{N} \exp\{2\pi i \mathbf{n}_j \cdot \mathbf{r}_j/\lambda\} \tag{1.65}$$

and hence the total emitted intensity is given by

$$I_{tot}(\lambda) = I_1(\lambda) \left| \sum_{j=1}^{N} \exp\{2\pi i \mathbf{n}_j \cdot \mathbf{r}_j/\lambda\} \right|^2 . \tag{1.66}$$

We can rewrite the squared sum as

$$\begin{aligned} I_{tot}(\lambda) &= I_1(\lambda) \sum_{j=1}^{N} \exp\{2\pi i \mathbf{n}_j \cdot \mathbf{r}_j/\lambda\} \sum_{k=1}^{N} \exp\{-2\pi i \mathbf{n}_k \cdot \mathbf{r}_k/\lambda\} \\ &= I_1(\lambda) \sum_{\substack{j,k=1 \\ j=k}}^{N} \exp\{2\pi i(\mathbf{n}_j \cdot \mathbf{r}_j - \mathbf{n}_k \cdot \mathbf{r}_k)/\lambda\} + \sum_{\substack{j,k=1 \\ j\neq k}}^{N} \exp\{2\pi i(\mathbf{n}_j \cdot \mathbf{r}_j - \mathbf{n}_k \cdot \mathbf{r}_k)/\lambda\} \end{aligned}$$

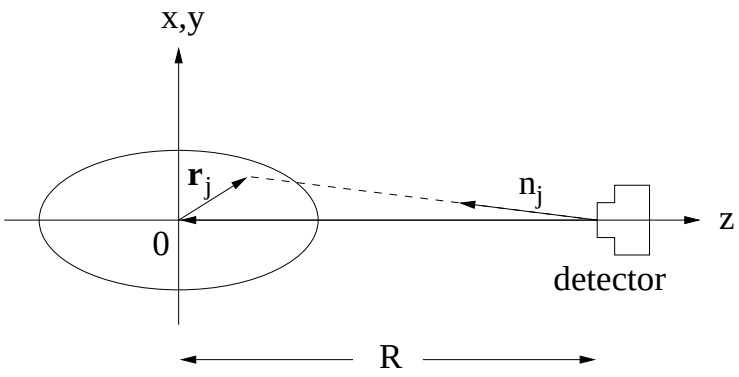

Figure 1.11: Coherent radiation from an extended electron bunch.

$$= I_1(\lambda)N + \sum_{\substack{j,k=1 \\ j\neq k}}^{N} \exp\{2\pi i(\mathbf{n}_j \cdot \mathbf{r}_j - \mathbf{n}_k \cdot \mathbf{r}_k)/\lambda\}. \tag{1.67}$$

We can also write (1.67) as

$$I_{tot}(\lambda) = I_1(\lambda)[N + N(N-1)f(\lambda)], \tag{1.68}$$

where we define

$$f(\lambda) = \frac{1}{N(N-1)} \sum_{\substack{j,k=1 \\ j\neq k}}^{N} \exp\{2\pi i(\mathbf{n}_j \cdot \mathbf{r}_j - \mathbf{n}_k \cdot \mathbf{r}_k)/\lambda\}. \tag{1.69}$$

For a large number of particles ($N \to \infty$), $f(\lambda)$ can be derived from a continuous particle density $S(\mathbf{r})$ and then be expressed by the Fourier integral

$$f(\lambda) = \left| \int S(\mathbf{r}) \exp\{2\pi i \mathbf{n} \cdot \mathbf{r}/\lambda\} dr \right|^2. \tag{1.70}$$

$f(\lambda)$ is hence given by the Fourier transform of the charge distribution function squared. The distribution function $S(r)$ is symmetric about $\mathbf{r} = 0$,

$$S(\mathbf{r}) = S(-\mathbf{r}), \tag{1.71}$$

and normalized such that

$$\int_{-\infty}^{+\infty} = S(\mathbf{r}) d^3r = 1. \tag{1.72}$$

The factor $f(\lambda)$ is called the bunch form factor. For wavelengths larger than the bunch length, the form factor approaches unity. In this limit, the particles in the bunch radiate coherently and the whole bunch behaves as a macro-particle with

charge Ne. The radiated intensity in this wavelength range scales with $(Ne)^2$. For wavelengths much smaller than the charge distribution, the form factor approaches zero and the particles radiate incoherently. The radiated intensity in this part of the spectrum scales with Ne^2. The coherent part of the spectrum therefore carries information about the charge distribution and is strongly enhanced compared to the incoherent part.

If R is much larger than the bunch size and for a cylindric symmetric bunch, (1.70) simplifies to

$$f(\lambda) = \left| \int S(\mathbf{r}) \exp\{2\pi i \mathbf{n} \cdot \mathbf{z}/\lambda\} dz \right|^2 . \tag{1.73}$$

In this approximation, for a transversely symmetric beam, the bunch form factor depends only on the longitudinal charge distribution in the bunch.

1.5.2 Influence of Transverse Beam Dimensions

No radiation is emitted in the exact forward direction. It is therefore always necessary to observe the radiation at a finite angle θ. In this case the transverse beam dimensions contribute to the form factor. For a cylindrical bunch of radius ρ and length l, the form factor is given by

$$f(\lambda) = 4 \left[\frac{J_1(2\pi\rho \sin(\theta/\lambda)}{2\pi\rho \sin(\theta/\lambda)} \frac{\sin \pi l \cos(\theta/\lambda)}{\pi l \cos(\theta/\lambda)} \right]^2 , \tag{1.74}$$

where J_1 is the first-order Bessel function. For $\theta = 0$ the form factor is given by the function $\sin(x)/x$. For large angles or large transverse beam size, the measured bunch length is longer than the actual one. The effect of the transverse bunch dimensions can be neglected if the condition

$$\frac{2\pi\rho \tan\theta}{3.38} \ll l \tag{1.75}$$

is fulfilled [14].

1.5.3 Application to Specific Charge Distributions

The coherent spectra of some analytic distribution functions are calculated in order to illustrate their dependence on bunch length and shape. Figure 1.12 shows in the upper part various charge distributions and in the lower part the normalized coherent spectra. A flat charge distribution results in a $sin(x)/x$-shaped spectrum, a Gaussian distribution results again in a Gaussian spectrum and a triangular distribution results in a $(sin(x)/x)^2$-shaped spectrum. All these spectra are similar in the width of the first maximum and in the first minimum.

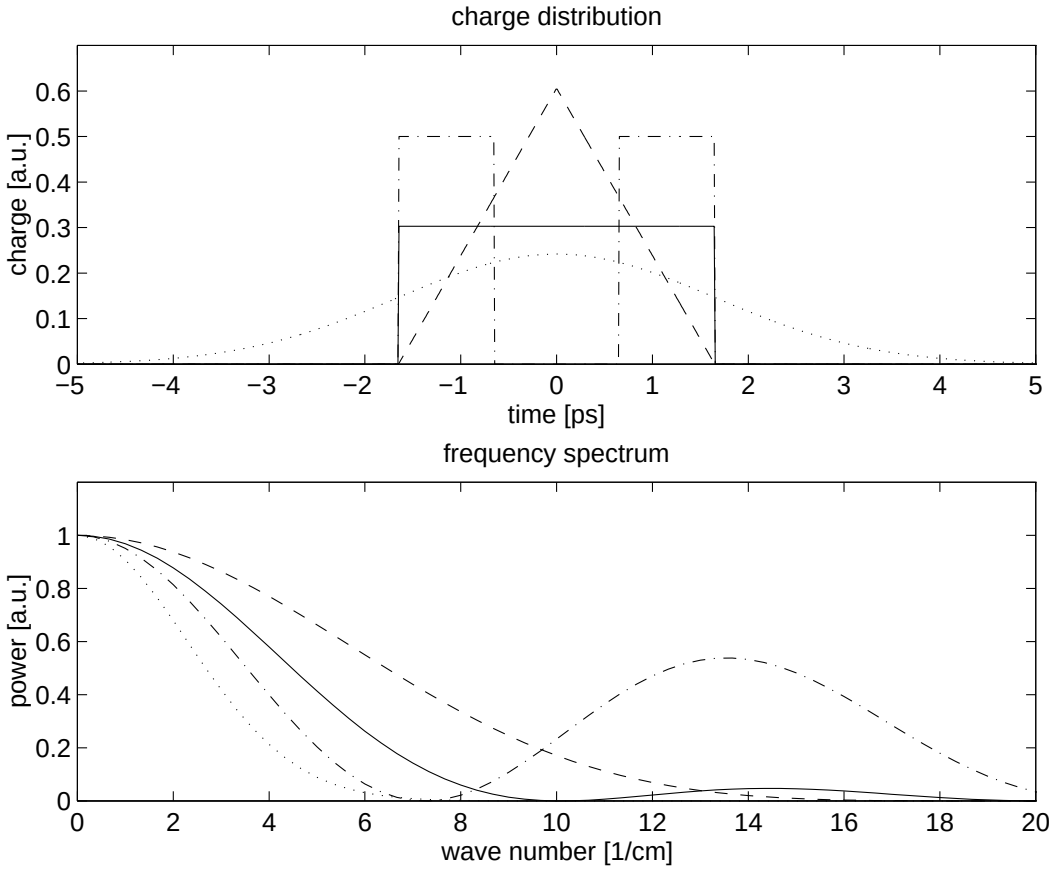

Figure 1.12: Upper plot: flat distribution with 3.3 ps full length (solid line); Gaussian distribution with $\sigma = 1.65$ ps (dotted line); triangular distribution with 3.3 ps full length (dashed line); double-peak with 3.3 ps full length (dashed-dotted line). Lower plot: corresponding spectra.

Given that the secondary maxima in the case of a flat and triangular distribution are smaller than the central maximum and therefore cannot easily be observed, these charge distributions can hardly be distinguished from their spectra. A double-peak distribution shows a drastically different spectrum with pronounced secondary maxima.

Although in principle the bunch shape can be obtained from the shape of the spectra, most charge distributions have a similar slope of the first maximum and can therefore in practice not be distinguished.

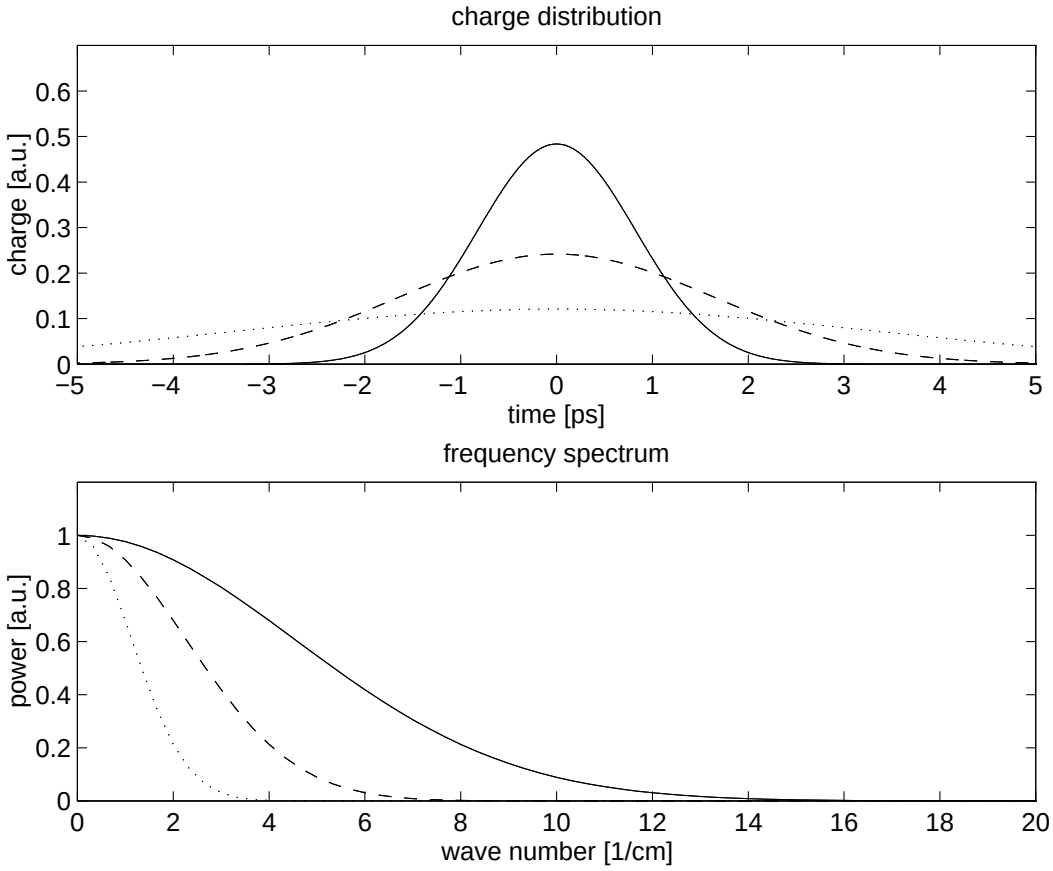

Figure 1.13: Upper plot: Gaussian distributions with $\sigma = 0.825$ ps (solid line), 1.65 ps (dashed line) and 3.3 ps (dotted line). Lower plot: corresponding spectra.

1.5.4 Application to Various Bunch Lengths

While the exact shape of the spectrum gives some information on the bunch shape, the position of the minima permits determination of the bunch length. For a flat distribution, for example, the $sin(x)/x$-shaped spectrum has its minima at wave numbers $\bar{\nu} = n/l$, $n = 1,2,3...$, where l is the full length of the bunch. For a Gaussian distribution, the spectrum is again a Gaussian where $\sigma_t = 1/\sigma_\omega$. Since in practice often only the first maximum can be measured, a Gaussian distribution is a reasonable approximation. In Figure 1.13, Gaussian charge distributions of various length and their normalized spectra are shown. From the width of the Gaussian in the frequency domain, the bunch length can directly be obtained.

Chapter 2

Millimeter-Wave Optics, Devices and Systems

The radiation emitted by a particle bunch is only coherent at wavelengths of the order of the bunch length and longer. Measurements of coherent radiation have been reported in the far-infrared regime ([14],[15],[16] and references therein), but for picosecond bunches the onset of coherence is in the millimeter wavelength range. Applying optical techniques to millimeter-waves is called the quasi-optical approach. Longer wavelengths have to be handled using standard waveguide techniques which means necessarily a limitation in bandwidth. Since bunch length measurements require spectroscopy over a wide wavelength range, the quasi-optical approach was chosen.

In the wavelength range of several millimeters, diffraction is often a limiting factor since the beam diameter is small compared to the wavelength. It therefore acts as a pinhole and the radiation is divergent already after emission.

2.1 Signal Detection

The choice of a detector for coherent transition radiation is essentially determined by the bunch length that is expected. A broadband detector is required which covers as much of the coherent spectrum as possible.

Detectors for far-infrared and millimeter-wave radiation can roughly be classified in mixers (heterodyne detectors) and heat detectors. Heat detectors are mainly used for quasi-optical systems which are required to work over a wide wavelength range. While a variety of detectors are available for the far-infrared, bolometers, pyroelectric detectors and Golay cell detectors are the only detector types that work even at wavelengths of several millimeters.

A bolometer is a resistive element which absorbs radiation. The resistance

changes as a result of the heating. If a bias current is passed through the device, the change of the resistance results in a change in output voltage. Bolometers are commercially available for operation at room temperature and at cryogenic temperatures. While bolometers for infrared radiation can be operated at room temperature, they usually have to be cooled with liquid nitrogen or liquid helium to obtain sufficient signal-to-noise ratio in the millimeter range. Bolometers commonly used in the millimeter wavelength range are for instance made from indium antimonide ($InSb$). They are mounted in a liquid helium cryostat and have a sensitivity range from the far-infrared up to wavelengths of a few millimeters.

Pyroelectric detectors consist of crystals which possess an internal electric dipole moment. Heating of the sample causes a change in the dipole moment and hence a surface charge. If a pair of electrodes is applied to the probe, the radiation can be detected by measuring the charge on the plates. Pyroelectric detectors work in the far-infrared. They are also sensitive to longer wavelengths, but the small diameter of a few millimeters generally determines a cutoff at wavelengths of the order of the aperture.

Golay cells were developed during World War II in order to detect aircrafts by measuring their heat radiation. The development of these detectors came to an end when radar became available [17]. A Golay cell detector consists of a metal foil inside a gas cell. The foil absorbs the incoming radiation, heats up and causes a change in pressure in the gas cell. In the original Golay cell, one side of the gas cell is coated with a reflecting material. The change in volume can then be read out by an optical system, either by deflection of a light beam or by measuring interference fringes.

In photo-acoustic detectors, the pressure change is detected by a microphone which makes the system less sensitive.

For the measurement of picosecond bunches, a pyroelectric detector and a photo-acoustic detector have been used which will now be characterized in detail.

2.1.1 Photo-Acoustic Power Meter

For the detection of millimeter waves, a power meter from Thomas Keating Ltd. was chosen [18]. It has a flat response from 0.1 mm up to 10 mm wavelength (3 THz - 30 GHz). The aperture of the detector is 30 $\times$ 60 mm^2. The power meter is a photo-acoustic detector consisting of a closed gas volume with a metal foil absorber inside. A known fraction (49$\pm$2%) of the radiation directed onto the window is absorbed by the foil, the rest is partly transmitted and partly reflected. A hearing aid microphone powered by a 9 V battery is used to transform the change in pressure into a voltage. An incoming radiation pulse results in a steep increase of the detector output followed by a long decay. While the time constant

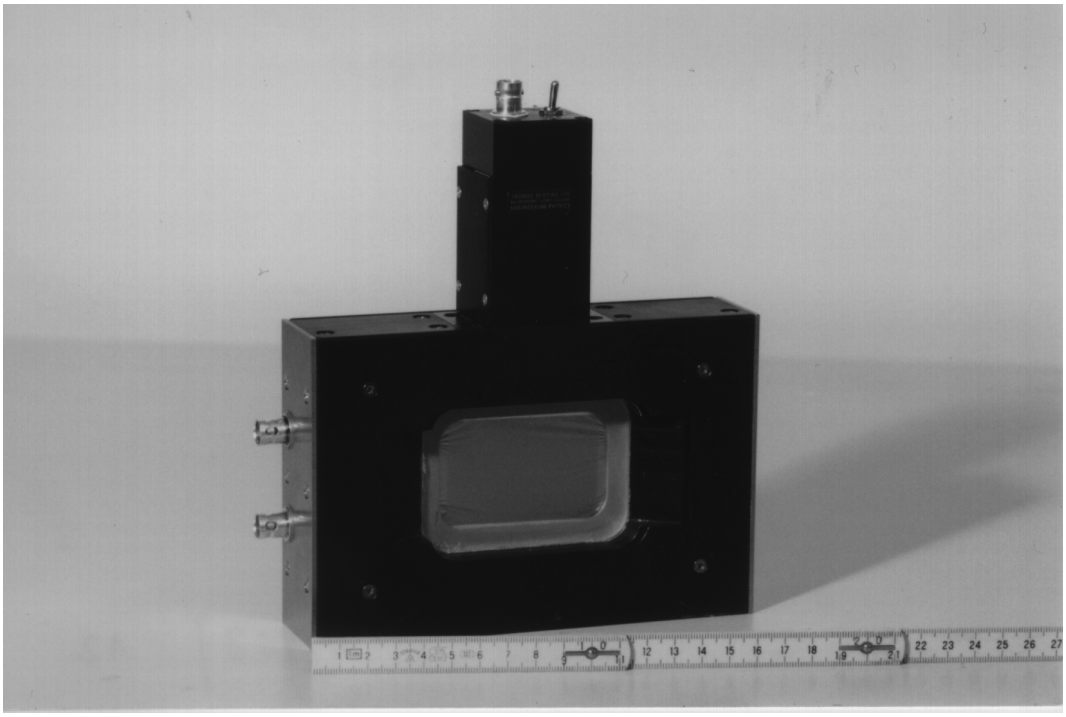

Figure 2.1: Thomas Keating photo-acoustic detector. The radiation is directed on the input window on either side of the device. The output voltage is obtained from the BNC connector on top of the detector head. The two BNC connectors on the left are directly connected to the foil and used for calibration. The microphone is housed in the box on top of the cell.

	nominal	calibrated
aperture [mm]	> 30	
voltage response [VW^{-1}]		0.125
noise equiv. power [$WHz^{-1/2}$]	5×10^{-6}	
output impedance [Ω]	< 2500	
bandwidth [Hz]	< 40	
wavelength range [mm]	0.1 - 10	

Table 2.1: Nominal and calibrated parameters of the Thomas Keating photo-acoustic detector.

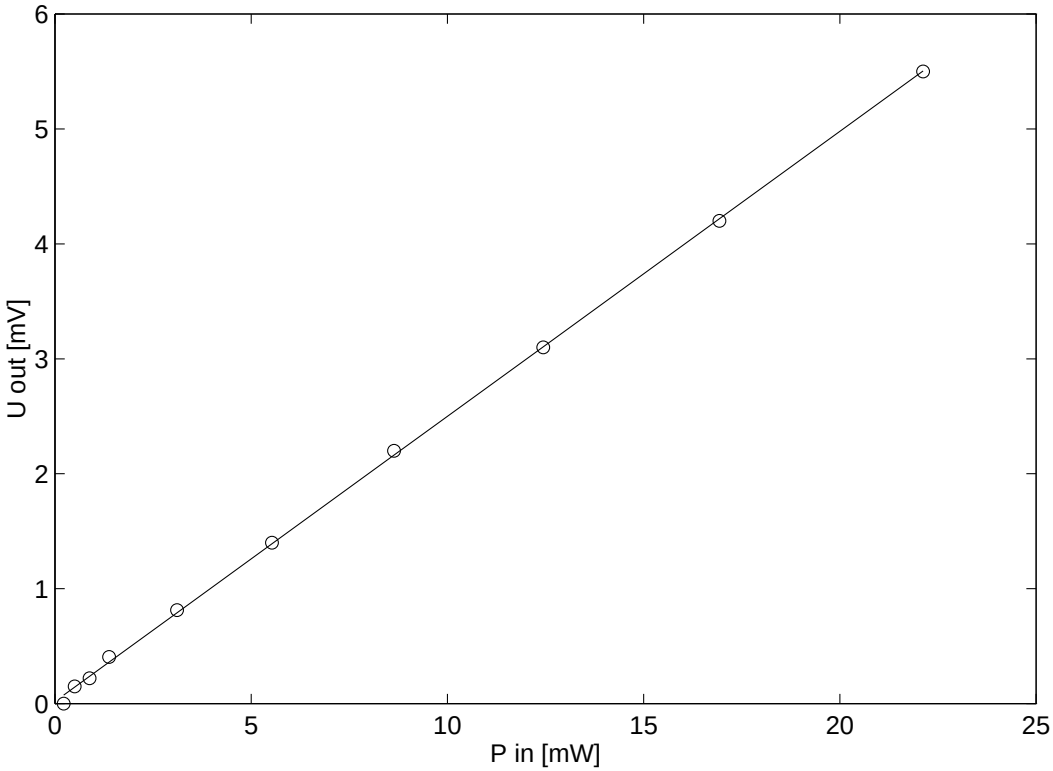

Figure 2.2: Output voltage versus input power for 20 ms long pulses at 7 Hz. The signal is obtained from an oscilloscope without additional amplification.

for the increase of the signal takes about 0.5 ms, the decay time is in the order of 10 - 15 ms.

The Thomas Keating photo-acoustic detector allows absolute measurement of the radiation power since it can easily be calibrated. For this purpose, first the resistance R_f of the foil is measured via the two BNC connectors at the side of the detector head which are directly connected to the foil. Then a square wave current is passed through the foil via one of these connectors producing Ohmic power in the foil:

$$P_{in} = \frac{U_{in}^2}{R_f}. \tag{2.1}$$

The output voltage U_{out} is then measured and the internal response in units of VW^{-1} obtained from

$$r_{i(power)} = \frac{U_{out}}{P_{in}}. \tag{2.2}$$

To obtain the external response r_e, the result must be multiplied by a factor of 0.5 since the foil absorbs only $(49 \pm 2\%)$ of the radiation. If optical components (e.g.

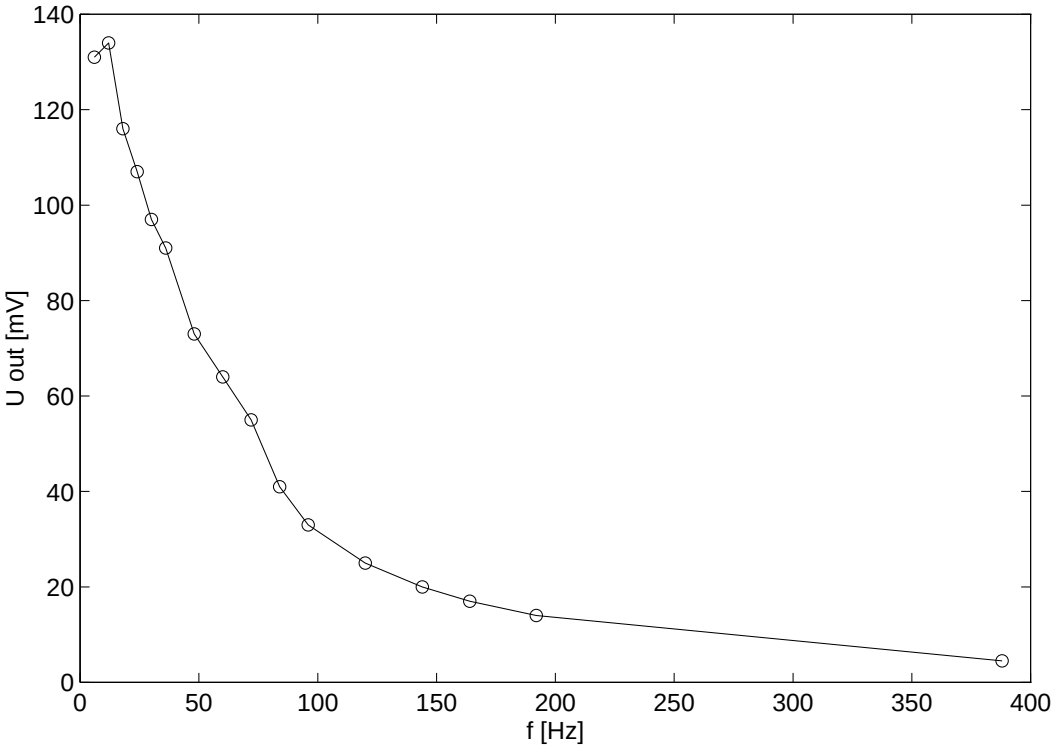

Figure 2.3: Output voltage versus pulse repitition rate for radiation from a carbon filament lamp chopped mechanically at variable frequency. The duration of the light pulses and hence the energy per pulse also changes corresponding to the change in frequency.

windows or filters) are used that cause losses, these also have to be taken into account. The calibration factor and the precision of the measurement depend on the specific setup and the time structure of the radiation. Figure 2.2 shows a typical calibration curve measured using an oscilloscope without additional amplifier. The pulse width for these measurements was 20 ms and the repitition rate 7 Hz. For these parameters, an internal response of 0.248 VW^{-1} was obtained.

The power meter can also do absolute energy measurements for pulsed beams with a pulse width of a millisecond or less and a pulse repitition rate of less than about 40 Hz. The calibration is done in the same way as for power measurement. The energy generated in the foil is given by

$$E_{in} = \frac{U_{in}^2}{R_f} \Delta t, \tag{2.3}$$

where Δt is the length of the pulse. The internal response in units of VJ^{-1} is then given by

$$r_{i(energy)} = \frac{U_{out}}{E_{in}} = \frac{U_{out} R_f}{U_{in}^2 \Delta t}. \tag{2.4}$$

Not only the amplitude and width of an incoming radiation pulse determines the detector output, but also the repitition rate. The power meter requires pulsed radiation. A continuous source must be chopped mechanically. In order to quantify the dependence of the output voltage on repitition rate, radiation from a carbon filament lamp was chopped at variable frequency and directed on the detector head. The output voltage was measured as a function of the chopper frequency. Figure 2.3 shows the resulting calibration curve. The signal level decays significantly with increasing repitition rate. In the case of a continuous source, the detector gives no output at all. Therefore, the calibration of the detector is only valid for a given pulse repitition rate. If the repitition rate is too high, it is necessary to chop the radiation mechanically.

2.1.2 Pyroelectric Detector

In addition to the photo-acoustic detector head, a Molectron P2-49 pyroelectric detector was used. It consists of a $LiTaO_3$ crystal with a pair of electrodes attached to it. Radiation is absorbed by the blackened front electrode and increases the temperature of the crystal. The change in temperature changes the lattice spacing inside the crystal, producing a change in the spontaneous electric polarization. When electrodes are applied normal to the axis of the polarization and are connected through an external circuit, a current is generated to balance the polarization effect. The current produces a voltage across an appropriate load which is read out. The output voltage is proportional to the rate of change in temperature.

	nominal	calibrated
aperture [mm]	9	
voltage response [VW^{-1}]	40000	28300
noise eqiv. power [$WHz^{-1/2}$]	1.33×10^{-8}	1.0×10^{-8}
output impedance [Ω]	100	
bandwidth [Hz]	0.05 - 500	
spectral response [μm]	0.1 -100	

Table 2.2: Nominal and calibrated parameters of the P2-49 pyroelectric detector.

The pyroelectric detector is much more sensitive than the photo-acoustic power

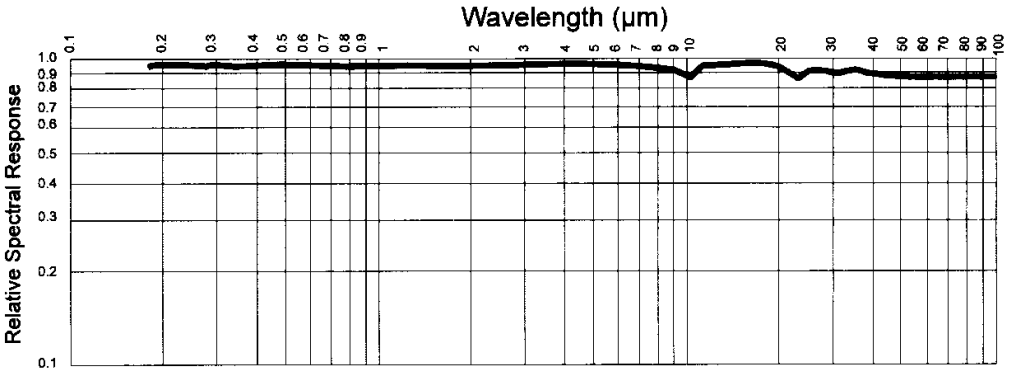

Figure 2.4: Relative spectral response versus wavelength for Molectron P2-49 pyroelectric detector.

meter, but the response has only been calibrated up to $\lambda = 100$ μm. It is flat from 0.2 μm to 100 μm. Figure 2.1.2 shows the relative response versus wavelength as given by the manufacturer [19]. No calibrated data are available for longer wavelengths. The response has been determined with a pulsed laser to 28.3 kVW^{-1} at $\lambda = 632.8$ nm and a repitition rate of 10 Hz [20]. The diameter of the detector is 9 mm. The time constant of the detector for both increase and decay of the output voltage is in the order of a millisecond, that is much faster than the photo-acoustic detector. The nominal value for the upper limit of the repitition rate is at about 500 Hz. Table 2.2 shows some important nominal and calibrated parameters of the detector.

2.2 Signal Amplification

Signal amplification is almost always necessary for measurements with the photo-acoustic detector. Two amplifiers were built for the measurement of coherent transition radiation. One of them contains a MAX263 universal bandpass filter [21] for suppression of high frequency noise. It provides gains of 1, 10 100 and 1000. The circuit diagram is shown in Fig. B.1. In addition, a differential amplifier without filter has been built. It provides gains of 100, 200, 400, 1000 and 6000. The circuit diagram is shown in Fig. B.2.

2.3 Windows

Windows may be required in a quasi-optical setup through which the radiation is passed. In the case of bunch length measurements for example, the radiation is produced inside the vacuum system of the accelerator and is then directed

through a window onto the spectrometer which is placed outside the vacuum. Other tasks of windows may be to separate the setup from the outer atmosphere, for instance if measurements are made under a nitrogen atmosphere in order to avoid water absorption effects. It may also be necessary to protect the setup from visible light or other distortions.

Common window materials for visible light such as quartz and glass are non-transparent in the infrared but become transparent again for millimeter waves and have then a flat transmission of about 60%. High-density polyethylene (HDPE) or polytetramethylpentane-1 (TPX) are also good window materials for infrared and millimeter waves. The transmission curves for some commonly used millimeter-wave materials are given in Appendix A.

2.4 Flat Mirrors

Reflectors for millimeter waves have the same characteristics as for visible light. The flatness of the reflecting surface should be 1/10 λ which is in the order of 0.1 mm and therefore less critical than for optical wavelengths. It is important that first surface mirrors are used. Here, the reflecting substrate forms the surface of the mirror and is not coated with a protecting layer which might have an effect on the radiation.

Reflectors have been made by coating commercially available optical mirrors or plates with a thin layer of gold, which has a very good reflectivity in the infrared. In order to achieve a good adhesion of the gold on the support material, the surface is first coated with a layer of copper and then with a layer of gold by vapor-deposition.

In most cases, polished brass or aluminum provide sufficient surface quality. Such reflectors are rugged and easy to mount. Since in many cases quasi-optical systems cannot be aligned with a laser, the components must be manufactured and mounted precisely.

2.5 Roof Mirror Reflectors

A roof mirror is a pair of flat mirrors arranged at an angle of 90^o. The junction of the two reflecting plates is referred to as the roof line. The roof mirror makes two reflections and turns the polarization vector of the radiation. Roof mirrors are frequently used in polarizing instruments. Figure 2.5 illustrates the process of altering the polarization state of an incident field. Here a polarized beam is incident upon the roof mirror with its electric vector orientated at an angle θ with respect to the roof line. The input and output direction is normal to the

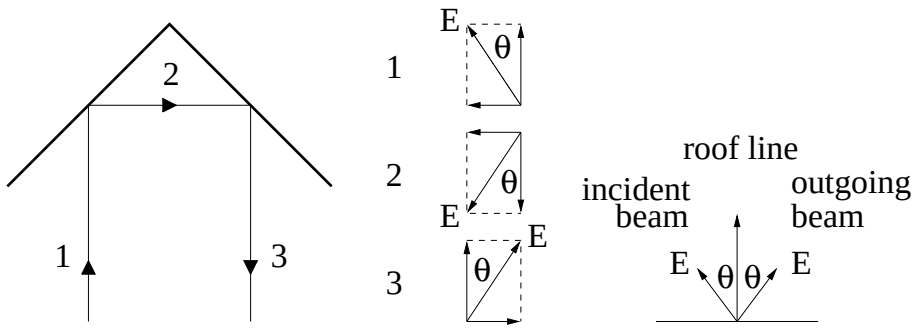

Figure 2.5: Roof mirror arrangement to rotate the polarization of an incoming beam upon reflection.

roof line. The electric vector of the outgoing beam will then be at an angle of -θ with respect to the roof line.

Roof mirrors have been made from pairs of polished brass plates which are screwed together at 90^o and mounted on a fixed support.

2.6 Focusing Elements

Focusing elements are essential for instance to produce a parallel beam which is to be directed through an optical setup or to focus radiation on a detector of small aperture. It can be achieved either by quasi-optical lenses or by spherical, parabolical or ellipsoidal mirrors.

Quasi-optical lenses can be made from polyethylene or teflon. Their parameters can be calculated as for an optical lens. The refractive indices of these frequently used lens materials are given in Appendix A. Quasi-optical lenses cause significant losses in the radiation power. Another problem for their application at particle accelerators is that they are not radiation resistant.

Spherical mirrors can be made by coating convex lenses with a reflecting metal layer as in the case of flat mirrors. Spherical mirrors provide good focusing only if the incident and reflected beams are close to the axis. If this is not the case, a spherical mirror will cause aberration.

Parabolic or ellipsoidal mirrors cause no losses and aberrations. They are therefore mainly used in quasi-optical systems. Off-axis paraboloids do not only focus the incident radiation but also make a deflection such that incoming and outgoing beam are not on axis. Such mirrors can be machined from brass or aluminum. The surface is then polished by hand. Figure 2.6 illustrates the principle of a spherical mirror and an off-axis paraboloid.

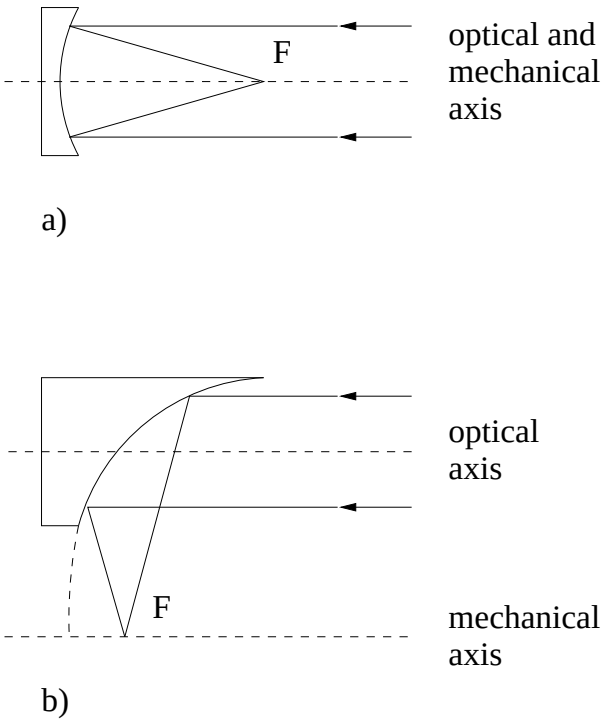

Figure 2.6: (a) Spherical mirror and (b) off-axis paraboloid for focusing of millimeter waves.

2.7 Filters

Filters are used to select certain frequencies out of a broadband source. High-pass, band-pass and low-pass filters for millimeter waves can be realized.

High-pass filters are generally made of waveguides, making use of the fact that a waveguide has a low-frequency cutoff which depends on its diameter. One can either use a single waveguide or an array of waveguides. A set of high-pass filters for millimeter waves was manufactured by drilling holes into brass plates. This is described in detail in Chapter 3.

Low-pass filters are for instance wire grids. As described below, a grid acts as a reflector for an electric field polarized parallel to the wires. The performance of a grid decreases with increasing frequency, that means a grid becomes transparent for sufficiently high frequencies. The transition is, however, not sharp but smooth as can be seen from Fig. 2.9.

Band-pass filters are more complicated to manufacture. Metallic meshes can be used for this purpose. They can be made from dielectric substrates coated with a metallic pattern. Figure 2.7 shows some frequently used mesh patterns. The

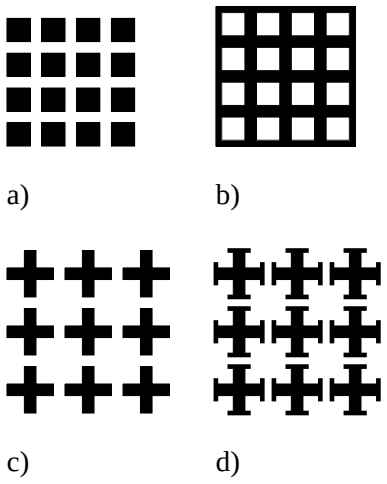

Figure 2.7: Metallic mesh patterns: (a) capacitive mesh; (b) inductive mesh; (c) resonant crosses; (d) Jerusalem crosses.

analysis of their spectral behaviour is complicated and subject of a large amount of literature, e.g. [22], [23], [24], [25].

The capacitive mesh filter acts as a mirror at wavelengths smaller than the square size. These wavelengths set up an oscillatory current in the metal which can locally be considered uniform. This uniform current produces a reflected wave as in the case of an ordinary flat mirror. A capacitive mesh is, on the other hand, transparent for wavelengths much larger than the size of the metal squares. Such long wavelength radiation is unable to induce an oscillatory current in the metallic regions and the mesh appears essentially transparent to it.

The inductive mesh is just the inverse of the capacitive mesh, and so are its properties just the inverse of those of a capacitive mesh. It can be considered as an arrangement of two perpendicular arrays of parallel wires. For wavelengths larger than the uncoated regions, the incident radiation sets up currents along the wires which produce a reflected wave. The mesh behaves in this case like an intransparent metal sheet. For wavelengths much smaller than the gaps, radiation can only induce a significant current in the wires if it passes very close to them. Radiation at these wavelengths passes the filter almost undisturbed.

Resonant-cross and Jerusalem-cross filters provide a sharp reflection maximum centered at a given frequency and can therefore be used as bandpass filters. The crosses behave as pairs of crossed dipoles. An incident wave induces an oscillatory current along the dipoles with a resonant maximum at wavelegth $\lambda = 2l$, where l is the length of the dipole arms. The resulting reflectivity of such a pattern is low in general, with a sharp peak at a the resonance frequency.

The Jerusalem-cross pattern is a modification of the resonant-cross pattern having a narrower reflection band and a higher peak reflectivity.

Metallic mesh filters can be made either by coating a dielectric substrate with a metallic pattern or by cutting or etching a pattern into a thin metallic foil. Patterns without a supporting dielectric are called free-standing meshes. In general, all these systems work better in the far-infrared rather than in the millimeter wavelength range.

2.8 Beamsplitters

A semi-reflecting sheet can be used as an amplitude beamsplitter. In quasi-optical systems, Mylar[1] or Hostaphan[2] (polyethylene terephthlate, $C_5H_4O_2$) are frequently used for this purpose. The efficiency, defined as the modulus squared of the reflectivity times the transmittivity $|RT|^2$, is not constant but a function of wave number and thickness of the foil. For a Mylar foil of thickness t and refractive index $n = 1.85$, arranged at an angle of 45^o with respect to the incoming radiation, the total amplitude reflection and transmission coefficients R and T are given by

$$R = -r\frac{1-\exp(i\phi)}{1-r^2\exp(i\phi)} \tag{2.5}$$

$$T = (1-r^2)\frac{\exp(i\phi/2)}{1-r^2\exp(i\phi)}, \tag{2.6}$$

where r is the amplitude reflection coefficient of the air/Mylar interface at 45^o and

$$\phi = 4\pi t\bar{\nu}\sqrt{(n^2-1)/2}. \tag{2.7}$$

In fact, the efficiency must be calculated for the parallel and perpendicular polarization component using $r_\perp$ and $r_\parallel$. In the case of unpolarized radiation, the efficiency is given by

$$|RT|^2 = \frac{|R_\perp T_\perp|^2 + \left|R_\parallel T_\parallel\right|^2}{2}. \tag{2.8}$$

Here, the absorption in the Mylar foil is not taken into account. The effect of absorption is found in [26] and shown to be small within the first lobe of the interference pattern. Figure 2.8 shows the calculated efficiency versus wavenumber of mylar foil beamsplitters according to (2.8) for different thicknesses. The radiation is assumed to be unpolarized. The strong variations are due to the fact, that reflections both from the first and the second surface give rise to interference.

[1]Trademark, DuPont S.A.
[2]Trademark, Hoechst GmbH.

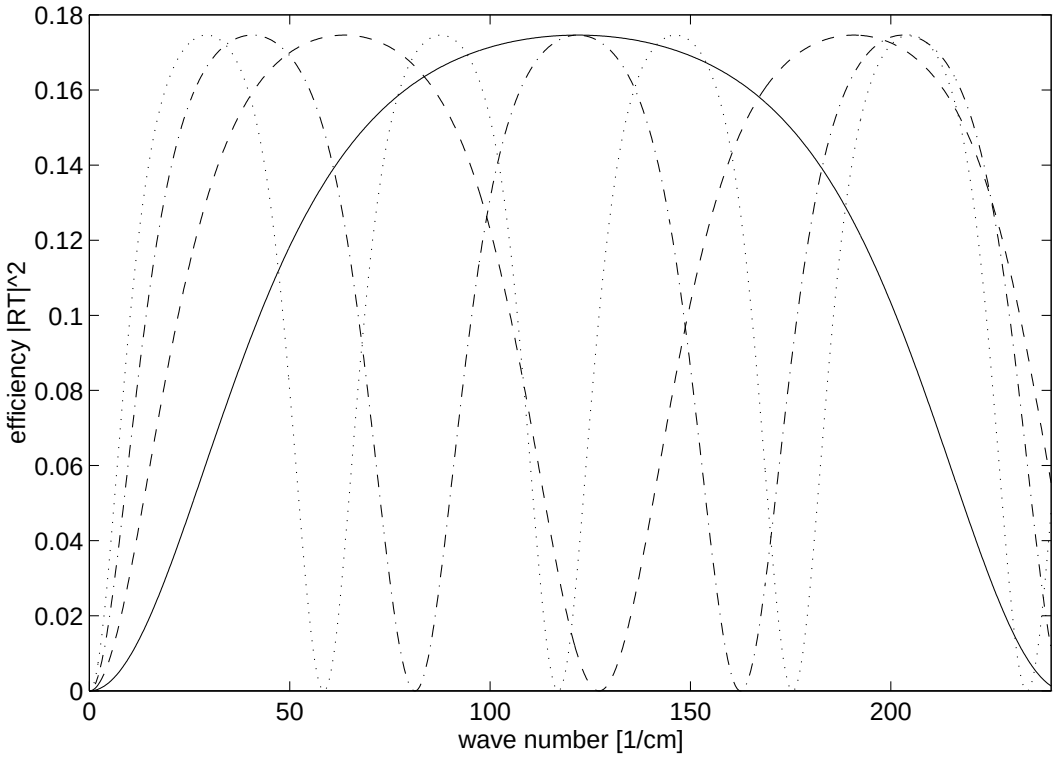

Figure 2.8: Calculated efficiency versus wave number for Mylar/Hostaphan beamsplitters of various thickness at 45^o: t = 12 μm (solid line); t = 23 μm (dashed line); t = 36 μm (dashed-dotted line); t = 50 μm (dotted line). The radiation is assumed to be unpolarized. Absorption in the Mylar is not included.

Measurements using an uncoated Mylar foil beamsplitter have to be corrected for this effect [14]. It becomes clear from Fig. 2.8 that for the low wavenumbers of interest here, Mylar is not an appropriate beamsplitter material.

For many applications, beamsplitters are required that have a constant efficiency over a wide frequency range. A possible choice is a capacitive mesh made from Mylar foil with a pattern of copper dots [27]. Such an arrangement of opaque and transparent regions acts as a wavefront beamsplitter. It avoids the interference effects of a pure Mylar amplitude beamsplitter and can therefore be used in a wider frequency range. However, a beam passing such a beamsplitter undergoes diffraction and is then less collimated and directed.

Wave front beamsplitters can be made by coating Mylar foil with photo lacquer and exposing them using a mask. After this, the non-exposed coating is removed chemically. The foil is coated with copper and the photo structure removed using acetone. The remaining structure is a pattern of copper dots with sharp edges.

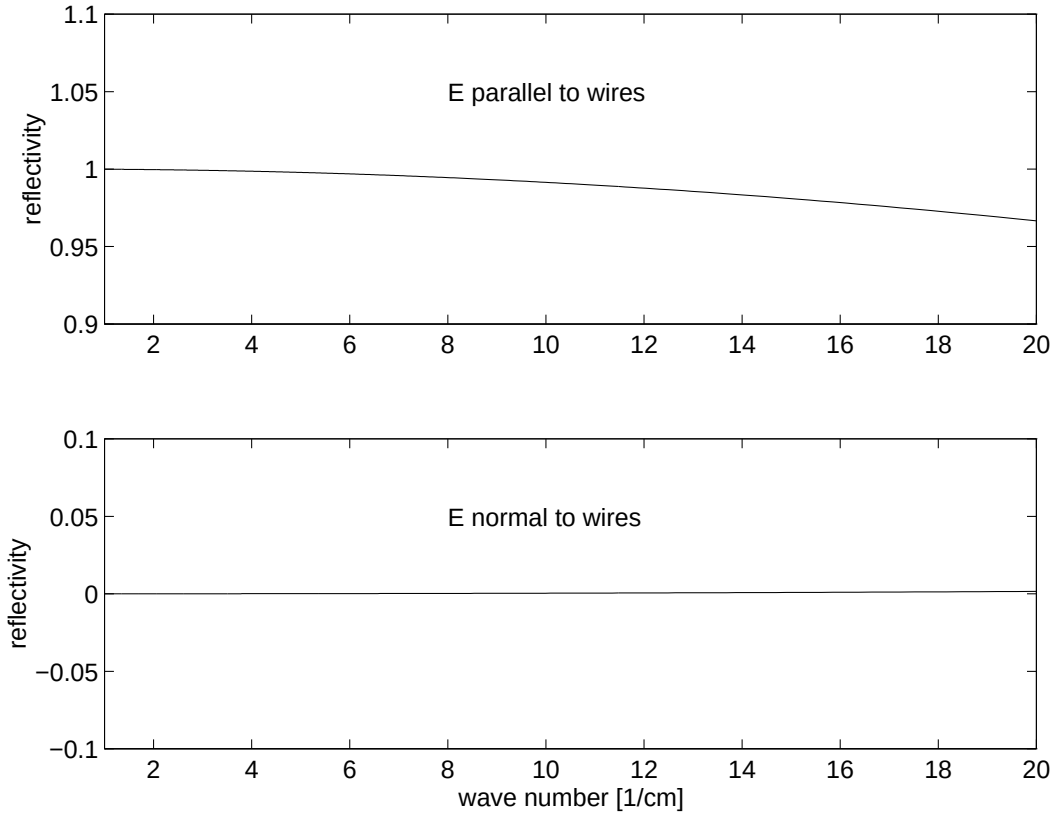

Figure 2.9: Computed power reflectivity for the components of the electric field parallel and normal to the wires of a grid. The diameter of the wires is 20 μm and the spacing is 100 μm. The grid acts as an ideal polarizer up to a wave number of about 20 cm^{-1}.

The sharp edges are required for proper operation of the beamsplitter [28].

2.9 Wire Grids

A wire grid acts as a polarizer since the component of the electric field parallel to the wires is reflected and the component of the electric field perpendicular to the wires is transmitted. The reflection coefficients for the component parallel to the wires, $r_\parallel$, and for the component normal to the wires, $r_\perp$, are given by [29]

$$r_\parallel = \left[1 + \left(\frac{2s}{\lambda}\right)^2 \ln\left(\frac{s}{\pi d}\right)^2\right]^{-1/2}, \tag{2.9}$$

$$r_\perp = \left[\frac{\pi^4 d^4}{(2\lambda s)^2[1 + \pi^4 d^4/(2\lambda s)^2]}\right]^{1/2}. \tag{2.10}$$

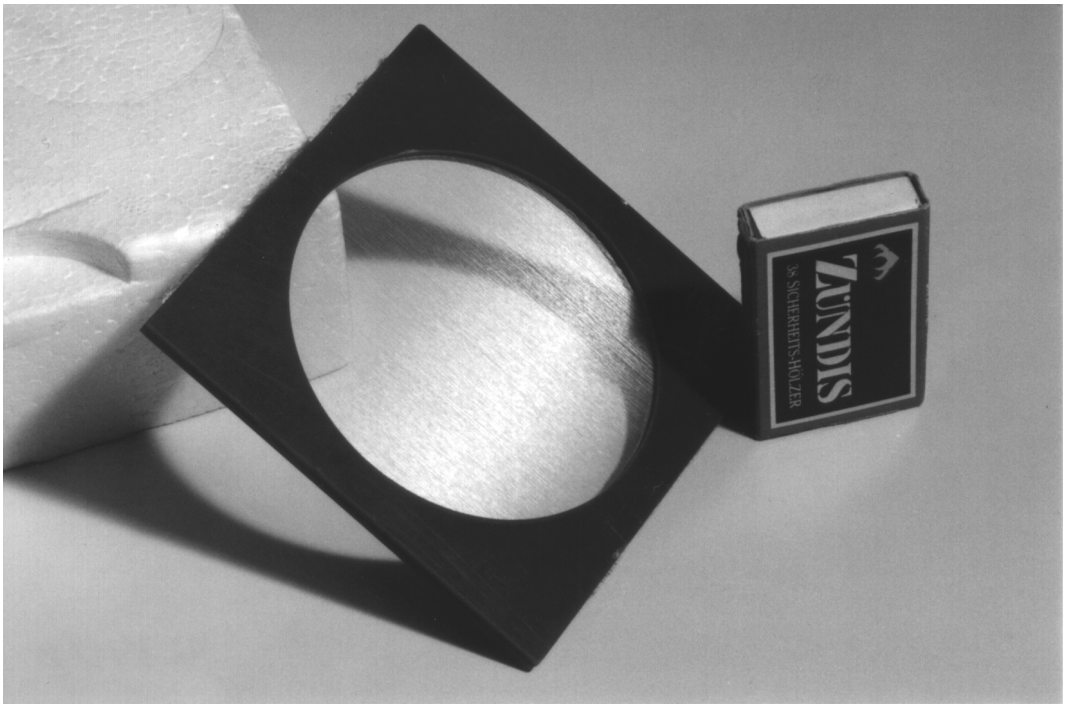

Figure 2.10: Wire grid from 20 μm tungsten wire at a spacing of 100 μm wound on a hard paper frame.

The reflection coefficients are plotted in Fig. 2.9 as a function of the wave number for a grid made from 20 μm tungsten wire at a spacing of 100 μm. A wire grid can be considered as an ideal polarizer through the whole millimeter-wavelength range. At larger wave numbers, the performance of a grid gently decreases.

A wire grid can be used as a beamsplitter. If the electric vector of an incident field with amplitude A is at an angle θ with respect to the wires, then the transmitted field will have an amplitude $A\sin\theta$ and the reflected field $A\cos\theta$. For $\theta = 45^o$, the grid therefore acts as a 50:50 beamsplitter where both the reflected and transmitted component have a magnitude of $A/\sqrt{2}$. The field component perpendicular to the wires is simply transmitted. The field component parallel to the wires is reflected and undergoes a phase change of 180^o.

The wire grids used here have been manufactured from gold-plated tungsten wire. The diameter of the wire is typically 20 μm and the spacing 100 μm. The grids are made by winding the wire on a hard paper frame using a coilwinder. Another frame is then glued on top of the windings and the outer layer of wires cut off, such that only one layer of wires remains inside the frames. The aperture of the grids is 80 mm. Figure 2.10 shows a wire grid polarizer for millimeter waves.

2.10 The Design of Quasi-Optical Circuits

For the design of quasi-optical systems it is convenient to make use of a notation by analogy to the design of electrical circuits. Subsystems can then be designed and used as components of large quasi-optical setups. Only a few types of components are needed. Figure 2.11 shows circuit symbols of some frequently used quasi-optical components [29]. As an example for the use of this notation, the design of a Martin-Puplett interferometer will be discussed in detail in Chapter 8.

While such a diagram is only a schematic design, some practical aspects must be taken into account when assembling a quasi-optical setup. Diffraction becomes important when the aperture of optical components is in the same order of magnitude as the wavelength. For millimeter waves, therefore the aperture of a system must be several centimeters in order to avoid losses due to diffraction. Since beams can never be focused below a waist of the order of the wavelength, there is often a low frequency limit for small aperture components and detectors. Since quasi-optical components often cannot be aligned with a laser, high precision manufacturing and mounting is essential. The components are then mounted in fixed positions on an optical bench.

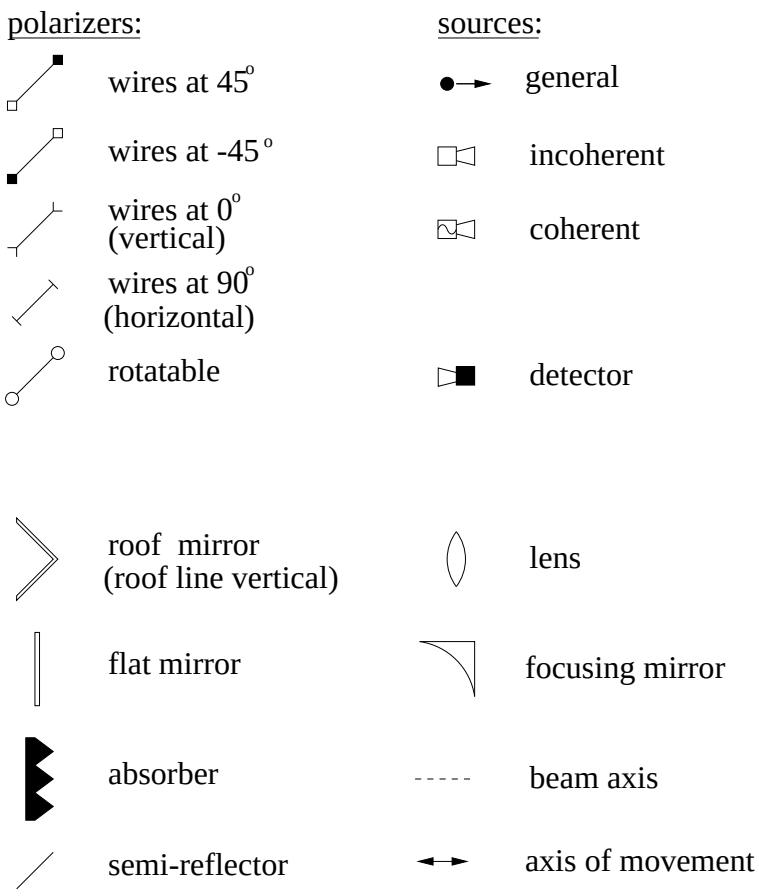

Figure 2.11: Elements for the design of quasi-optical systems.

Chapter 3

Spectrometers for Millimeter Waves

3.1 Filter Spectrometer

A set of filters can serve, together with a broadband detector, as a spectrometer. The advantage of such a system is its simplicity. Since no quasi-optical setup is required, the spectrometer can be used at a low electron beam energy where the opening angle of the radiation is large. The filter spectrometer allows a direct measurement of the spectrum. Its resolution is of course limited by the number of filters available. One can use either high-pass, low-pass or band-pass filters. For the wavelength range of several millimeters, highpass filters can be manufactured mechanically.

3.1.1 High-Pass Filters for Millimeter Waves

A periodic pattern of holes drilled into a brass plate of a given thickness acts as a high-pass filter for millimeter waves [30], [31]. The holes behave like circular waveguides with a given cutoff wave number $\bar{\nu}_c$. The advantage of using an array of waveguides is that the radiation needs not to be directed through a single,

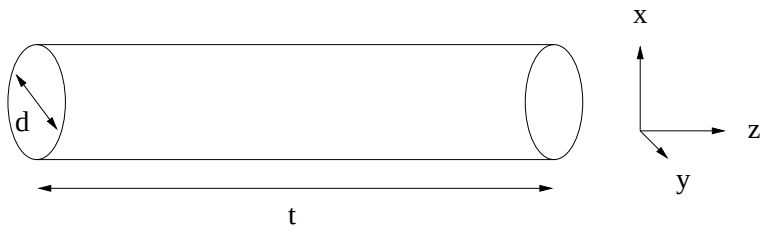

Figure 3.1: Circular cutoff waveguide with diameter d. The length is given by the thickness t of the plate and chosen at twice the diameter of the holes.

small structure and therefore the transmission is larger.

In a hollow cylindrical structure with conducting walls as sketched in Fig 3.1, only TM and TE modes, characterized by $\mathbf{B}_z = 0$ and $\mathbf{E}_z = 0$, can exist. Each of the various modes has its specific cutoff wave number $\bar{\nu}_c$. Assuming infinitely high wall conductivity, each component of a given mode decays along z as $\exp\{i(2\pi c\bar{\nu}\tau) - \beta z)$, where τ is the time and

$$\begin{aligned} \gamma = 0,\ \beta = 2\pi\sqrt{\bar{\nu}^2 - \bar{\nu}_c^2} \quad &\text{for} \quad \bar{\nu} > \bar{\nu}_c \\ \beta = 0,\ \gamma = 2\pi\sqrt{\bar{\nu}_c^2 - \bar{\nu}^2} \quad &\text{for} \quad \bar{\nu} < \bar{\nu}_c. \end{aligned} \tag{3.1}$$

For frequencies far below cutoff, the decay constant is independent of frequency, whereas for frequencies just below cutoff it varies drastically with frequency. This provides a filter function with a very steep slope. Neglecting reflections at both ends of the waveguide, the transmission T is given by

$$T = \exp\{-2\gamma t\} \tag{3.2}$$

where t is the thickness of the plate. The power loss is due to reflections along the length of the waveguide. The value of $\bar{\nu}_c$ varies for different modes. For the transverse magnetic modes, it can be expressed by

$$\bar{\nu}_c = \frac{1}{2\pi\sqrt{\mu_o\varepsilon_0}}\left(\frac{P_{nl}}{d}\right) \tag{3.3}$$

and for the transverse electric modes by

$$\bar{\nu}_c = \frac{1}{2\pi\sqrt{\mu_o\varepsilon_0}}\left(\frac{Q_{nl}}{d}\right), \tag{3.4}$$

where P_{nl} is the l^{th} root of the Bessel function $J_n(x)$ and Q_{nl} is the l^{th} roots of the Bessel function $J_n'(x)$ [32]. For the first few modes, their values are given by

mode	P_{nl}
TM_{01}	2.405
TM_{11}	3.832
TM_{21}	5.136
TM_{02}	5.520

and

mode	Q_{nl}
TE_{01}	3.832
TE_{11}	1.841
TE_{21}	3.054
TE_{12}	5.331.

A waveguide with a given diameter d therefore has a cutoff spectrum, where the lowest cutoff is found for the TE_{11} mode. Its cutoff wave number is given by

$$\bar{\nu}_c = \frac{0.586}{d}. \tag{3.5}$$

Higher order modes have their cutoff at higher wave numbers than the fundamental mode. Figure 3.2 shows the cutoff frequency spectrum for a 1 mm diameter waveguide.

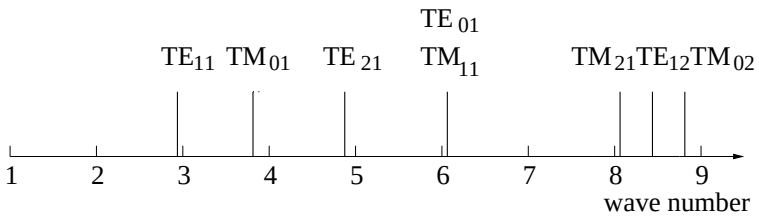

Figure 3.2: Cutoff wave number spectrum for a 1 mm diameter circular waveguide.

The in- and outgoing fields couple to the array of waveguides. By a plane wave incident on the filter, TE and TM modes in the waveguide are excited. They can be expressed as sums over circular waveguide modes. The amplitudes of the plane wave expansions of the incident and transmitted fields have then to be matched to those of the waveguide expansion using the continuity conditions at both surfaces of the filter.

The dominating mode in the waveguide is the TE_{11}, which has also the lowest cutoff frequency. The transmission approaches (3.2) the better the beams couple to the TE_{11} mode inside the waveguide. Unlike in the case of a single waveguide, where the outgoing radiation forms a very broad lobe, interference effects of an array of waveguides provide that the outgoing radiation is well collimated.

Figure 3.3 shows the geometry of a filter and Tab. 3.1 gives the dimensions for a set of filters with various cutoff wave numbers. The thickness of the brass plates is chosen at twice the diameter of the holes in oder to suppress long wavelengths sufficiently. The spacing of the holes provides closest possible packing of the waveguides. The transmission was specified to 85% for the cutoff wave number.

Ten filters were manufactured according to Tab. 3.1 by drilling patterns of holes into brass plates. The array of holes covers 50 mm $\times$ 50 mm, the total size of the filters is 60 mm $\times$ 60 mm. Figure 3.4 shows a filter with nominal cutoff wave number $\bar{\nu}_c = 5.86$ cm^{-1}.

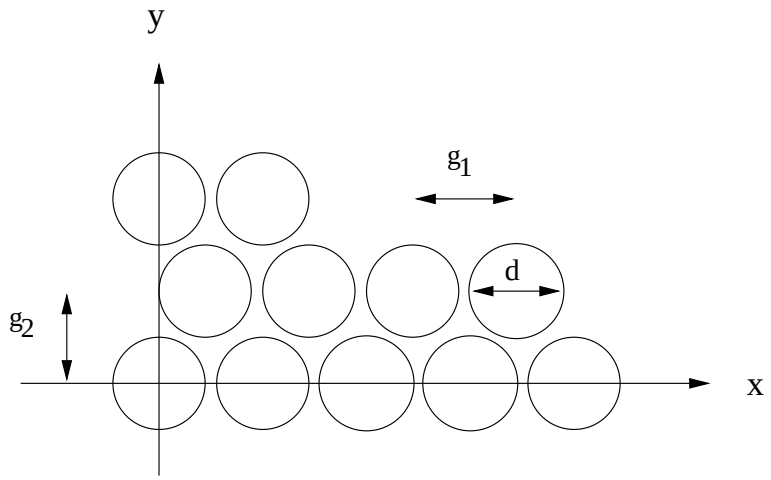

Figure 3.3: Geometry of a high-pass filter for millimeter waves.

filter	d[mm]	$\bar{\nu}_c$ [cm$^-$1]	g_1[mm]	g_2[mm]	t [mm]
1	5.85	1.00	6.882	5.960	11.70
2	3.90	1.50	4.588	3.973	7.80
3	2.90	2.02	3.412	2.955	5.80
4	2.35	2.49	2.765	2.395	4.70
5	2.00	2.93	2.353	2.038	4.00
6	1.70	3.45	2.000	1.732	3.40
7	1.50	3.91	1.765	1.529	3.00
8	1.30	4.51	1.523	1.319	2.60
9	1.15	5.10	1.353	1.172	2.30
10	1.00	5.86	1.176	1.018	2.00
11	0.90	6.51	1.059	0.917	1.80
12	0.80	7.32	0.941	0.815	1.60
13	0.75	7.81	0.882	0.764	1.50
14	0.70	8.37	0.823	0.713	1.40
15	0.65	9.01	0.765	0.662	1.30
16	0.60	9.67	0.706	0.611	1.20
17	0.55	10.65	0.647	0.560	1.10
18	0.50	11.72	0.588	0.510	1.00
19	0.45	13.02	0.530	0.459	0.90
20	0.40	14.65	0.470	0.407	0.80
21	0.35	16.75	0.411	0.356	0.70
22	0.30	19.50	0.353	0.306	0.60

Table 3.1: Nominal parameters for a set of high-pass filters.

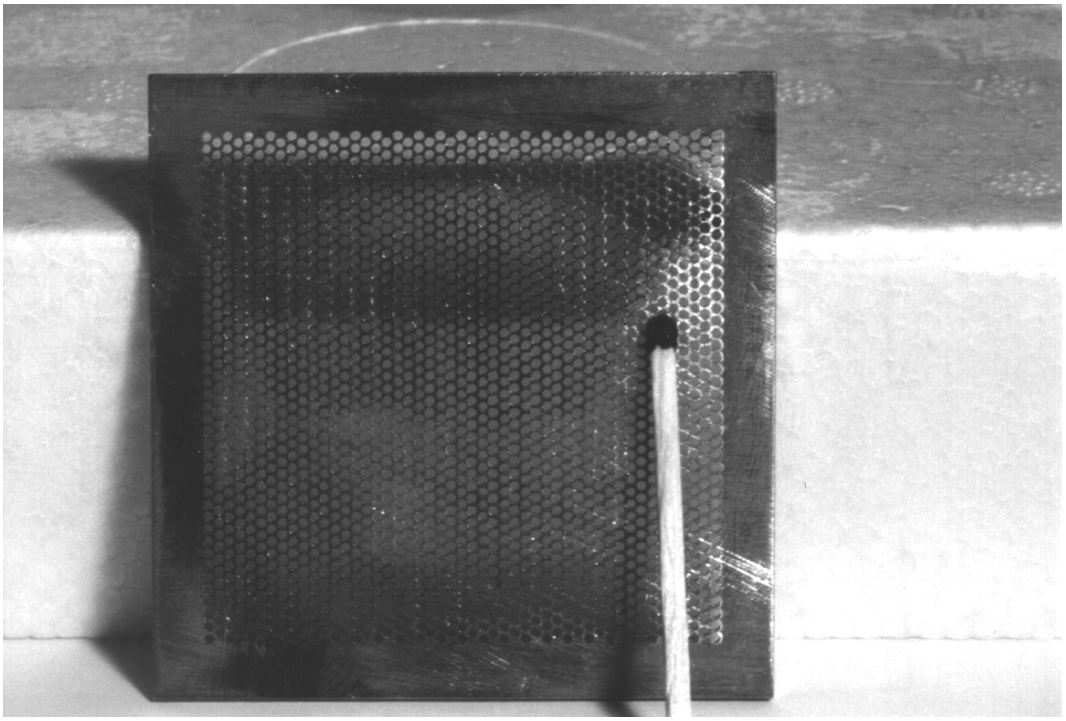

Figure 3.4: High-pass filter with cutoff wave number $\bar{\nu}_c = 5.86$ cm^{-1}.

3.1.2 Characterization of Filters

Due to the manufacturing process, the dimensions of the holes are not exactly as specified. The hole diameters were measured for a number of holes on both sides of each filter with a microscope. They deviate slightly from those specified in Tab. 3.1 and are not exactly equal on both sides of the filters. The actual dimensions are given in Tab. 3.2. The diameters of the holes on either side of a filter are referenced to as d_a and d_b, while d_m is the mean value. The cutoff wave number is then obtained from (3.5).

For some of the filters, the cutoff wave number has been measured using radiation from backward wave oscillators and synthesizers [33]. The transmitted power was measured as a function of the source frequency. Figure 3.5 shows the measurement of the cutoff for the filter with nominal cutoff wave number $\bar{\nu}_c = 1$ cm^{-1}. The slope of the transmission curves at cutoff turned out to be less steep than one would expect from (3.2). In reality, it has a width of several GHz. Therefore, the cutoff wave number was calculated as the mean value of the two wave numbers where the transmission is 10% and 90% of the first maximum. The measured cutoff wave numbers are given in Tab. 3.2. They do not exactly correspond to the nominal values from Tab. 3.1, because the hole diameters are not exactly as specified.

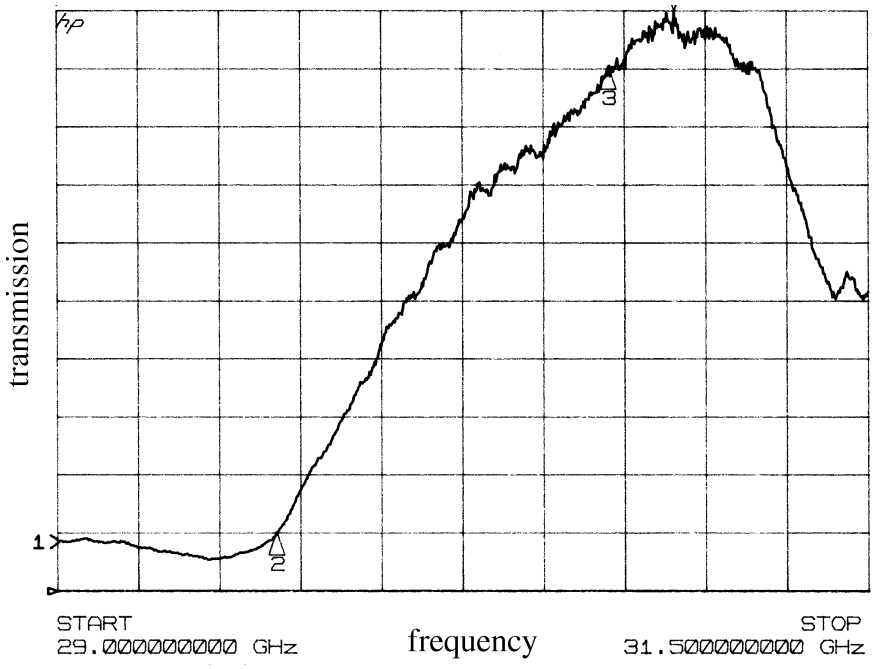

Figure 3.5: Measured transmission (arbitrary units) versus frequency in the cutoff region for a filter with nominal cutoff wave number $\bar{\nu}_c = 1$ cm^{-1} (30 GHz).

filter	d_a [mm]	d_b [mm]	d_m [mm]	$\bar{\nu}_c$ [cm^{-1}] (from d_m)	$\bar{\nu}_c$ [cm^{-1}] (measured)
1	5.85	5.95	5.90	0.99	1.01
2	3.89	3.91	3.90	1.50	-
3	2.90	2.80	2.85	2.06	-
4	2.17	2.22	2.20	2.66	2.43
5	1.94	2.03	1.99	2.94	2.95
6	1.72	1.96	1.84	3.18	3.51
7	1.48	1.51	1.50	3.91	-
8	1.28	1.35	1.32	4.44	-
9	1.08	1.05	1.07	5.48	-
10_a	1.03	1.07	1.05	5.58	-
10_b	0.93	1.01	0.97	6.04	-

Table 3.2: Measured parameters of a set of filters. The diameter of the holes on either side of the filter is d_a and d_b, the average diameter is d_m.

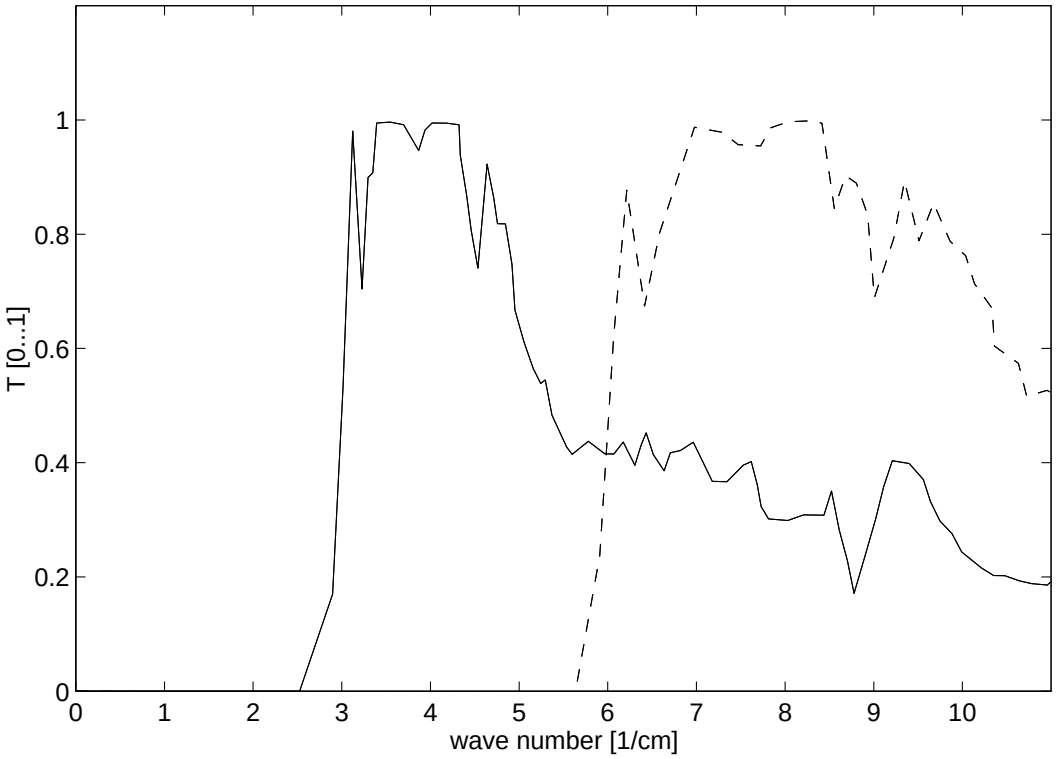

Figure 3.6: Measured transmission versus wave number for filters with nominal cutoff frequencies $\bar{\nu}_c = 2.93$ cm^{-1} and $\bar{\nu}_c = 5.86$ cm^{-1}.

For filters 4 and 6, the measured cutoff wave numbers do not agree with those obtained from the diameters d. This is due to imperfections of the holes. Measurements with a microscope showed that they are not always circular so that the radius is attached with some error. For filters where the cutoff wavenumber could be directly measured, the measured value is the one whereas for the other filters the cutoff wave number must be obtained from the average hole diameter d_m.

Not only the cutoff wave numbers but also the complete transmission curves above cutoff must be known for every filter. The transmission curves of a series of filters were measured over a whole frequency range with a Fourier spectrometer [28]. Fig. 3.6 shows the measured curves for filters with nominal cutoff wave numbers $\bar{\nu}_c = 2.49$ cm^{-1} and $\bar{\nu}_c = 5.86$ cm^{-1}.

As expected, the filters are non-transparent below cutoff. The transmission above cutoff is not constant but decays with increasing wave number. This decay is due to the transition from waveguide propagation to optical propagation: for pure

waveguide propagation one would expect a step function with zero transmission below cutoff and full transmission above cutoff. For optical propagation one expects a constant transmission which is determined by the ratio of open and covered area. The transition between these two propagation mechanisms results in a decay of the transmission curve which becomes constant at high wave numbers. The measured transmission curves have, beside the general decay, several sharp minima. This is due to Fabry-Perot resonances in the waveguide as well as interference effects due to reflected fields from both ends of the waveguides. This effect, already existing for a single waveguide, becomes even more complex for an array of waveguides as discussed here. It has been theoretically and experimentally examined by [31].

An important result of this measurement is that the shape of the curves is equal for all filters and simply scales with $\bar{\nu}_c$. This allows to normalize the transmission curves with respect to the wavenumber. Any given filter can then be characterized simply by scaling this normalized curve to its specific cutoff wave number.

3.1.3 Experimental Setup

The highpass filters are mounted on a rotatable wheel. In addition to the 10 filters, there are an open window without filter and a completely closed section. The wheel is driven by a stepper motor such that the filters can be placed successively in front of the photo-acoustic detector which is mounted as close as possible to the filters. Figure 3.7 shows the experimental setup. The filter spectrometer is placed directly at a transition radiation target such that the distance between the radiatior and the detector is as small as possible.

3.1.4 Analysis Algorithm

In order to measure spectra, the filters are successively moved in front of the broadband photo-acoustic detector. The result of such a measurement is a number of measured values corresponding to the number of filters used. An algorithm was developed to reconstruct the original spectrum from these data.

Without filter, the detector integrates the radiation intensity within its spectral acceptance:

$$V_0 = \int_{\bar{\nu}_{min}}^{\bar{\nu}_{max}} W(\bar{\nu}) d\bar{\nu}. \tag{3.6}$$

Here, $W(\bar{\nu})$ is the spectral distribution of the radiation and V_0 is the detector output voltage. If the ith filter is moved in front of the detector, the detector output is given by the spectrum $W(\bar{\nu})$ multiplied with the transmission function $t_i(\bar{\nu})$ of the filter:

$$V_i = \int_{\bar{\nu}_{min}}^{\bar{\nu}_{max}} W(\bar{\nu}) t_i(\bar{\nu}) d\bar{\nu}. \tag{3.7}$$

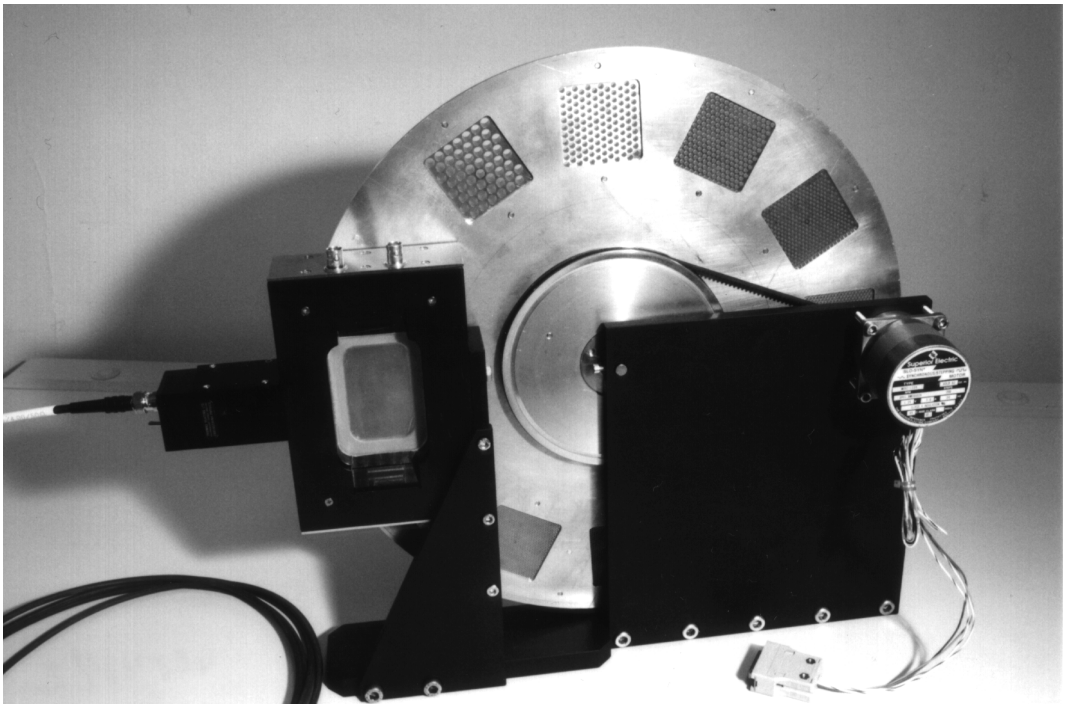

Figure 3.7: Experimental setup of the filter spectrometer with photo-acoustic detector.

Let $\mathbf{V}$ be the vector containing all the measured values, $\mathbf{W}$ is the vector containing the radiation power averaged in intervals given by the cutoff wave numbers of the filters and

$$\mathbf{V} = \mathbf{T}\mathbf{W}. \tag{3.8}$$

Instead of the transmission function of a single filter $t_i(\bar{\nu})$, now the transmission matrix $\mathbf{T}$ is used. $\mathbf{T}$ is a square matrix containing the transmission functions of all filters averaged in intervals given by the cutoff wave numbers:

$$\mathbf{T} := \begin{bmatrix} t_{11} & t_{12} & t_{13} & \cdots & t_{1n} \\ 0 & t_{22} & t_{23} & \cdots & t_{2n} \\ 0 & 0 & t_{33} & \cdots & t_{3n} \\ \vdots & \vdots & \ddots & \ddots & \vdots \\ 0 & \cdots & \cdots & 0 & t_{nn} \end{bmatrix}.$$

Here, the rows correspond to n filters and the columns correspond to the wave number intervals from $[\bar{\nu}_{c1}, \bar{\nu}_{c2}]$ to $[\bar{\nu}_{c(n-1)}, \bar{\nu}_{cn}]$. $\mathbf{T}$ is entirely determined by the properties of the filters and does not depend on a specific measurement.

The vector $\mathbf{W}$ can now be obtained from

$$\mathbf{W} = \mathbf{T}^{-1}\mathbf{V}. \tag{3.9}$$

It contains n values of the spectral intensity in the intervals given by the cutoff wave numbers of the filters.

In order to obtain the bunch length from a measured spectrum, charge distributions are generated and their spectra computed. The charge distribution is varied until computed and measured spectra are in good agreement. Then, the bunch length is obtained from the corresponding charge distribution. It should be noted that measuremens of the radiation power never contain the phase information which makes it impossible to transform the frequency domain measurements into the time domain. Therefore symmetric charge distributions must be assumed.

The resolution of a measurement with the filter spectrometer is given by the number of filters used. Taking into account the limited resolution and the frequency range covered by the filter spectormeter, only the first maximum of a bunch spectrum can be reliably measured. Therefore, a fit is performed to the first maximum of the spectrum. A Gaussian bunch shape, which results in a Gaussian shape of the spectrum as shown in Chapter 5, is a reasonable choice. Therefore, a Gaussian fit is performed to the first maximum and from this an estimate for the bunch length is obtained. Bunch length measurements using the filter spectrometer are discussed in Chapter 5.

3.2 Martin-Puplett Interferometer

Interferometers can serve as spectrometers for electromagnetic waves. The principle of these measurements is called Fourier spectroscopy. The main advantage of interferometers is their good resolution. Various kinds of intererometers can be used for spectroscopy in the far infrared. For the frequency range of interest here, a Martin-Puplett interferometer was used.

3.2.1 Fourier Spectroscopy

A two-arm Michelson interferometer as sketched in Fig. 3.8 splits up incoming radiation into two beams which are then brought to interference at variable path length difference. The radiation power is measured as a function of the path length difference s. From the interferogram, the frequency spectrum is obtained by applying a Fourier transform. The technique is therefore called Fourier spectroscopy (see for instance [34]).

The radiation power at the place of the detector is a function of the frequency spectrum of the radiation and the path length difference s of the two interferometer arms. The spectral power of the radiation is given by $dP/d\omega$. The variable path length difference of the interferometer arms causes a phase factor of $\exp\{i\omega\frac{s}{c}\}$ between the two beams. The frequencies superimpose as a function

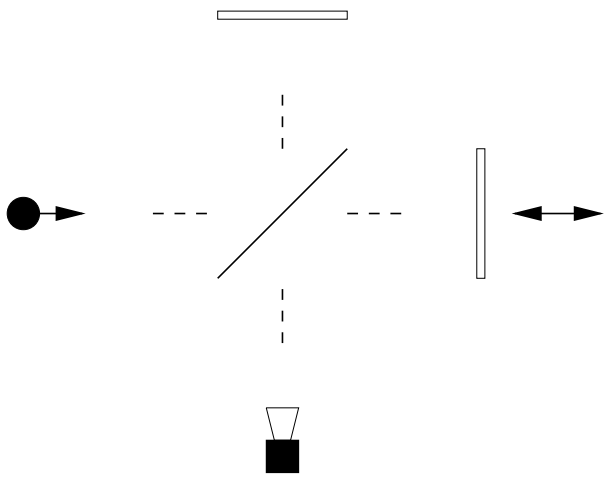

Figure 3.8: Quasi-optical diagram of a two-arm Michelson interferometer.

of s/c which results in an interferogram. The power measured by the detector is given by

$$P(t) = \int_0^\infty \frac{dP}{d\omega}\left[1 + \cos(\omega\frac{s}{c})\right] d\omega. \tag{3.10}$$

The function is a sum of a constant term

$$P_0 = \int_0^\infty \frac{dP}{d\omega}(\omega)d\omega \tag{3.11}$$

and a path length dependent term

$$P(s) = P_0 + \int_0^\infty \frac{dP}{d\omega}(\omega)\cos(\omega\frac{s}{c})d\omega. \tag{3.12}$$

It is readily seen that for a path length difference of $s = 0$ the measured power is $2P_0$. This is referred to as the zero position of the interferometer. If one of the interferometer arms is closed, the remaining power is just $P_0/2$.

The performance limits of an interferometer are determined by the maximum path length difference S and the stepwidth Δs with which the scan is performed. From the total travel distance of the movable mirror, the frequency resolution of the interferometer can be obtained. If the maximum travel distance of the movable mirror is S, the maximum time difference is given by $T = S/c$. The Fourier transform therefore resolves frequencies of

$$\Delta\omega = \frac{2\pi}{T} \tag{3.13}$$

or, in terms of wave numbers,

$$\Delta\bar{\nu} = \frac{1}{cT}. \tag{3.14}$$

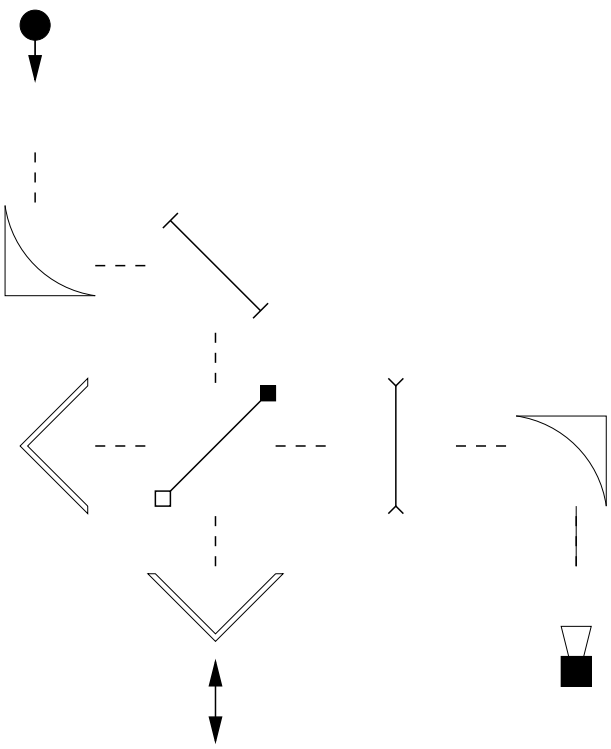

Figure 3.9: Quasi-optical diagram of the Martin-Puplett interferometer.

The stepwidth Δt, with which the interferometer scan is performed, gives an upper limit for the frequency that can be measured:

$$\omega_{max} = \frac{\pi}{\Delta t} \tag{3.15}$$

or

$$\bar{\nu}_{max} = \frac{1}{2c\Delta t}. \tag{3.16}$$

It should be noted, that these are theoretical performance limits. Due to systematic errors, the resolution of an interferometric measurement is in general worse.

3.2.2 Experimental Setup

Michelson interferometers for the far-infrared are frequently constructed as sketched in Fig. 3.8. The flat mirrors can be optical first-surface mirrors or glass

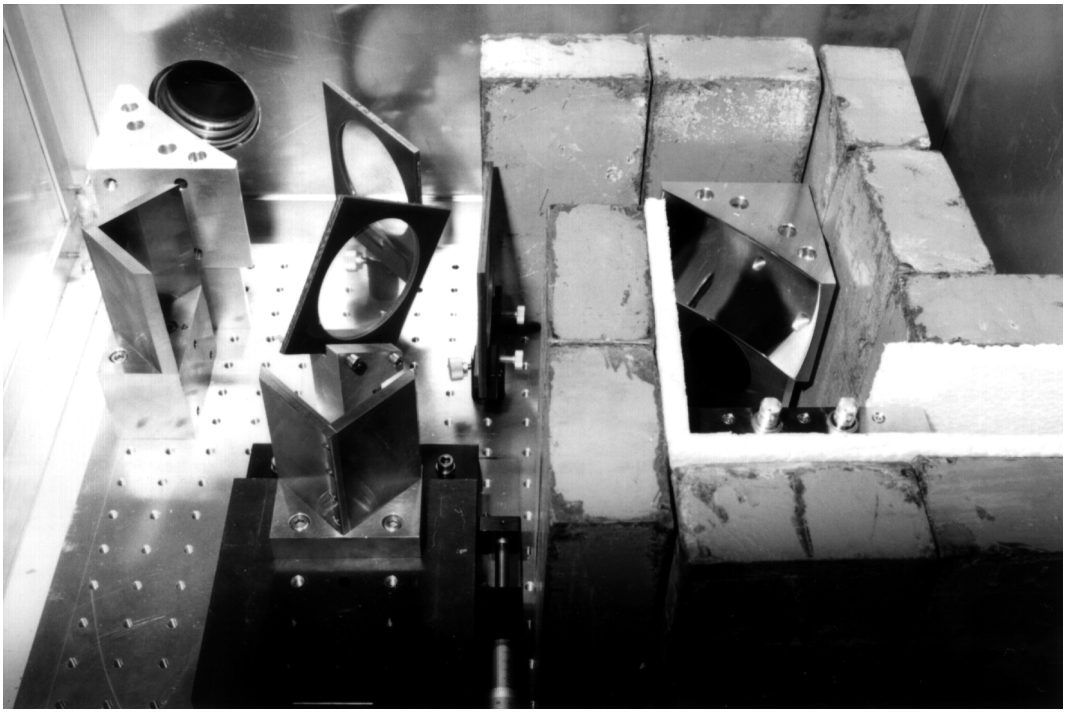

Figure 3.10: Experimental setup of the Martin-Puplett interferometer with photo-acoustic detector.

plates coated with a reflecting material, e.g. gold. A common beamsplitter material is Mylar. As shown in Chapter 2, Mylar does not have a flat beamsplitter efficiency but shows significant frequency-dependent variations. It is, on the other hand, desirable to have a spectrometer with a flat efficiency such that the effect of the instrument does not have to be deconvoluted from the measurement. Polarizing interferometers use systems of wire grid polarizers and reflectors instead of Mylar. An example is the Martin-Puplett interferometer [29], [35].

The Martin-Puplett interferometer is made of wire grid polarizers and roof-mirror reflectors. Figure 3.9 shows the schematical setup of the interferometer using the notation introduced in Chapter 2 and Fig. 3.10 shows the experimental setup. The interferometer is set up on a horizontal optical table. The incoming transition radiation falls on an off-axis paraboloid. The interferometer is arranged such that the radiation source is at a distance of 200 mm from the first focusing mirror. The off-axis paraboloid is machined from aluminum and hand-polished. The radiation is then reflected by a wire grid polarizer with the wires arranged vertically. The grids used for this setup are made from 20 μm tungsten wire at a spacing of 100 μm. The first grid reflects the polarization component with the electric vector oriented parallel with respect to the wires into the interferometer. The other polarization component is lost. This grid therefore acts as a polarizer.

The radiation is then passed to a second grid with the wires arranged at 45^o with respect to the polarization plane of the incoming radiation. This grid acts as a beamsplitter. It reflects half of the incoming radiation and transmits the other half of it. Since it is arranged at 45^o with respect to the beam axis, one polarization component is passed to a fixed roof mirror, while the other polarization component is passed to a movable roof mirror. It should be noted, that the angle of the wires must be 45^o viewed along the input beam axis. That means that the beamsplitter wires must be oriented at an angle of 35^o with respect to the plane of the optical table.

The roof mirrors reflect the radiation and at the same time alter the polarization state. That means that the half pulse that was first reflected by the beamsplitter passes it on its way back and the half pulse that was first transmitted through the beamsplitter is reflected by it. After the beamsplitter, both beams are superimposed again. They pass a third grid with its wires arranged horizontally with respect to the optical bench. This grid acts as an analyzer. The radiation is then focused onto the detector by a second ellipsoidal mirror.

One of the roof mirrors is movable by a stepper motor. The maximum travel distance is 50 mm with a stepwidth of 2.5 μm. Upon changing the optical path difference, one polarization component undergoes interference and hence the polarization state of the recombined beam is rotated. The analyzer selects a polarization component and the power measured by the detector as a function of the path difference yields the autocorrelation.

The Martin-Puplett interferometer features a flat efficiency over the whole millimeter wavelength range. Another advantage of the Martin-Puplett interferometer is that after the first polarizer all radiation power is directed to the detector and nothing is directed back to the source as in the case of the Michelson interferometer. All components have an aperture of 80 mm which avoids diffraction limitations at long wavelengths. The whole setup is installed on a 500 $\times$ 500 mm optical table and covered by an aluminum box.

Either the pyroelectric or the photo-acoustic detector described in Chapter 2 can be used in the interferometer. The detector output is amplified in the accelerator tunnel and the amplified signal transmitted to the control room where it is read out by an oscilloscope or an analog-digital converter (see Fig. B.4).

3.2.3 Analysis Algorithm

From the measured interferogram, the spectrum can be obtained using the fact, that the modulus squared of the Fourier transform of a pulse $f(t)$ equals the

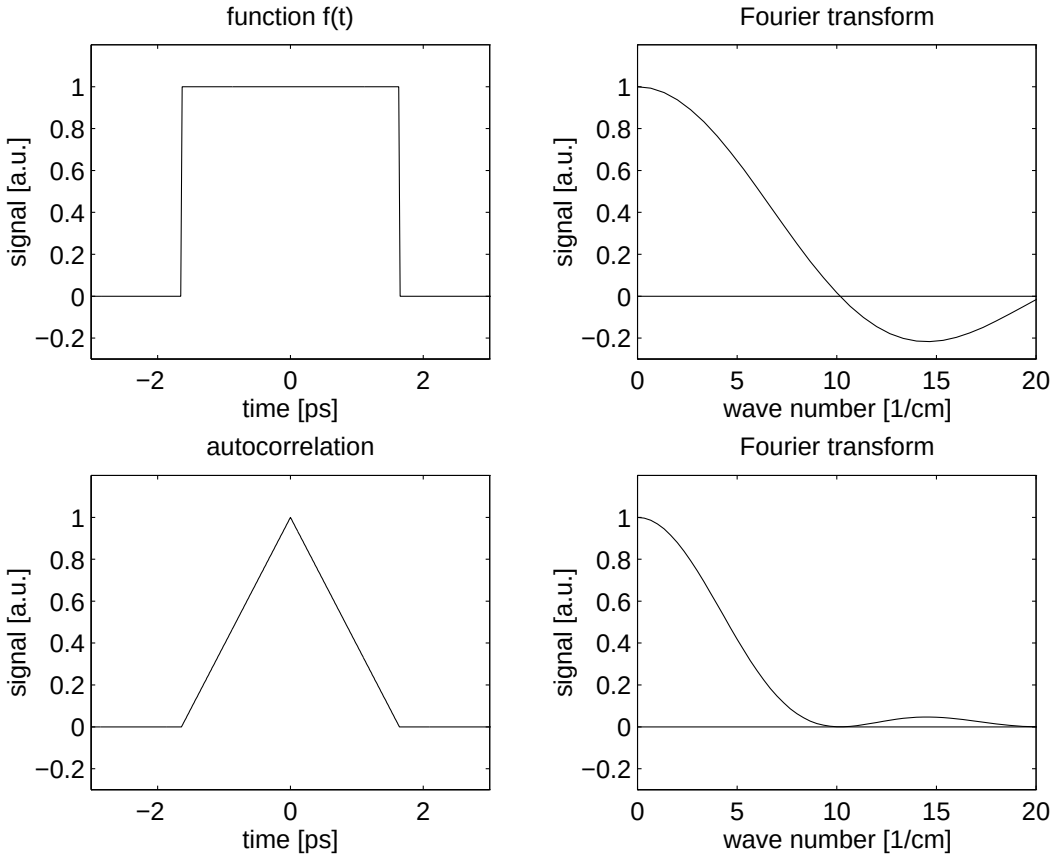

Figure 3.11: The modulus squared of the Fourier transform of a pulse $f(t)$ equals the Fourier transform of its autocorrelation function.

Fourier transform of its autocorrelation function $c_{ff}(t) = f(t) \odot f(t)$:

$$|F\{f(t)\}|^2 = F\{f(t) \odot f(t)\}. \tag{3.17}$$

Equation (3.17) is known as the Wiener-Khintchine relation [36]. It is illustrated for the special case of a flat pulse in Fig. 3.11.

By splitting up a radiation pulse into two equal parts and successively overlapping the two half pulses, the interferometer measures the autocorrelation function. For a flat charge distribution, for example, the autocorrelation is triangular shaped with a full width half maximum of the pulse length. This is strictly only true for an ideal spectrometer with a flat efficiency for all frequencies. Figure 3.12 shows in the upper left plot a flat charge distribution in the time domain and in the upper right plot its autocorrelation function. The autocorrelation function has been calculated without applying a filter, which corresponds to an ideal spectrometer. Any real instrument has a certain bandwith. A low frequency cutoff, given by the

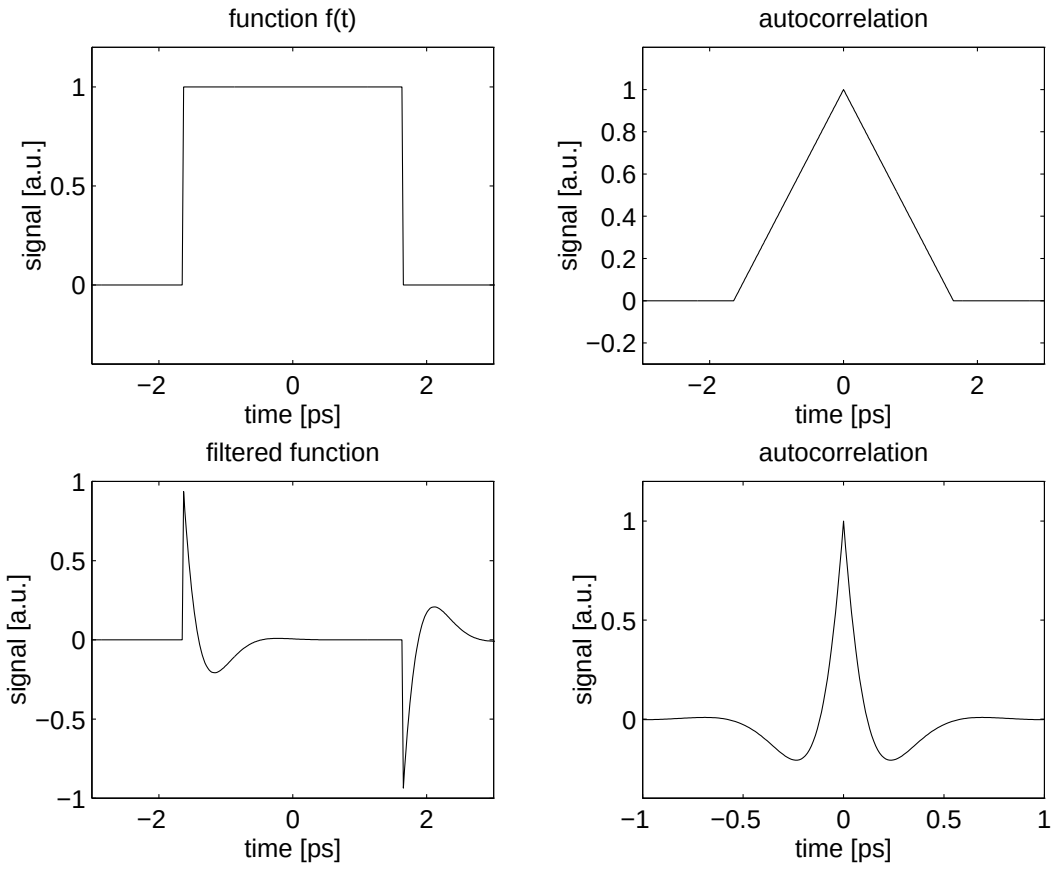

Figure 3.12: Pulse shape (upper left plot) and autocorrelation function (upper right plot). After applying a high-pass filter, which corresponds to a differetiation, the pulse shape changes (lower left plot). The corresponding autocorrelation function (lower right plot) has the same shape as the measured interferograms (see Chapter 5).

detector, can be simulated by applying a high-pass filter to the pulse. The lower left plot shows the pulse in the time domain after applying a high-pass filter and the lower right plot the corresponding autocorrelation function. As will be seen in Chapter 5, the measured autocorrelation functions have this shape.

The spectrum can be obtained by applying a numerical fast Fourier transform (fft) [37] to the measured interferogram. Since the power spectrum does not contain the phase information, the bunch shape cannot be directly obtained from the spectrum. A possible way to obtain the bunch shape is to generate charge distributions in the time domain and then to transform them into the frequency domain. If the calculated spectrum is in good agreement with the one obtained from the interferogram, the bunch shape and length can be obtained. Again the

principal restriction must be made that the phase information is lost and the analysis must be restricted to symmetric charge distributions.

For some charge distributions, the power spectrum is analytically known (see Chapter 1). These analytic functions can be used for a fit in the frequency domain and the corresponding charge distribution in the time domain be recalculated. For instance, the zeros of a $sin(x)/x$ function in the frequency domain yield directly the length of a flat charge distribution in the time domain.

Since often only the central maximum of the spectrum can clearly be seen, a Gaussian fit in the frequency domain is often a good choice. From the sigma of the distribution in terms of wave numbers, the frequency can be calculated using $\omega = 2\pi c\bar{\nu}$. The sigma of the distribution in the time domain is then simply $\sigma_t = 1/\omega$.

Chapter 4

Beam Diagnostics using Optical Techniques

Transition radiation in the optical frequency range is referred to as optical transition radiation (OTR). Besides simple imaging of the beam, also more information on the angular distribution and emittance can be obtained. By contrast to Čerenkov and synchrotron radiation, in the case of transition radiation the source is well defined by the interface of two media. This makes transition radiation a preferable diagnostic tool. The disadvantage of this method is, that one has to insert a target into the beam which decreases the beam quality.

4.1 Setup in the DESY Transfer Line

In order to study the potential of optical transition radiation for beam diagnostics, a setup was installed in the beam transfer line between the DESY II synchrotron and the DORIS storage ring at DESY.

At the place of the foil, the beam dimensions are $\sigma_x \approx \sigma_y \approx 1$ mm. The beam consists of positron bunches with $N = 10^{10}$ particles per bunch at an energy of $E = 4.65$ GeV. Measurements reported before were never carried out at this comparatively high energy. One of the aims of the experiment is therefore to show the applicability of optical transition radiation for beam diagnostics at high energy. Figure 4.1 shows the setup in the DESY transport line. An aluminum target can be moved into the positron beam using a pneumatic mover. Optical transition radiation is directed out of the vacuum chamber through a quartz window and focused on a CCD camera after reflection by 90^o using a remotely controllable mirror. The camera is housed in a lead shielding and has no direct view of the foil in order to protect it from X-rays. The objective of the camera was removed. Various combinations of lenses can be mounted on a vertical and a horizontal optical rail to focus the radiation directly on the CCD. A set of filters and polarizers can be remotely moved in front of the camera. A second

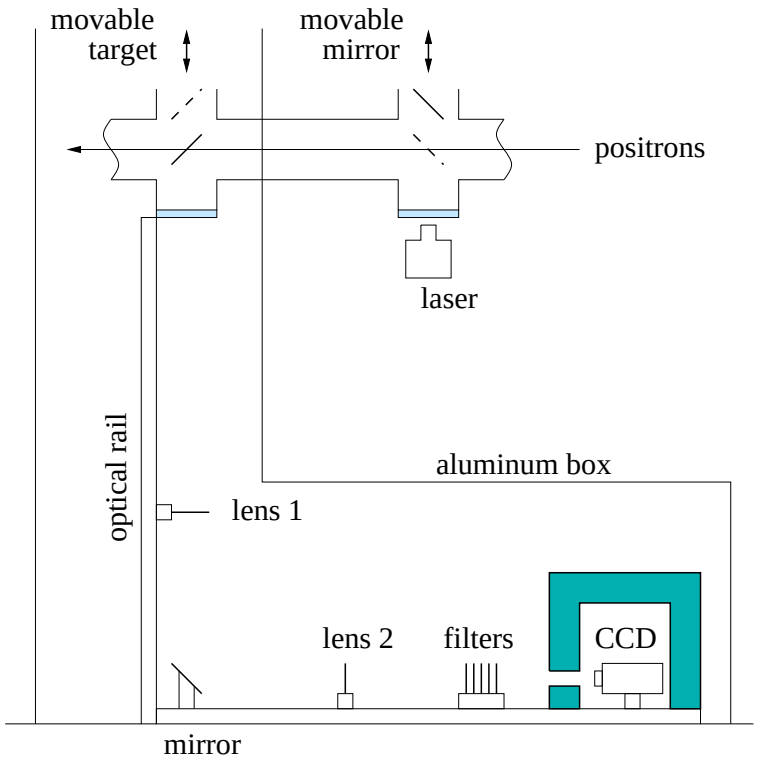

Figure 4.1: Setup for measurement of optical transition radiation in the DESY transport line.

window in the vacuum chamber is used to couple in an alignment laser, which is reflected along the particle beam trajectory by a snap mirror. The laser beam is directed out of the vacuum chamber by the OTR target and passes the whole optical setup.

4.1.1 Target

The target is a 20 nm aluminum layer on a 7.5 μm Kapton HN[1] (polyimide) film. Kapton is well suited as a support material as it is heat and radiation resistant. For a thin target (smaller than the radiation length, e.g. Al: 8.9 cm), the energy deposit per bunch passage in [J] can be obtained from

$$\Delta E = 1.5 \left[\mathrm{MeV cm^2 g^{-1}}\right] l\,[\mathrm{cm}]\, \rho \left[\mathrm{g cm^{-3}}\right] 1.6 \cdot 10^{-13} \left[\mathrm{J MeV^{-1}}\right] N, \qquad (4.1)$$

where the first factor is due to ionization losses, l is the thickness of the target material, ρ is the density of the material, $1.6 \cdot 10^{13}$[J MeV^{-1}] is the coefficient to transfer [MeV] to [J] and N is the number of particles in the bunch. The

[1]Trademark, DuPont S.A.

temperature rise per bunch passage is then given

$$\Delta T = \frac{\Delta E}{c\rho l A}, \tag{4.2}$$

where c is the specific heat capacity of the target material, m is the mass of the material heated and A the area hit by the bunch. This calculation is only correct for a homogenous particle distribution in the bunch. If the charge density is not homogenous, the temperature at the point of the highest density is higher.

For the beam parameters given above, one obtains a heating per bunch passage of 0.1 K for the aluminum and of 0.07 K per bunch passage for the Kapton which is not a critical value for this setup.

4.1.2 Camera and Readout

An image intensifier made by XYBION was chosen with a gating of 5 ns and a gain of up to 18000 [38]. The incoming photons are converted into electrons by a photocathode. The electron signal is then amplified by a multichannel plate (MCP) and converted back to photons by a phosphor screen. A CCD chip views the image on the phosphor screen.

The camera is gated by applying a bias voltage between the photocathode and the MCP which blocks the low energy electrons. Switching the bias voltage from -100 V to 200 V switches the camera 'on'. The trigger is flexible and allows to disable the CCD readout in order to integrate faint signals. The signals viewed by the CCD are digitized using a framegrabber. The bitmaps are then analyzed off-line using the package IDL (Interactive Data Language).

4.1.3 Calibration

In order to find the calibration factor from pixels to millimeters, the beam was swept over the target in x and y direction using two steerer dipoles. A set of beam positions was measured as a function of the dipole strength. The offset caused by the dipoles in [mm] at the place of the target can be calculated and the calibration factor in [px/mm] be obtained. Figure 4.2 shows the calibration measurements in both dimensions. The beam position on the CCD is plotted as a function of the calculated offset caused by the dipoles. A fit yields a calibration factor of 38.34 [px/mm] for the horizontal and 30.54 [px/mm] for the vertical calibration, which is consistent with the pixel size of 16 μm and a magnification of the optical system of 0.5.

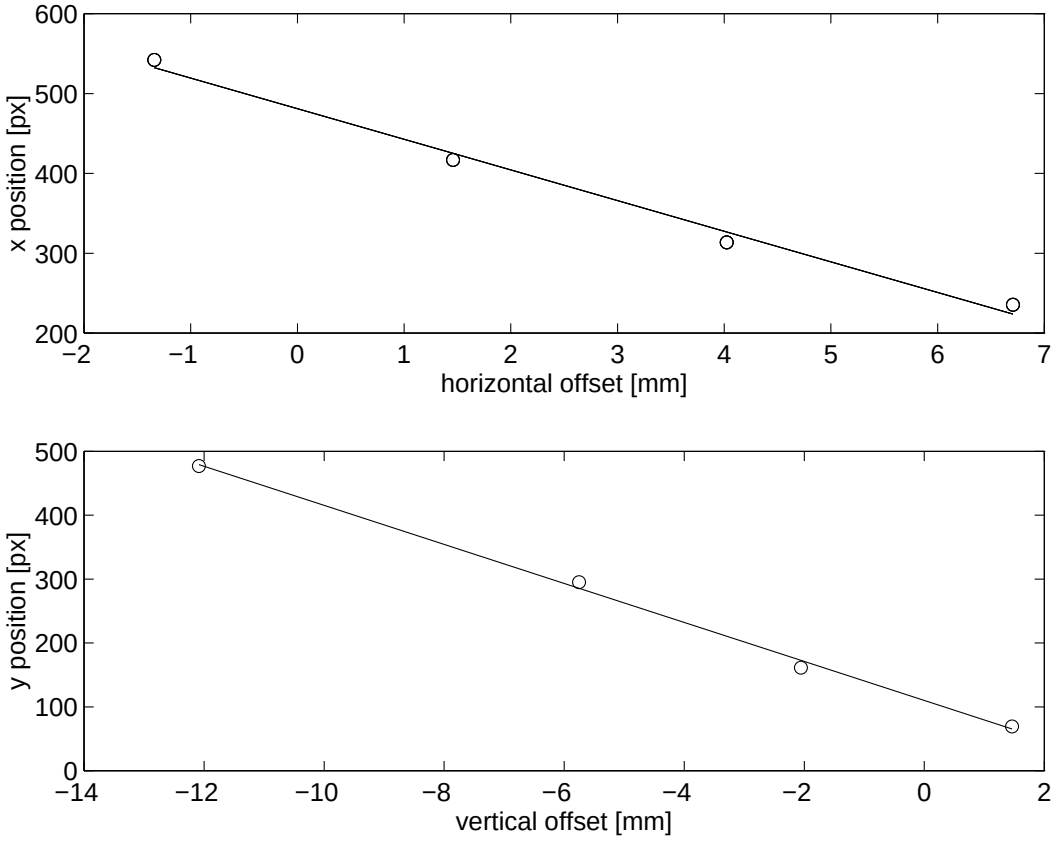

Figure 4.2: Beam position on the CCD versus offset produced by dipoles in x and y. The fit yields a calibration factor of 38.34 [px/mm] for the horizontal and 30.54 [px/mm] for the vertical calibration .

4.1.4 Beam Profile Measurement

The simplest optical technique is to image the beamspot on the target on a CCD camera. For a profile measurement one lens is needed. Figure 4.3 illustrates schematically, how the optical setup images the beam profile at the place of the foil on the CCD. It is readily seen, that different places on the OTR foil are imaged to different places on the CCD.
An achromatic lens with $f = 400$ mm was installed on an optical rail with a distance from the target of 1200 mm and a distance to the CCD of 600 mm. This system provides a magnification factor of $M = 0.5$.
From the image on the CCD, the transverse beam profile can directly be obtained. Therefore, the image is digitized and the distribution of pixels in x and y dimension read out. A Gaussian fit is performed to the distribution and the transverse beam size is obtained as the rms value. For a precise beam profile measurement,

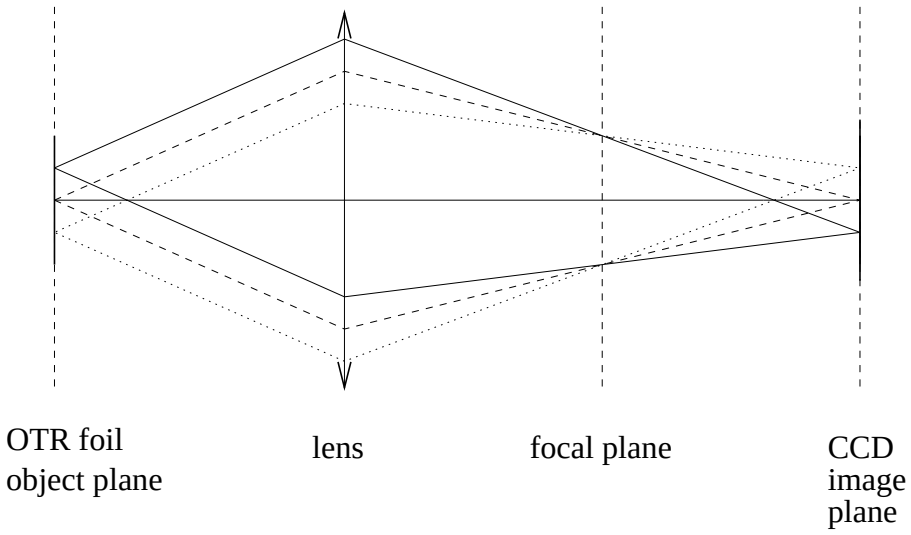

Figure 4.3: Optical setup to image the beam profile on a CCD. Different locations on the OTR foil correspond to different places on the CCD.

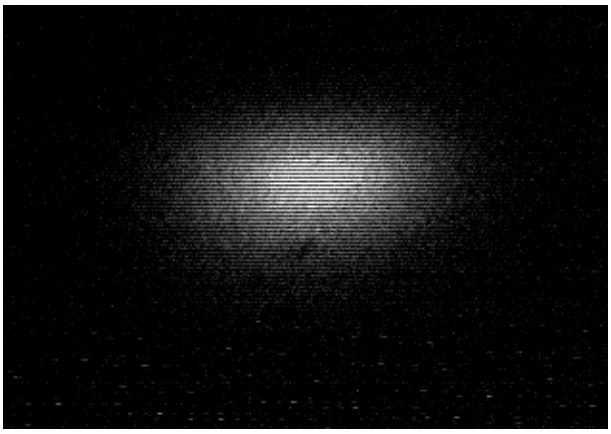

Figure 4.4: Typical beamspot obtained with optical transition radiation in the DESY transfer line.

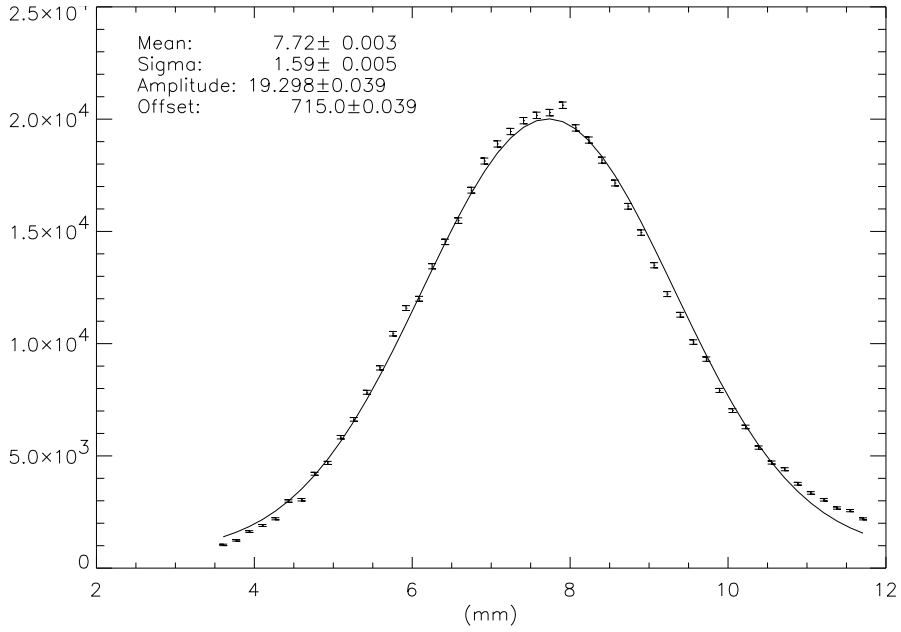

Figure 4.5: Typical horizontal beam profile measured in the DESY transfer line.

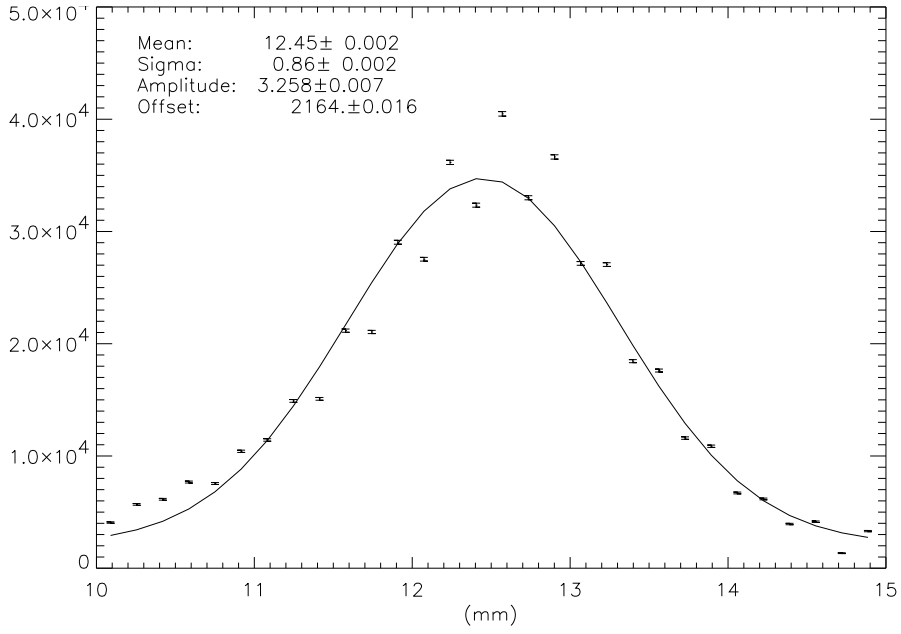

Figure 4.6: Typical vertical beam profile measured in the DESY transfer line.

a background image must be taken with the OTR target moved out of the beam and substracted from the beam image before analysing the intensity distribution. Figure 4.4 shows a typical image of the beamspot in the transport line and Fig. 4.5 and 4.6 show the corresponding x and y beam profiles.

4.1.5 Angular Distribution Measurement

The angular distribution of transition radiation yields directly the beam energy, since the opening angle is given by $1/\gamma$. An ideal optical transition radiation monitor would contain both the optics for beam profile measurement and for angular distribution measurement.
In order to measure the angular distribution of the transition radiation, two different optical setups can be used. Figure 4.7 shows schematically the two possibilities. A single lens can be used as in the case of beam profile measurement. The CCD is not in the image plane but in the focal plane of the lens. Alternatively, a system of two lenses can be used, where the CCD is in the focal plane of the second lens. In both cases, radiation emitted at different angles is imaged to different places on the CCD. The choice of the optical setup depends on the magnification that is desired.

Since the opening angle of the transition radiation at 4.65 GeV is only 110 μrad, a magnification of about $M = 8$ is required in order to achieve sufficient resolution on the CCD. For this purpose, a setup consisting of two lenses was used. A lens with focal length $f = 400$ mm was installed on the optical rail at a distance of 185 mm from the target and a second lens with focal length 120 mm was installed at a distance of 720 mm from the target. The total distance from the target to the CCD was, as in the case of beam profile measurement, 1800 mm. This system provides a magnification of $M = 8$.

A first attempt to resolve the two-lobe pattern at 4.65 GeV failed. The measured images did not have the expected shape. Further measurements could not be carried out so far. These measurements, successfully done at lower electron energies, are apparently not easy at small opening angles.

4.1.6 Quadrupole Scan

Optical transition radiation can be used to measure the beam emittance. Basically, two different methods can be applied: either the transverse beam dimensions are measured with a fixed screen but with several quadrupole settings or the beam profiles are measured at different places along the beamline with fixed beam optics. Since only one screen was available in our case, the quadrupole scan method was applied.
The beam size in x and y is measured as a function of the setting of a preceding

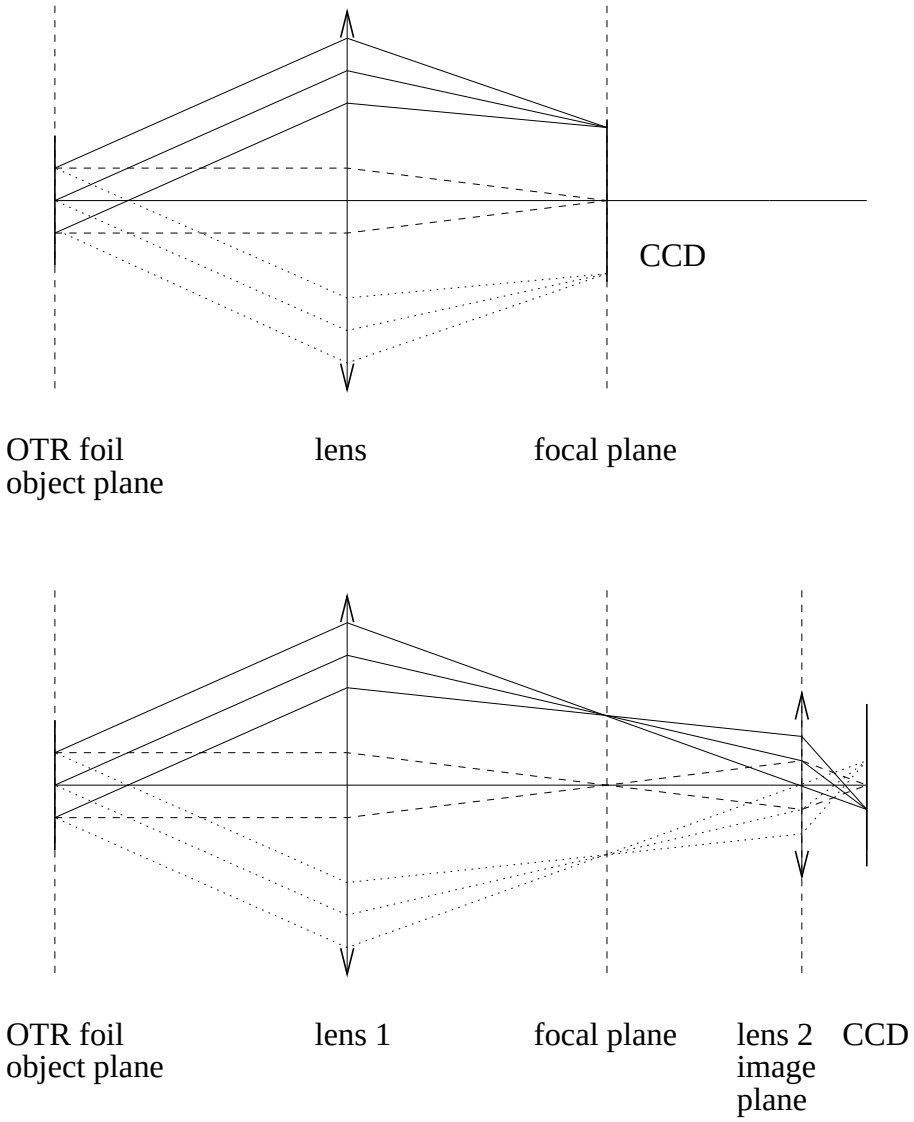

Figure 4.7: Two alternative setups to measure the angular distribution of optical transition radiation. Different angles of emission correspond to different places on the CCD.

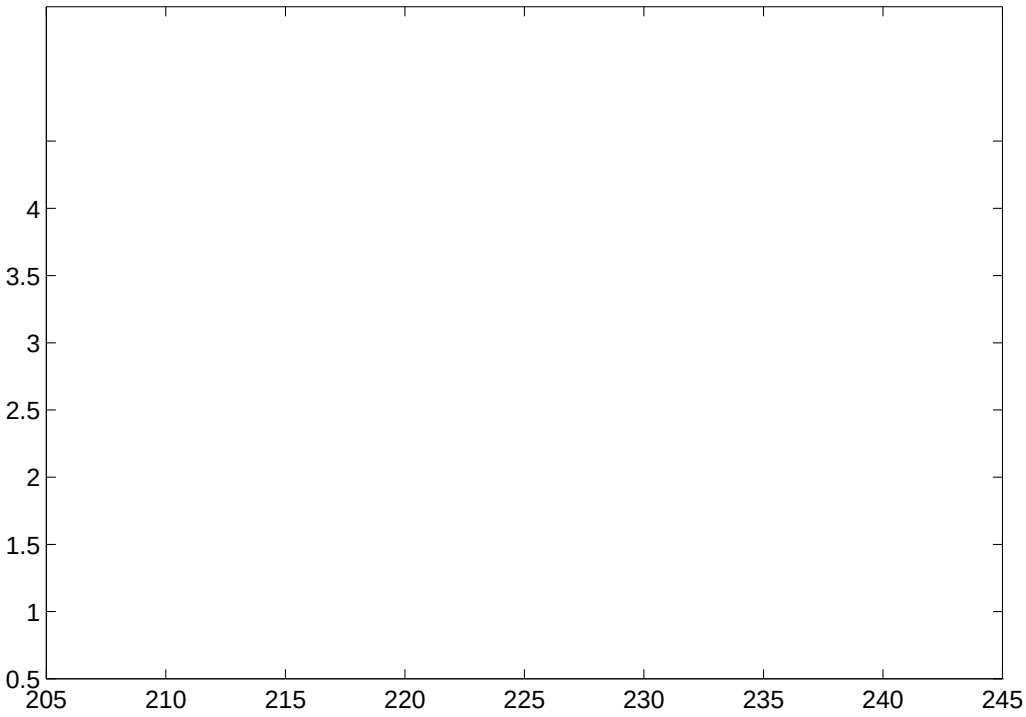
4
3.5
3
2.5
2
1.5
1
0.5
205
210
215
220
225
230
235
240
245

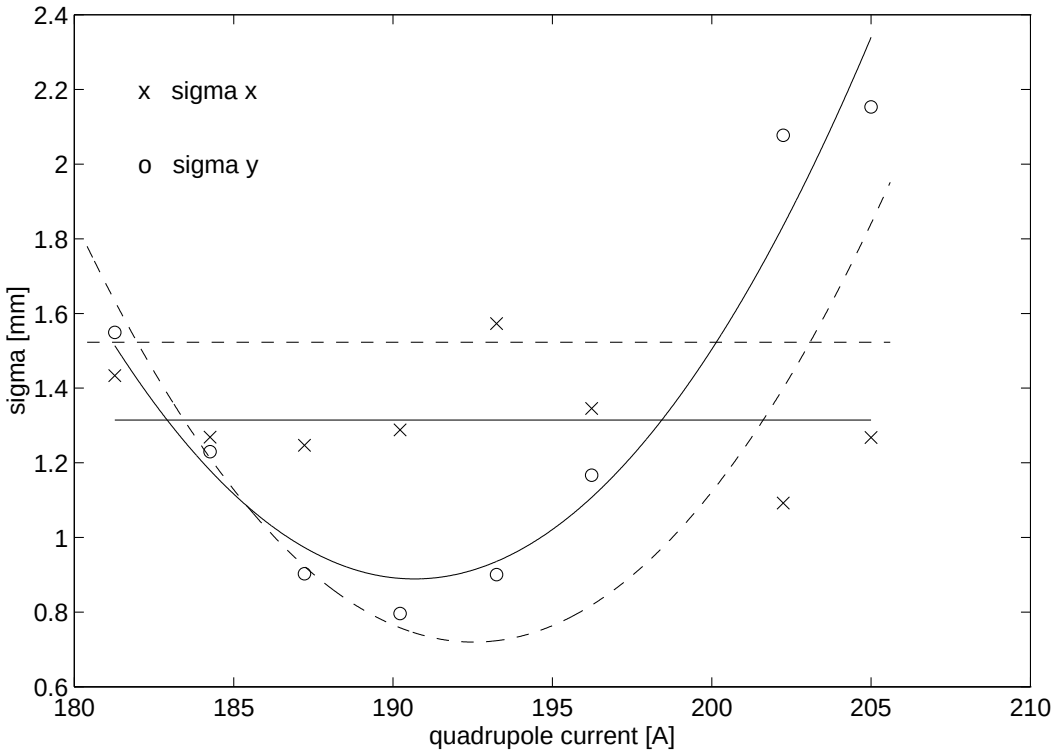

Figure 4.9: Quadrupole scan using the QR12 quadrupole. The solid line is a fit through the measured points, the dashed line is the theoretical expectation.

$$\gamma\epsilon \;=\; \frac{C_2C_3}{ab}r_1^2 - \frac{C_1C_3}{ac}r_2^2 + \frac{C_1C_2}{bc}r_3^2 \tag{4.4}$$

where we use $a = (C_1S_2 - C_2S_1)$, $b = (C_1S_3 - C_3S_1)$ and $c = (C_2S_3 - C_3S_2)$. We can therefore obtain the Twiss parameters from three measurements of the spot size and then obtain the beam emittance according to

$$\epsilon = \sqrt{(\beta\epsilon)(\gamma\epsilon) - (\alpha\epsilon)^2} \tag{4.5}$$

As can be seen from (4.3), the beam size is a parabolic function of the quadrupole gradient. Although in principle three measurements of the spotsize are sufficient for a parabolic fit, more data points improve the accuracy of the measurement.

In order to study the potential of optical transition radiation for such measurements, quadrupole scans were carried out using a vertically and a horizontally focusing quadrupole in the transfer line. The spotsize was measured as a function of the quadrupole current. Figure 4.8 shows the measured spotsize as a function of the current in the horizontally focusing quadrupole. The solid lines are fits

through the measured data points. The dashed lines show the caculated spotsize for the given quadrupole settings [40]. The x-profile changes rapidly as a function of the quadrupole current. A quadratic fit is in excellent agreement with the theoretical curve. The y-dimension is not influenced by the variation of the quadrupole current which proves good alignment of the quadrupole.
Figure 4.9 shows the measured spotsize as a function of the current in the vertically focusing quadrupole. The y-dimension of the beam changes as a function of the focusing. The fitted curve is in good agreement with the theoretical curve.

4.2 Longitudinal Bunch Imaging

The bunch length cannot be obtained by simple optical imaging because a CCD camera can only measure the transverse dimensions of an incident light beam. One possibility to obtain the bunch length is to measure light pulses emitted by the beam with a streak camera. A streak camera uses a photocathode which

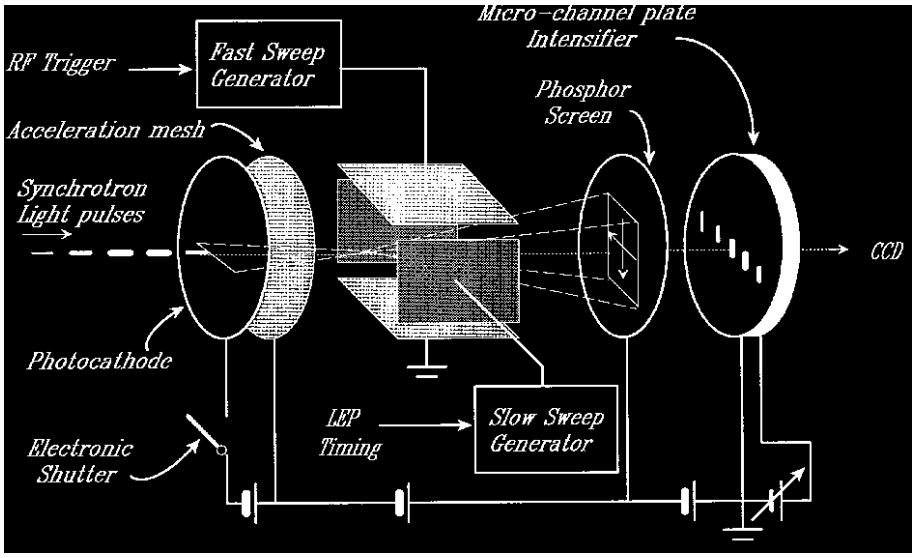

Figure 4.10: Principle of a streak camera as used at LEP.

converts light pulses into electron pulses. The electrons are then accelerated by a voltage and deflected by a rapidly increasing electric field (fast sweep) as they pass through a pair of deflection plates. The electron beam sweeps over a phosphor screen such that the time structure of the pulse is converted in deflection. The image on the screen is observed with a CCD. If the deflection field is switched off (focus mode), the streak camera records the transverse beam dimensions just as an ordinary CCD camera. A slower deflection voltage in the vertical direction (slow sweep) is optional. It allows to display successive bunches in the machine.

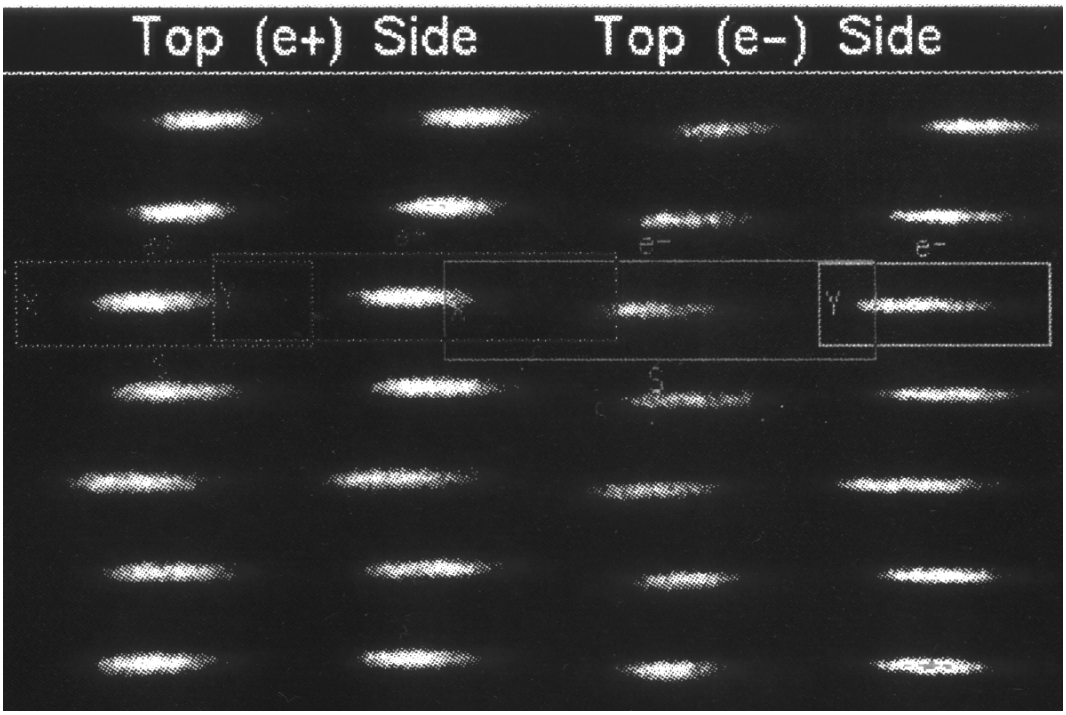

Figure 4.11: Top and side view of an electron and a positron bunch in LEP observed with a streak camera. Successive turns of the same bunch in the machine are displayed.

Streak cameras offer the unique possibility of single bunch observation in real time. A dedicated optical setup can be used to observe at the same time all three bunch dimensions and bunch instabilities as done at LEP. Figure 4.11 shows successive turns of an electron and a positron bunch in LEP [41]. On the left side, both top and side view of the electron bunch are displayed, on the right side both views of the positron bunch are displayed. The successive images correspond to successive turns of the same bunch.

The standard time resolution of streak cameras of about 1 ps has been improved significantly by the manufacturers. Fast streak cameras are now commercially available with a resolution of 180 fs. This might be even improved in the future. There are, however, reservations to be made. The time resolution specified by the manufacturers refers generally to monochromatic laser pulses and degrades by 10 - 20% for synchrotron or transition radiation. The high resolution for monochromatic light is obtained by matching the work function of the photocathode material to the quantum energy such that the photoelectrons are emitted with zero velocity. Such a selection using optical bandpass filters is usually not possible since not enough intensity is left.

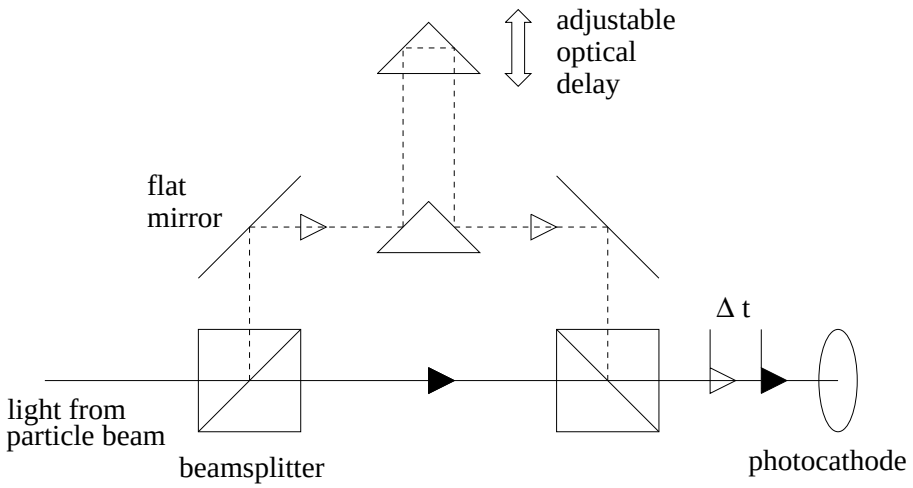

Figure 4.12: Setup to determine time resolution and fast sweep calibration of a streak camera.

There is a way to determine the resolution of a streak camera under given experimental conditions. The incoming light pulse is split into two pulses using a beamsplitter. One of the pulses is delayed with respect to the other such that they reach the photocathode at a well defined time difference. The resolution limit is reached, if the optical delay is adjusted such that the pulses are no longer separated by the streak camera. This measurement provides not only the resolution limit but also the calibration factor for the deflection voltage. Ideally the deflection voltage should be a sawtooth with a very steep and linear rise. The generation of this voltage is actually what determines the performance limit of a streak camera. In practice, a sinusoidal voltage is used where the middle part of the flank is used for deflection. The linearity can be verified by measuring the separation of the pulses on the CCD as a function of the optical delay. This yields the calibration factor for the fast sweep in number of pixels swept per picosecond.

Another effect becomes important if the streak camera is operated without a slit in front of the photocathode which is necessary for beam imaging since the whole light pulses must be observed in order to obtain the correct intensity distribution. In this case, the time resolution depends on the spot size. The finite extension parallel to the fast deflection broadens the measured longitudinal profile. For a Gaussian bunch shape, the true and the measured longitudinal bunch dimensions are related by

$$\sigma_z = \sqrt{\sigma_m^2 - \sigma_x^2}, \tag{4.6}$$

where σ_z is the true bunch length, σ_m is the measured bunch length and σ_x is the transverse spot size in the direction of the fast sweep [42].

Time domain measurements using a streak camera have shown to work very well for bunch lengths of several tens of picoseconds. For picosecond bunches as in a linear accelerator, the resolution limit is reached. In the case of sub-picosecond bunches as required for the operation of free-electron lasers, time resolving electronics is presently not available.

Chapter 5

Beam Diagnostics using Coherent Transition Radiation

Coherent transition radiation was observed and used for diagnostics of electron beams in linear accelerators. Measurements were carried out at the CLIC test facility at CERN, at the S-DALINAC in Darmstadt and at the TESLA test facility at DESY. The spectrometers described in Chapter 3 were used to determine the bunch length.

5.1 Measurements at the CLIC Test Facility

5.1.1 The CLIC Test Facility

The CLIC test facility at CERN is a prototype accelerator for the Compact Linear Collider (CLIC) design. The aim of the CLIC design is to provide an acceleration gradient of 80 MV/m using normalconducting structures operated at 30 GHz. Since no clystrons are available at this frequency, the two-beam scheme was chosen. A drive beam produces 30 GHz rf power which is coupled out and used to accelerate the beam in the main linac. In order to optimize the rf power gain, the drive beam must provide high bunch charge and a short bunch length. As operated in 1995, the CLIC test facility (CTF) should provide a drive beam with these specifications [43].

In order to produce short bunches with a high charge, a laser injector is used together with a magnetic bunch compressor [44]. Figure 5.1 shows a sketch of the CLIC test facility as it was operated in 1995.

5.1.2 Experimental Setup

Transition radiation is produced by moving thin, polished aluminum plates into the beam line. Transition and Čerenkov monitors (TCM) are distributed along

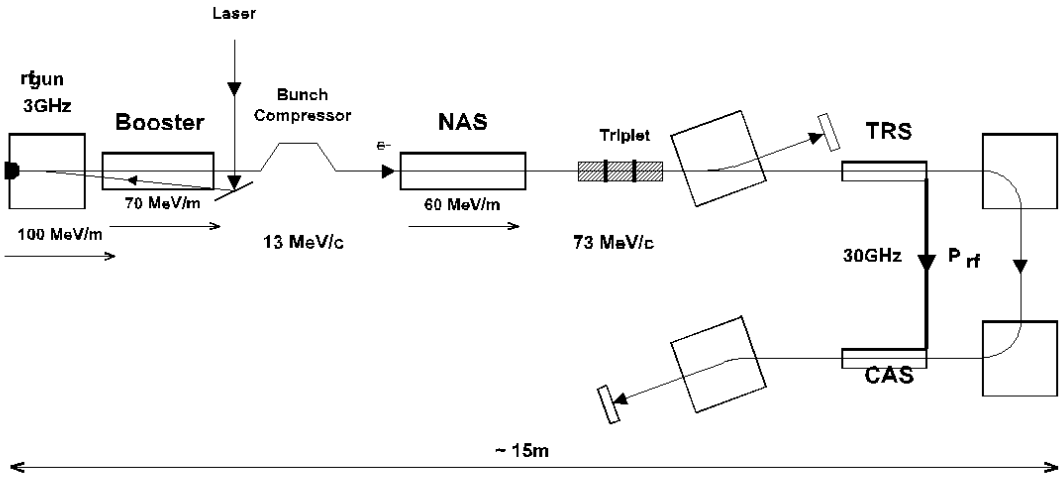

Figure 5.1: Schematic view of the CLIC test facility as operated in 1995. NAS: 3 GHz acceleration section; TRS: 30 GHz transfer structure; CAS: 30 GHz acceleration structure.

the machine for optical diagnostics [45]. The radiation is directed out of the vacuum chamber through sapphire windows. The measurements reported here were carried out behind the bunch compressor at a beam energy of 12 MeV. The machine was operated with bunch trains at a repetition rate of 10 Hz. The number of bunches per train and the individual bunch charge could be varied [46].

The photo-acoustic detector was placed directly on top of the sapphire window of a transition radiation setup. It was carefully shielded against electromagnetic noise, acoustic noise and vibrations. The signal was transmitted to the control room via a coaxial cable and measured with an oscilloscope.

5.1.3 Observation of Coherent Transition Radiation

The transition radiation was detected with the photo-acoustic detector. Figure 5.2 shows the detector signal observed from a train of 24 bunches with a bunch spacing of 333 ps. The detector cannot resolve the time structure of the bunch train. One can clearly see its temporal behaviour: the foil warms up quickly as the train passes. The decay then takes several milliseconds. The oscilloscope was triggered on the beam and averaged over 32 single measurements.

The total detector output is the sum of the coherent transition radiation signal and background. When the target is moved out of the beamline, the signal decreases but does not totally vanish. The remaining background is due to fields of

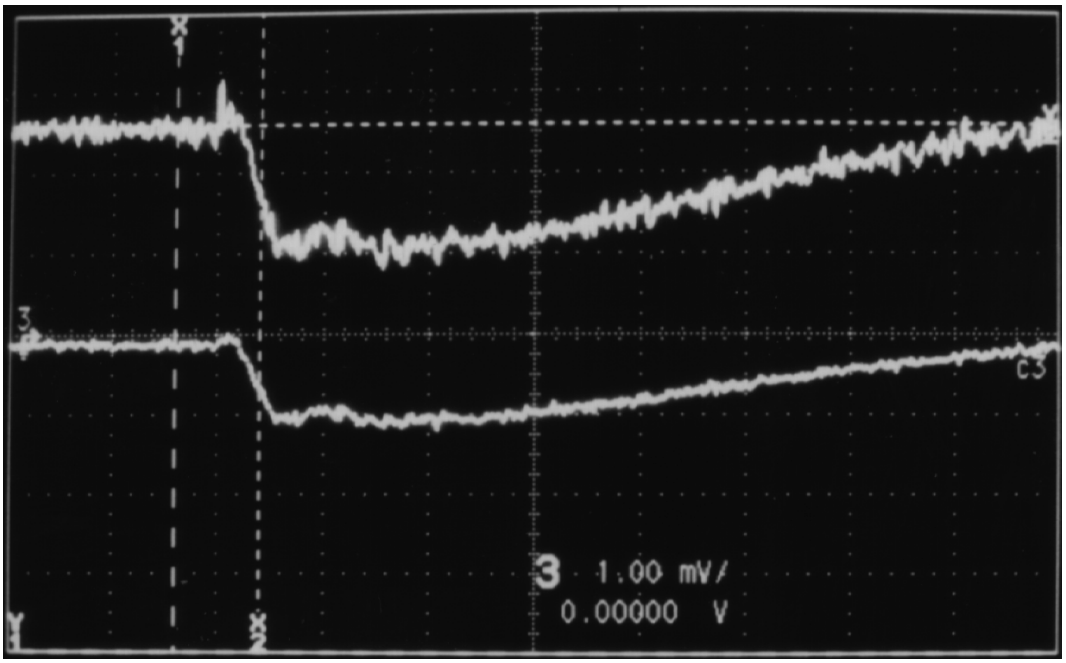

Figure 5.2: Detector output from a train of 24 bunches. The oscilloscope shows voltage versus time. The total time axis is 10 ms. The upper curve represents the total signal while the lower curve is the pure transition radiation signal after background subtraction.

the bunches that leak out of the vacuum window and are seen by the detector. The measurement procedure therefore has to be repeated with transition radiator moved out of the beam as a background measurement. The background is then subtracted to obtain the pure coherent transition radiation signal. The upper curve in Fig. 5.2 is the total signal, whereas the lower curve is the signal after background subtraction.

5.1.4 Optimization of Bunch Compressor Setting

Changing the bunch length shifts the onset of the coherence effect. For a short bunch, a larger part of the coherent spectrum will be found within the spectral range of the detector than for a long bunch. This results in a change of the detector output and hence can be used for optimizing the machine to short bunches.

The setting of the CTF machine was optimized using the detector output. With the bunch compressor switched off, no coherent transition radiation could be observed. For a setting of the bunch compressor at 25 A the detector output could be maximized. For comparison with the optimized machine setting a second, non-optimized setting was used with the bunch compressor at 21 A.

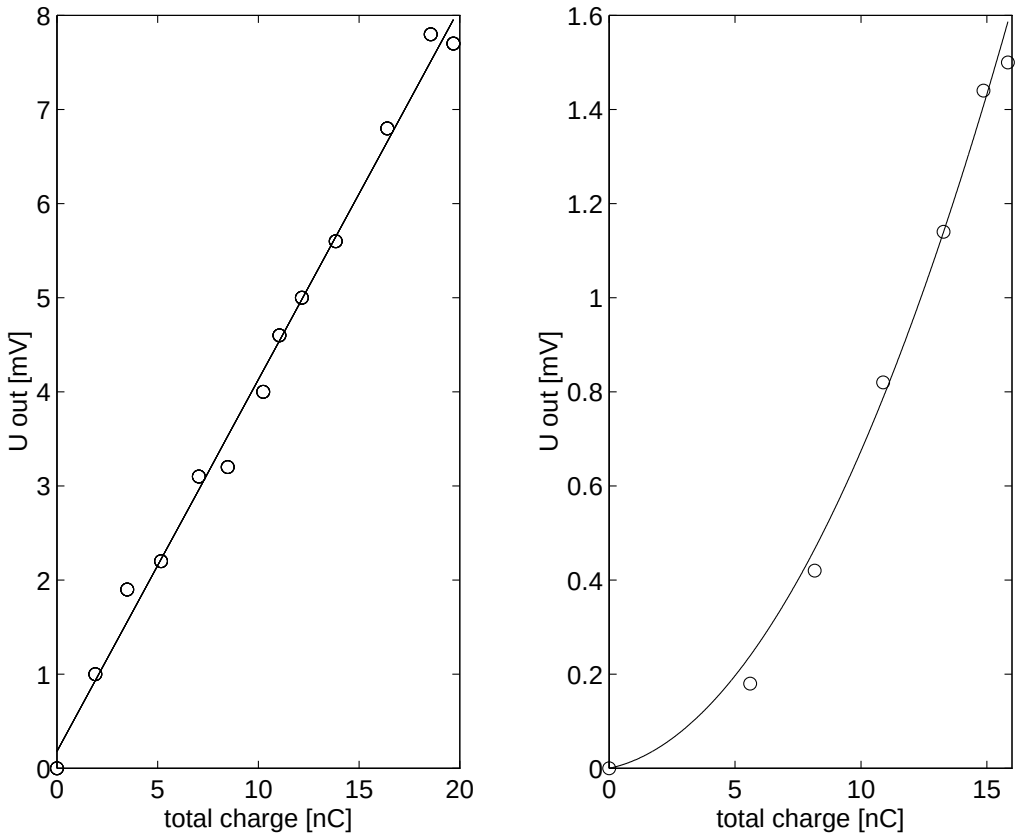

Figure 5.3: Left plot: detector output versus total beam charge for different numbers of bunches in a train. The first value is taken with one single bunch, then bunches are added successively until the train consists of 12 bunches. Right plot: detector output versus total beam current for increasing single-bunch charge. The number of bunches in the train is kept constant to 24.

5.1.5 Observation of Coherence Effect

The number of bunches per train was increased, leaving the single bunch charge constant. One expects a linear increase of the signal, since adding bunches does not lead to a coherence effect. The left plot in Fig. 5.3 shows signal versus charge for different numbers of bunches in the train. The first value is taken with a single bunch. Then, bunches are added successively until the train consists of 12 bunches. The detector signal increases linearly with the charge.

Adding charge to each single bunch and leaving the number of bunches constant results in a non-linear increase in detector voltage. The right plot in Fig. 5.3 shows signal versus charge for a train of 24 bunches. The charge per single bunch is increased, and the signal increases non-linearily with the charge. The

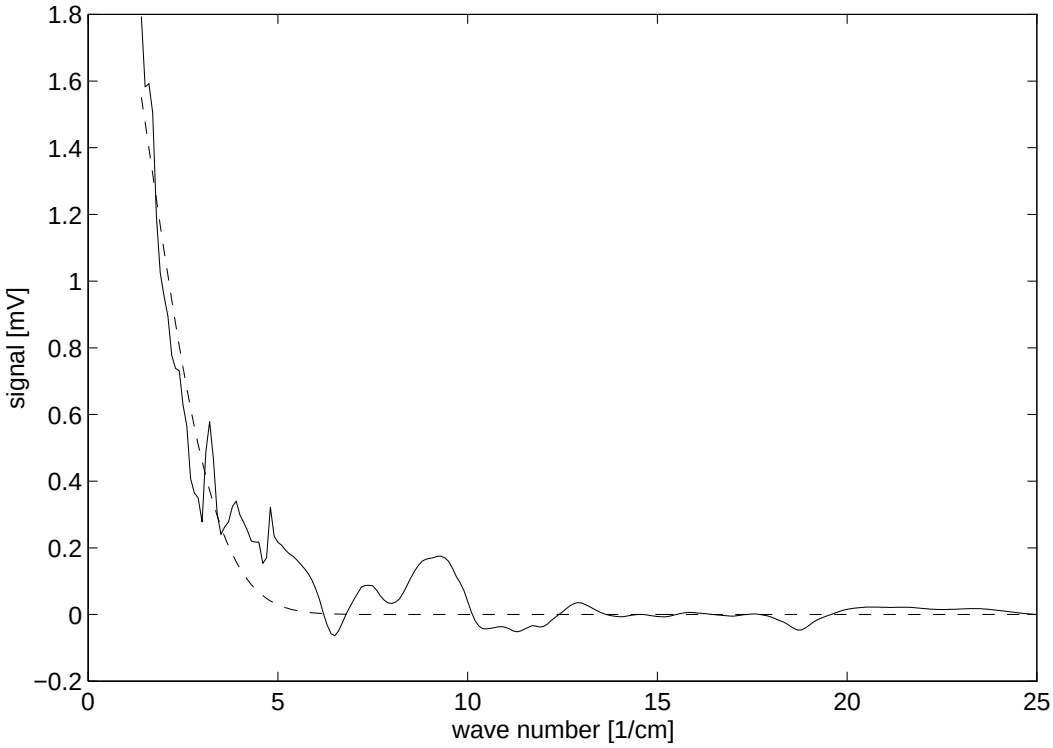

Figure 5.4: Spectral intensity versus wavenumber for non-optimized machine setting. A Gaussian fit yields $\sigma = 3.12$ ps (dashed line).

experimental results are in good agreement with the theoretical prediction. The beam optics was not changed during the experiments reported above.

5.1.6 Measurements with Filter Spectrometer

The spectrum of the coherent transition radiation was measured using the high-pass filters described in Chapter 2. From its shape and decay, the bunch length can be obtained. The spectrum was measured for both the optimized and non-optimized bunch compressor setting. Figure 5.4 shows the power spectrum for the non-optimized machine setting and Fig. 5.5 for the optimized machine setting.

A Gaussian fit is performed to the first maximum of the spectrum with the center of the distribution at $\bar{\nu} = 0$ cm^{-1} (dashed lines). From the sigma of the Gaussian distribution in the frequency domain, the sigma of the charge distribution in the time domain can directly be obtained as $\sigma_t = 1/\omega$, where $\omega = 2\pi c\bar{\nu}$. Assuming a Gaussian charge distribution, the fit yields $\sigma = 3.12$ ps for the non-optimized and $\sigma = 2.18$ ps for the optimized bunch compressor setting.

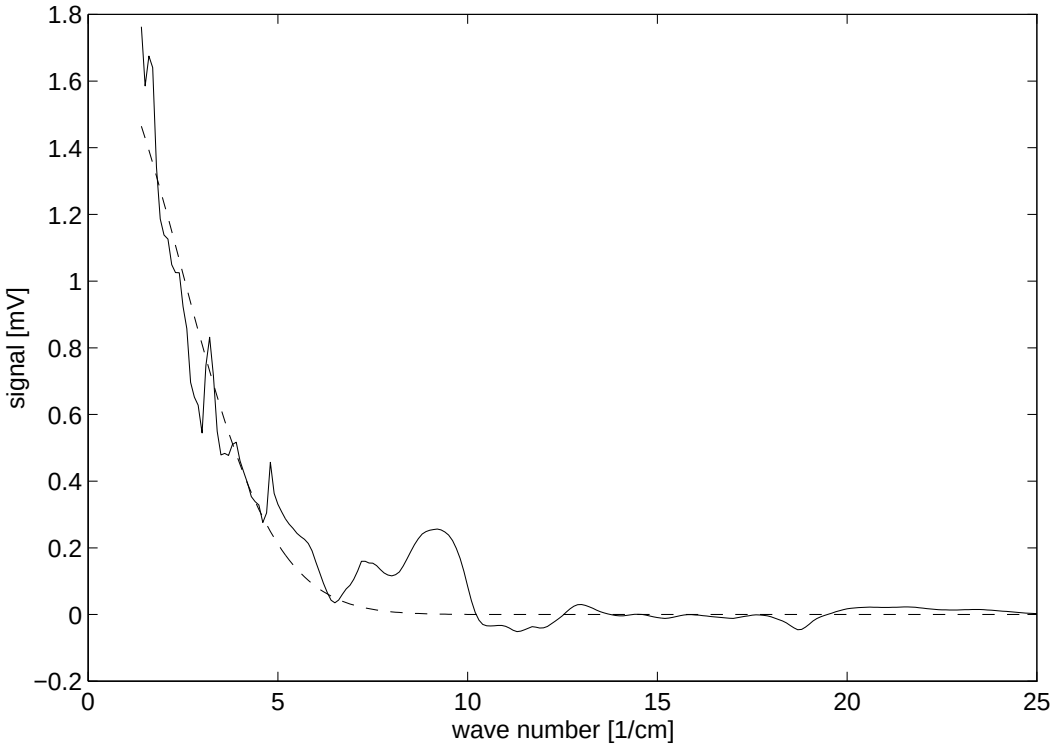

Figure 5.5: Spectral intensity versus wavenumber for optimized machine setting. A Gaussian fit yields $\sigma = 2.18$ ps (dashed line).

5.1.7 Streak Camera Measurements

For the two bunch compressor settings, the bunch length was directly measured with a streak camera. Therefore, Čerenkov radiation in the visible frequency range was directed on a streak camera with a nominal resolution of 2 ps made by ARP [47]. The light is directed through the roof of the accelerator building into an optical laboratory.

A series of streak camera measurements was performed for both the optimized and the non-optimized machine setting. Figure 5.6 shows a measurement of a 3.1 ps bunch at optimized setting of the bunch compressor. The plot shows the intensity in arbitrary units versus pixels. The whole range of the CCD is displayed on the upper plot, while the region of interest is shown on a different scale in the lower plot.

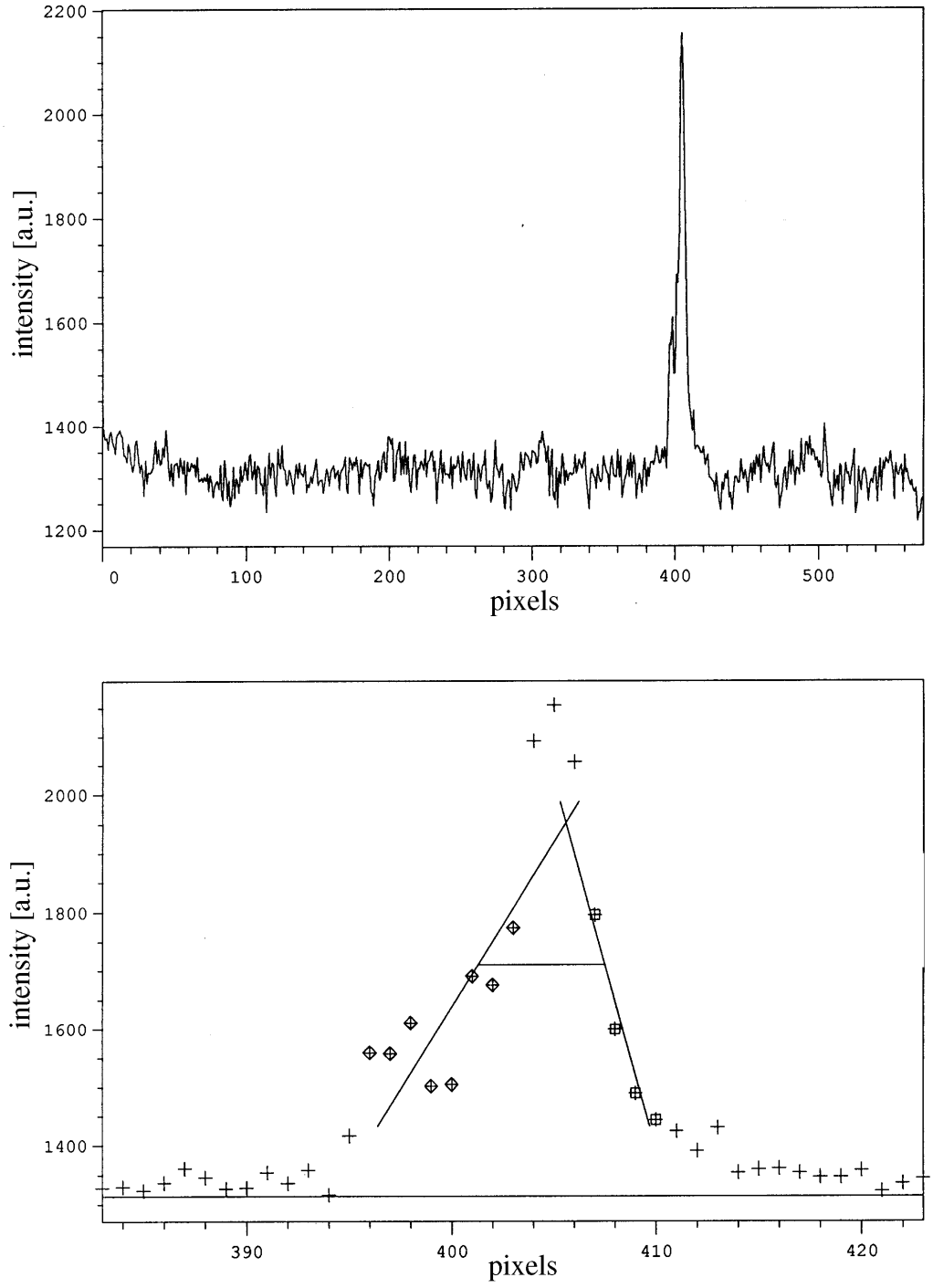

Figure 5.6: Single-shot streak camera measurement of a 3.1 ps bunch at the CLIC test facility.

5.1.8 Comparison of Spectroscopic with Streak Camera Measurements

The single-shot streak camera measurements vary from bunch to bunch and cannot directly be compared with the integrating spectroscopic measurements. They were therefore superimposed for comparison with the measurements of the coherent spectra. Figure 5.7 shows the integrated streak camera measurements for the two machine settings. While the charge distribution of the single shot measurements is somewhat arbitrary, the integrated plots show a Gaussian profile. A Gaussian fit yields $\sigma_t = 3.55$ ps for the non-optimized and $\sigma_t = 2.6$ ps for the optimized setting. Table 5.1 shows the bunch length obtained from the coherent transition radiation signal and from the streak camera measurements. The results from both methods are in agreement within 15%. The fact that the streak camera yields higher values might be due to its limited resolution.

bunch compressor setting	A	B
σ_t streak camera [ps]	2.6	3.55
σ_t coh. radiation [ps]	2.18	3.12

Table 5.1: Comparision of bunch length obtained from the coherent transition radiation spectrum and from a streak camera.

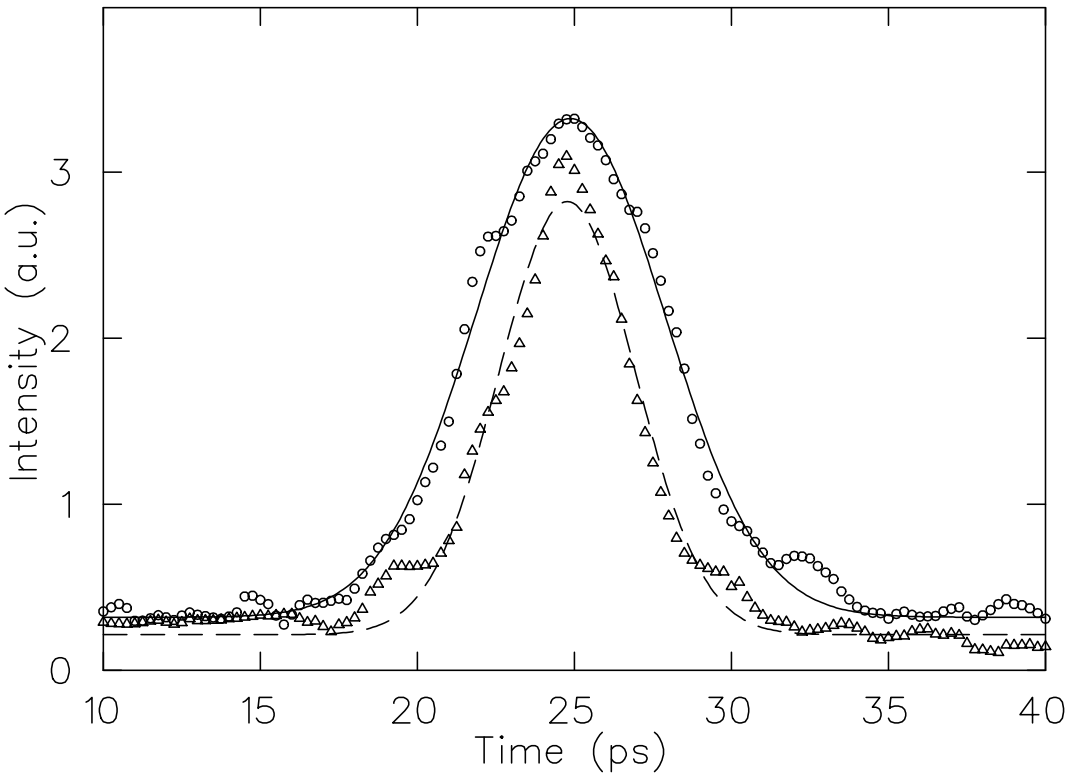

Figure 5.7: Streak camera measurements for optimized (triangles) and non-optimized (circles) machine setting. The single-shot measurements were superimposed and the rms bunch length determined. A Gaussian fit yields a bunch length of 3.55 ps (solid line) and 2.6 ps (dashed line) respectively.

5.2 Measurements at the S-DALINAC Facility

5.2.1 The S-DALINAC Facility

The S-DALINAC facility at the Institut für Kernphysik, Technische Hochschule Darmstadt, is a superconducting linear accelerator operated at an acceleration frequency of 3 GHz. It is both used for nuclear physics experiments and as a driver for a free-electron laser. As can be seen in Fig. 5.8, the S-DALINAC is a recirculating machine. The electron beam is generated by a thermionic gun and accelerated in an electrostatic acceleration section to 250 keV. A chopper-prebuncher system conditions the beam for further acceleration. The superconducting injector consists of a capture section of a 2-cell and a 5-cell superconducting cavity followed by two 20-cell cavities which provide a maximum energy of 10 MeV.

The beam can at this point either be extracted and used for nuclear physics experiments or be injected into the 40 MeV main accelerator. The main linac provides with two recirculations an energy of up to 130 MeV. The undulator of the free-electron laser is installed as a bypass of the first recirculation beamline. At the end of the linac, the electron beam can be extracted and used for nuclear physics experiments at high energy.

The S-DALINAC machine can be operated both in cw and pulsed mode. While for nuclear physics a continous beam is generated, the free-electron laser requires a high bunch charge which cannot be provided continously. Therefore, the electron gun is chopped at 10 MHz such that every 300^{th} bucket is filled. This provides a higher peak current while the average beam current is unchanged. From the 1 ns long pulses produced by the cathode, 370 ps bunches are cut out by a 600 MHz subharmonic chopper. A 600 MHz prebuncher causes an energy modulation such that the electrons converge to bunches of about 5 ps in the drift space to the injector.

5.2.2 Experimental Setup

The measurements reported here were carried out behind the injector at an electron beam energy of 10 MeV. The electron beam consisted of macropulses of 4 ms duration at a repitition rate of 31 Hz. Each macropulse consisted of 2×10^5 single bunches and each single bunch of 10^7 particles.

The transition radiation target is an aluminum foil that can be moved into the electron beam by a pneumatic mover. The backward transition radiation is directed out of the vacuum chamber through a quartz window into a Martin-Puplett interferometer. For the signal detection, both the Thomas Keating photo-acoustic detector and a Molectron P1-45 pyroelectric detector [19] were used. The detector output is read out by a boxcar integrator.

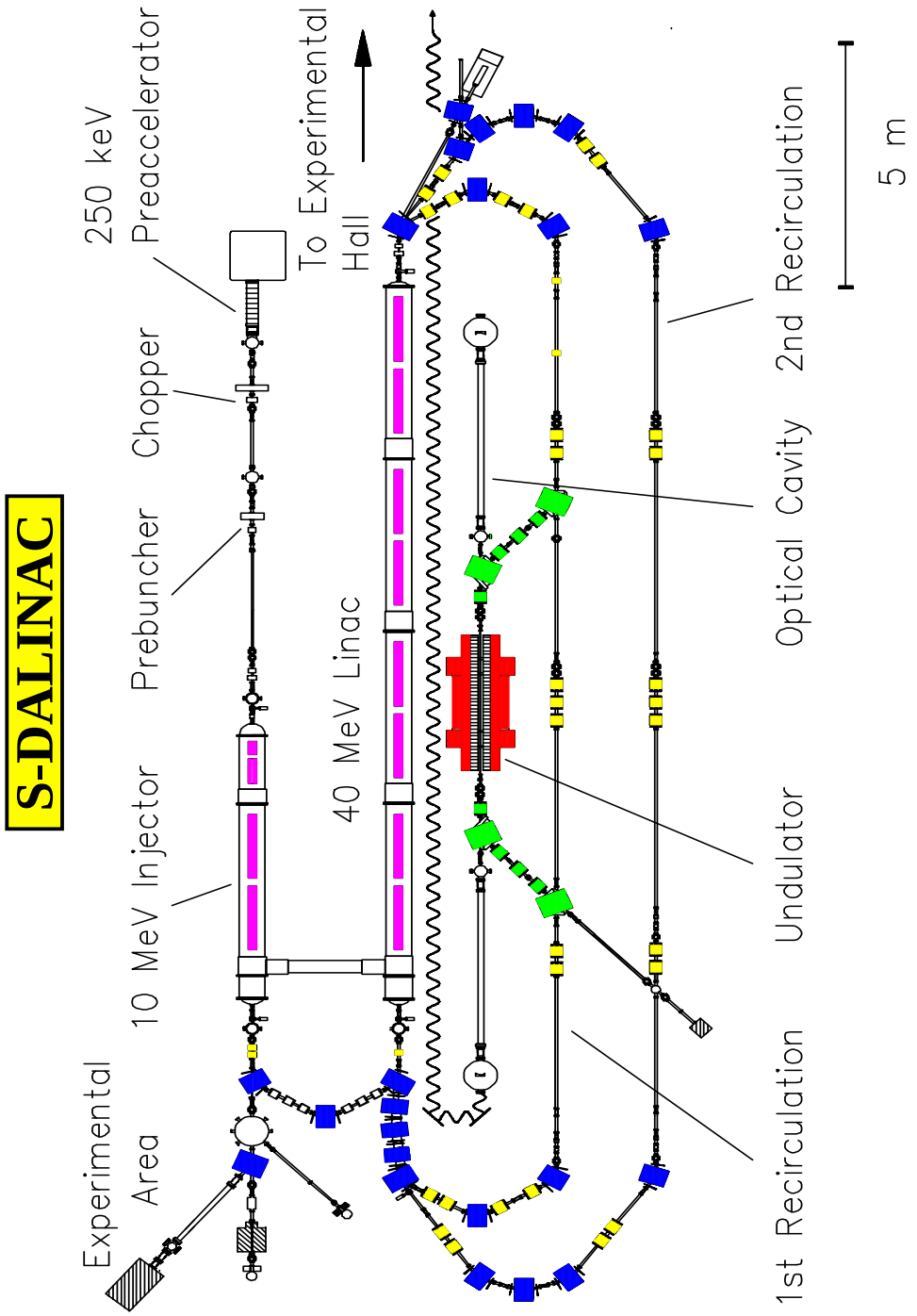

Figure 5.8: The S-DALINAC recirculating accelerator.

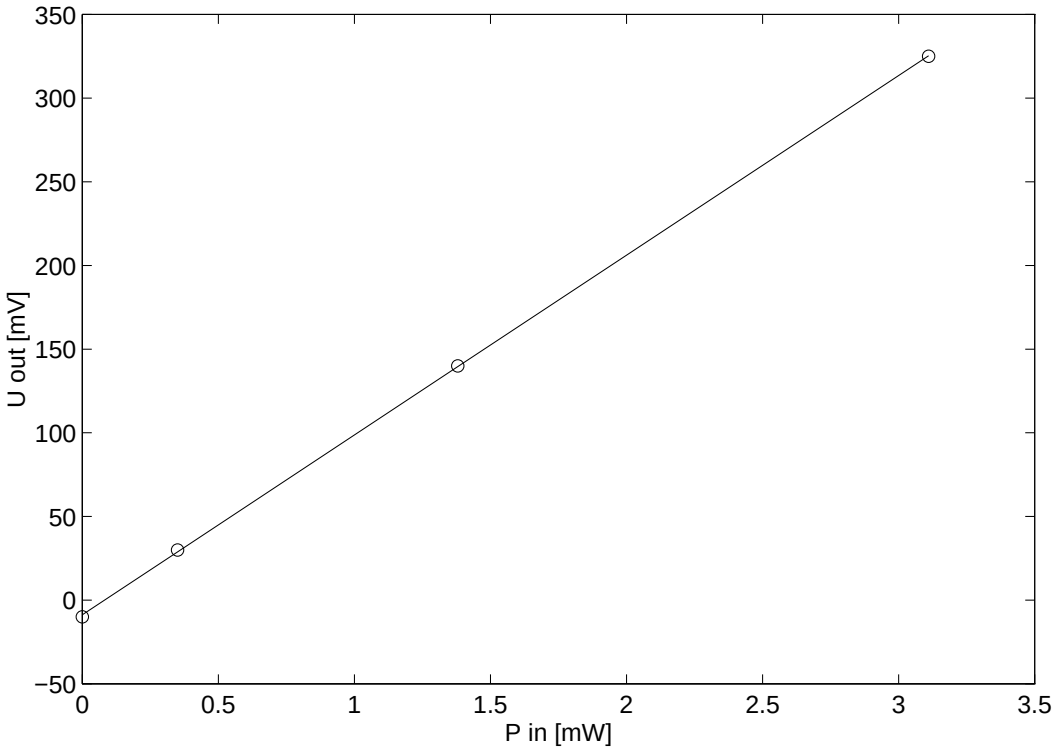

Figure 5.9: Calibration of the photo-acoustic detector with the boxcar integrator as used for measurements at the S-DALINAC facility.

5.2.3 Detector Calibration

The photo-acoustic detector was calibrated as described in Chapter 2. Since the calibration factor depends on the repitition rate of the signal and the read-out electronics, it had to be done under the specific experimental conditions at the S-DALINAC facility. A square wave voltage with a pulse width of 4 ms and a repitition rate of 33 Hz was passed through the foil of the detector. This corresponds to the time structure of the electron beam. The detector signal was read out using the setup used for the measurements with beam. The calibration curve is shown in Fig. 5.9. A fit yields a calibration factor of 107.42 V/W for the given setup. Using this calibration factor, absolute radiation power measurements are possible.

The pyroelectric detector cannot be calibrated this way. If both detectors are used in parallel, this can serve as a cross calibration.

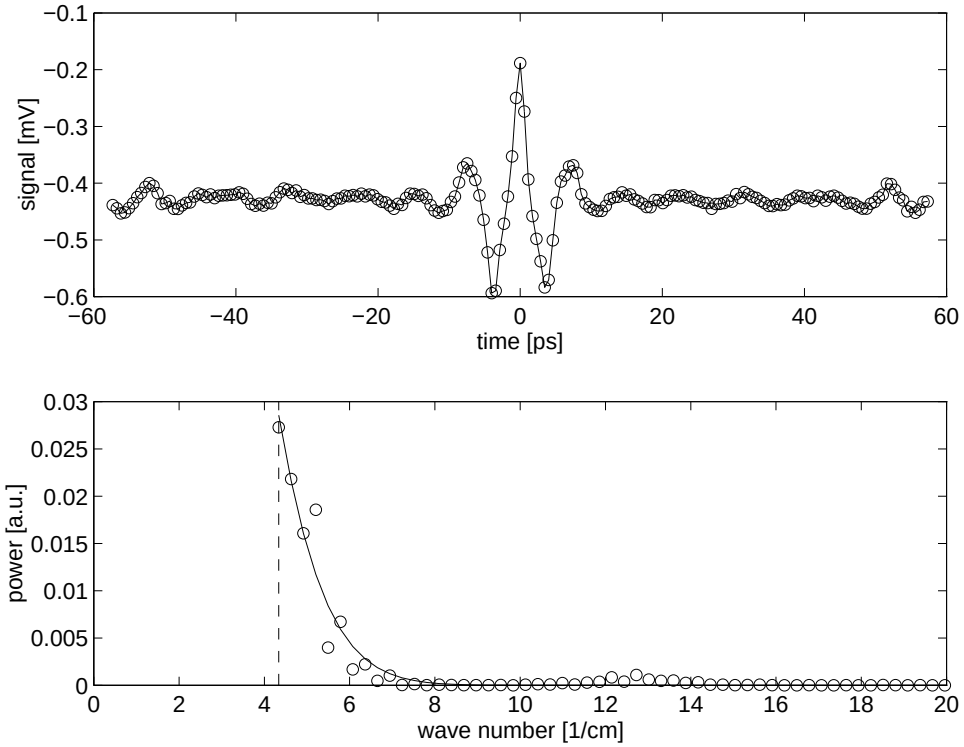

Figure 5.10: Interferometer scan with pyroelectric detector and power spectrum. A Gaussian fit applied to the spectrum yields a bunch length of $\sigma = 2.46$ ps in the time domain.

5.2.4 Measurements with Interferometer

The spectrum of coherent transition radiation was measured using the Martin-Puplett interferometer with both the photo-acoustic detector and the pyroelectric detector. Figure 5.10 shows an interferometer scan with the Martin-Puplett interferometer and the pyroelectric detector. This measurement was done with an average beam current of 3 μA (24 μA during the macropulse), a repitition rate of the macropulses of 31 Hz and a macropulse length of 4 ms. The signal was read out by the boxcar integrator averaging over 5 s for every point. The interferometer scan was done with a stepwidth of 0.17 mm. The total travel distance is 17 mm. The upper plot shows detector output versus travel distance of the movable interferometer mirror, where the optical path length difference is directly transformed into a time difference. The lower plot shows the spectrum calculated from the autocorrelation. A Gaussian fit is performed to the spectrum such that the center is at $\bar{\nu} = 0$ cm^{-1}. The low-frequency cutoff is found at $\bar{\nu} \leq 4$ cm^{-1}. The Gaussian fit is plotted as a solid line. From the Gaussian distribution in the frequency domain, the corresponding Gaussian charge distribution in the time domain can directly be obtained and its sigma be calculated as $\sigma = 2.46$ ps.

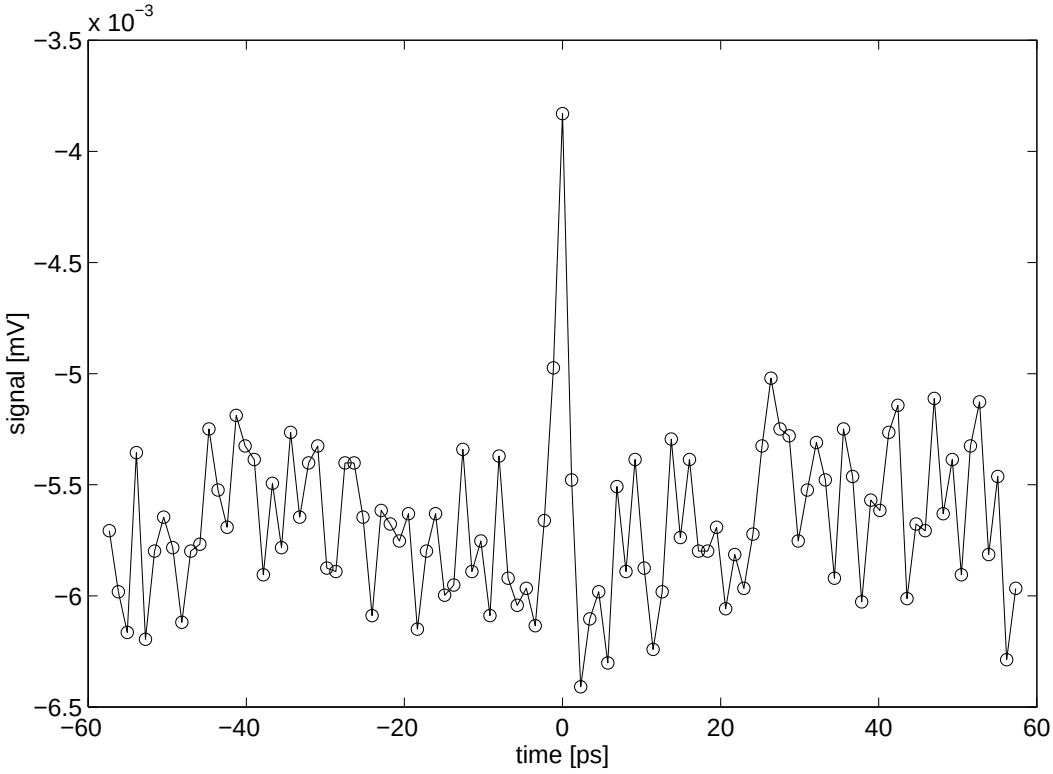

Figure 5.11: Interferometer scan with photo-acoustic detector. Each point is averaged over 60 s. The signal to noise ratio is too bad to obtain information from the spectrum.

The same measurement was done using the photo-acoustic detector. Since the signal to noise ratio is much worse in this case, an average over 60 s for every point was chosen. Since such a measurement takes a long time, the number of points was reduced. Figure 5.11 shows the measured interferogram. The central peak can clearly be seen, but still noise makes spectral analysis impossible.

5.2.5 Comparison of Photo-Acoustic and Pyroelectric Detector

The use of both the photo-acoustic and the pyroelectric detector under the same experimental conditions allows a comparison of the two detector types. The internal response of the P1-45 pyroelectric detector is about 300 V/W[1], which is about a factor of 10^3 higher than the one of the photo-acoustic detector. While the signal output of the pyroelectric detector was in the range of several hundred mV, the signal from the photoacoustic detector was only a few mV. This result is

[1]No calibration is available in the millimeter wavelength range.

consistent with the detector calibration. The signal to noise ratio is much better for measurements with the pyroelectric detector than for those with the photo-acoustic detector.

The photo-acoustic detector, on the other hand, is sensitive to much longer wavelengths than the pyroelectric one. This can be seen from the measured spectra as well as directly from the interferograms. In Fig. 5.10, one sees on both sides of the central peak strong minima. This is an effect caused by the low frequency cutoff of the detector. In Chapter 3 it has been shown for the example of a flat charge distribution how the filter function of the instrument influences the measured autocorrelation. The shape of the autocorrelation function measured with the pyroelectric detector clearly indicates the high-pass filter action fo the detector. For measurements done with the photo-acoustic detector, this effect is less important.

5.3 Measurements at the TESLA Test Facility Linac

5.3.1 The TESLA Test Facility Linac

The TESLA test facility at DESY includes the infrastructure for treatment and test of superconducting cavities as well as a prototype accelerator where the cavities are operated with beam [48]. Figure 5.12 shows the TESLA test facility. In a first stage, the linac is operated with one acceleration module containing 8 cavities. Later, more acceleration modules will be added and the beam energy increased.

The measurements reported here were carried out when the machine was operated with one acceleration module. The electron beam is generated by a thermionic gun. It is electrostatically accelerated and passed through a normal-conducting subharmonic prebuncher which is operated at 216.7 MHz. At an energy of 250 keV, the beam enters the superconducting capture section which consists of a 9-cell cavity operated at 1.3 GHz. The beam is here accelerated to 10 - 12 MeV and obtains its final time structure.

Behind the injector, the beam is injected into the acceleration module. It contains 8 superconducting cavities which provide an average energy gain of about 15 MeV. Behind the acceleration module follows a temporary beamline which leads to a spectrometer dipole. The beam can here be deflected into the high energy experimental area where experiments with the beam can be carried out.

In the configuration with the thermionic gun, a single bunch contains 10^8 particles. The macropulse length is 30 μs and the bunch spacing 4.6 ns. The repetition rate of the macropulses was chosen to 2 Hz. The beam energy after the capture section is about 10 MeV and after the acceleration module typically around 80 MeV.

5.3.2 Experimental Setup

At the TESLA test facility linac, transition radiation targets are installed in the injector part and in the beamline behind the acceleration module. The targets are made from kapton coated with a 20 nm aluminum layer. They can be moved into the electron beam by pneumatic actuators or by stepper motors. While most of the transition radiation monitors are equipped with metal-coated quartz windows, one station was equipped with a non-coated window for the extraction of millimeter waves. For the measurements reported below, the transition radiation target in front of the spectrometer dipole at the end of the linac was used.

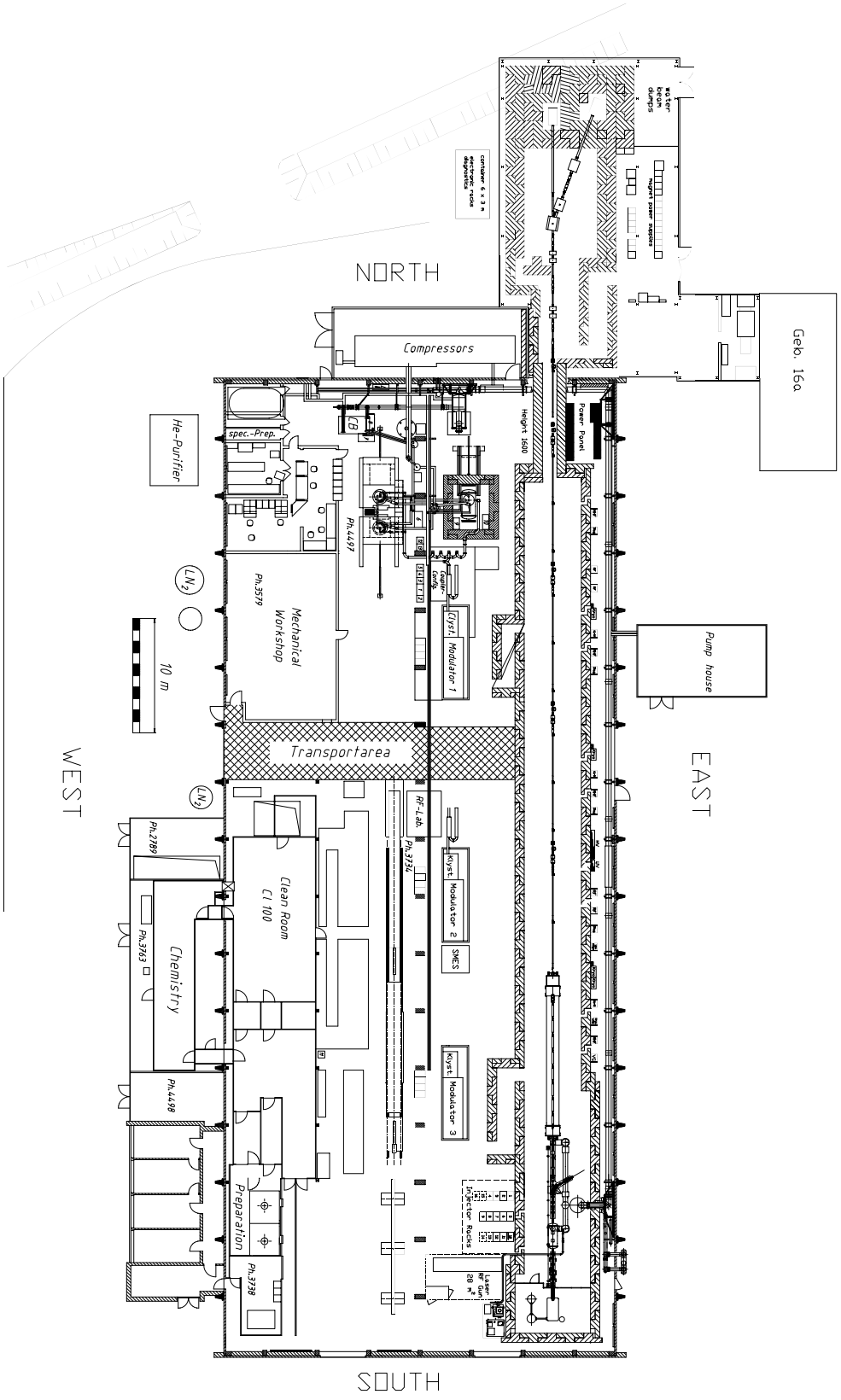

Figure 5.12: Setup of the TESLA test facility at DESY.

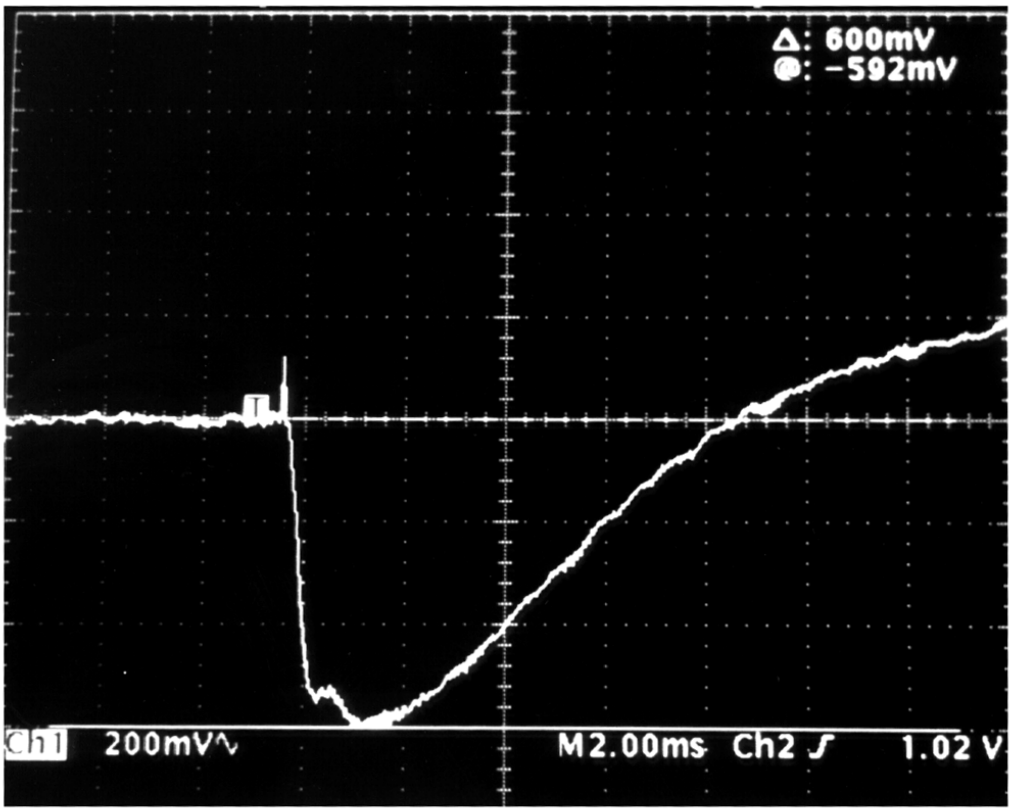

Figure 5.13: Output voltage of the photo-acoustic detector viewed on an oscilloscope.

5.3.3 Observation of Coherent Transition Radiation

Coherent transition radiation was first observed using the photo-acoustic detector without any quasi-optical setup. Figure 5.13 shows the output voltage of the detector viewed on an oscilloscope. The detector output is very sensitive to beam current and bunch length. In order to verify the non-linear behaviour of the radiation power, the beam current was varied and the detector output measured. Figure 5.14 shows the detector output as a funcion of the beam current. The non-linear increase of the radiation power can clearly be observed proving that the signal is indeed due to coherent radiation.

5.3.4 Optimization of Machine Setting

Since the detector output is extremely sensitive to the bunch length, the detector output can be used to optimize the machine to short bunches. The voltage of

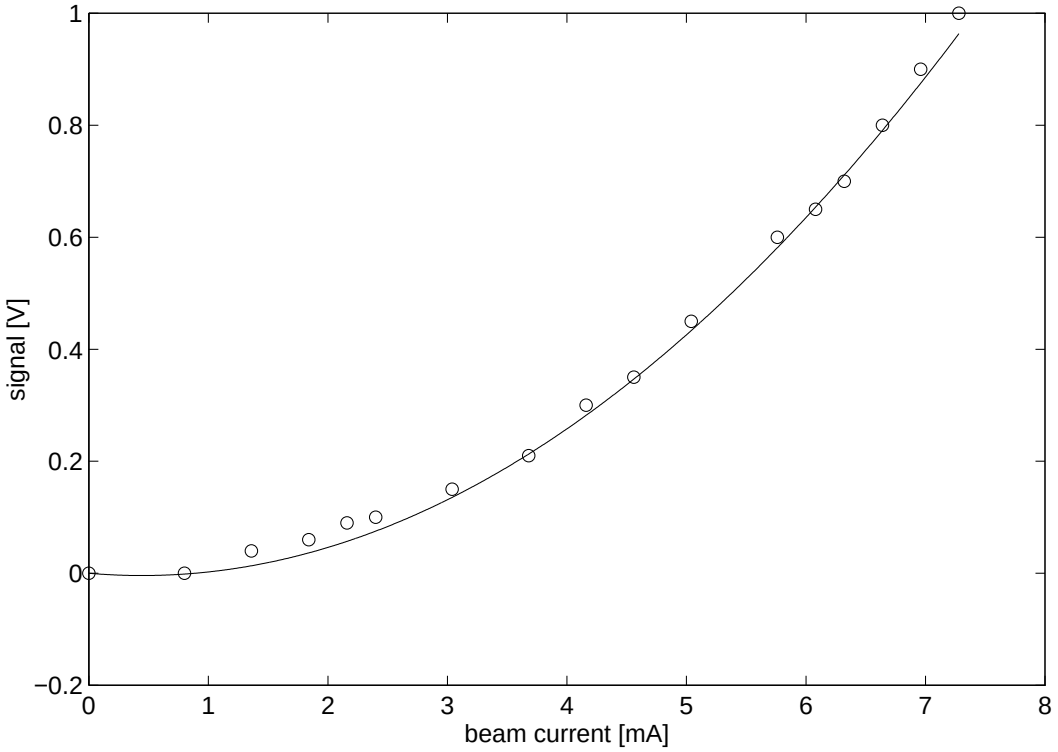

Figure 5.14: Output of photo-acoustic detector versus beam current. The expected non-linear dependence can clearly be seen.

the subharmonic prebuncher was changed in order to minimize the bunch length. The prebuncher is a normalconducting cavity operated at the 6^{th} subharmonic of the accelerating frequency. It is used to compress the bunches coming from the gun from 0.64 ns to 0.1 ns before they are injected into the 1.3 GHz capture cavity. This is done by phase compression, that is the electrons at the head of the bunch are de-accelerated and those at the end of the bunch are accelerated. Phase and amplitude of the buncher cavity can be varied. Figure 5.15 shows the detector output as a function of the prebuncher voltage. While changing the prebuncher voltage had a significant effect on the detector output, it was less sensitive to a change of the phase.

5.3.5 Estimate of Bunch Length from Energy Spread

For the optimized machine setting, the bunch length was estimated from the energy spread. The trajectory of a charged particle through an accelerator can

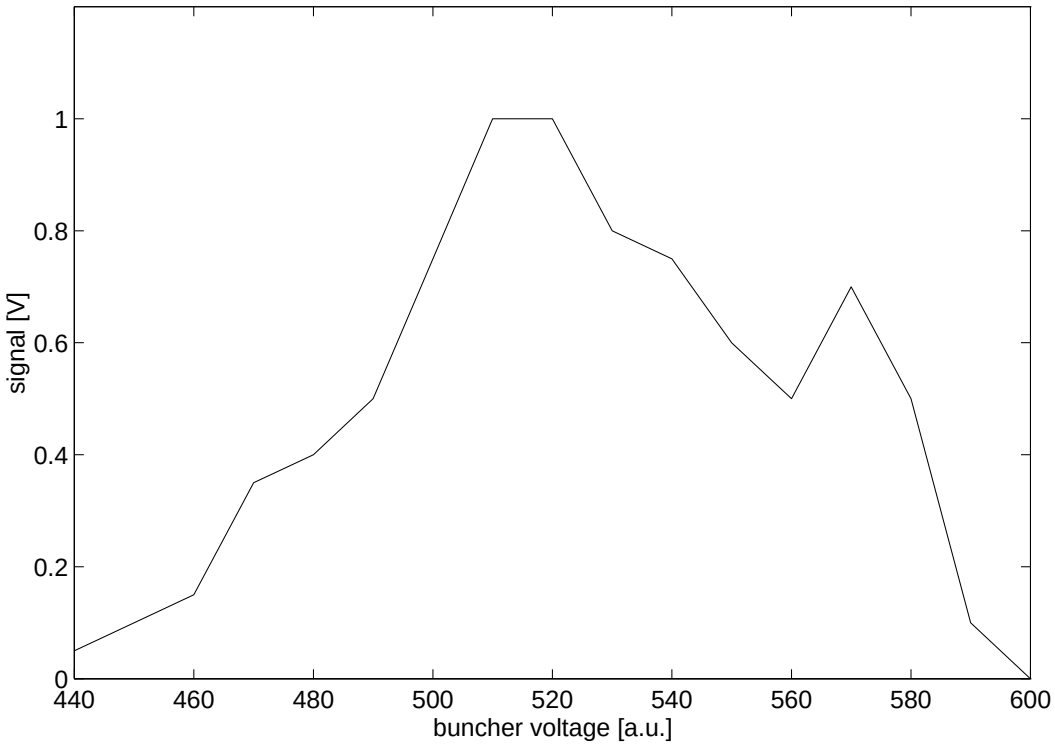

Figure 5.15: Total output of photo-acoustic detector versus buncher setting. At the setting with the shortest possible bunch length, the detector signal has its maximum.

be described using a matrix formalism [49]. At any position, the particle is represented by a vector

$$\boldsymbol{X} = \begin{bmatrix} x \\ \theta \\ y \\ \phi \\ l \\ \delta \end{bmatrix}, \tag{5.1}$$

where x is the horizontal displacement with respect to the central trajectory, θ is the horizontal angle with respect to the central trajectory, y is the vertical displacement with respect to the central trajectory, ϕ is the vertical angle with respect to the central trajectory, l is the path length difference between the particle trajectory and the central trajectory and δ is the energy spread of the beam. The transport of a particle through a part of an accelerator is represented by multiplication with a transport matrix $\mathbf{R}$

$$\boldsymbol{X}(1) = \boldsymbol{R}\boldsymbol{X}(0), \tag{5.2}$$

where $\mathbf{X}(0)$ is the initial coordinate vector and $\mathbf{X}(1)$ is the final coordinate vector of the particle under consideration. We will now examine the beam transport through the acceleration section of a linear accelerator, making the assumption that the particles are ultrarelativistic and that the energy gain is linear. The matrix $\mathbf{R}$ is then given by

$$\boldsymbol{R} = \begin{bmatrix} R_{11} & R_{12} & 0 & \cdots & \cdots & 0 \\ R_{21} & R_{22} & 0 & \cdots & \cdots & 0 \\ \vdots & 0 & R_{33} & R_{34} & 0 & 0 \\ \vdots & \vdots & R_{43} & R_{44} & 0 & 0 \\ \vdots & \cdots & \cdots & 0 & 1 & 0 \\ 0 & \cdots & \cdots & 0 & R_{56} & R_{66} \end{bmatrix} \tag{5.3}$$

We are here only interested in the fifth and sixth row of the transport matrix. The equation following from row five is

$$l(1) = l(0), \tag{5.4}$$

that is the bunch length is not changed by the acceleration section. From row six we obtain an expression for the energy spread:

$$\delta(1) = R_{56} l + R_{66}\delta(0), \tag{5.5}$$

where the elements R_{56} and R_{66} of the transport matrix are given by

$$R_{56} = \left(\frac{\Delta E \sin\phi}{E_0 + \Delta E \cos\phi}\right)\frac{2\pi}{\lambda}, \tag{5.6}$$

$$R_{66} = \frac{E_0}{E_0 + \Delta E \cos\phi}. \tag{5.7}$$

Here, λ is the wavelength of the accelerating field, E_0 is the beam energy before the accelerating section, ΔE is the energy gain in the module and ϕ is the phase lag of the reference particle behind the crest of the accelerating wave.

The energy spread $\delta(0)$ after the injector at 10 MeV and $\delta(1)$ after the acceleration module was measured. From this, an estimate of the bunch length of $\sigma \approx 1$ mm ($\hat{=}$3.3 ps) was obtained.

5.3.6 Measurements with Filter Spectrometer

For the same machine setting, the spectrum of the coherent transition radiation was measured with the filter spectrometer. The filters are moved successively between the photo-acoustic detector and the vacuum window of the transition radiation monitor. The detector output voltage is measured for each filter. The

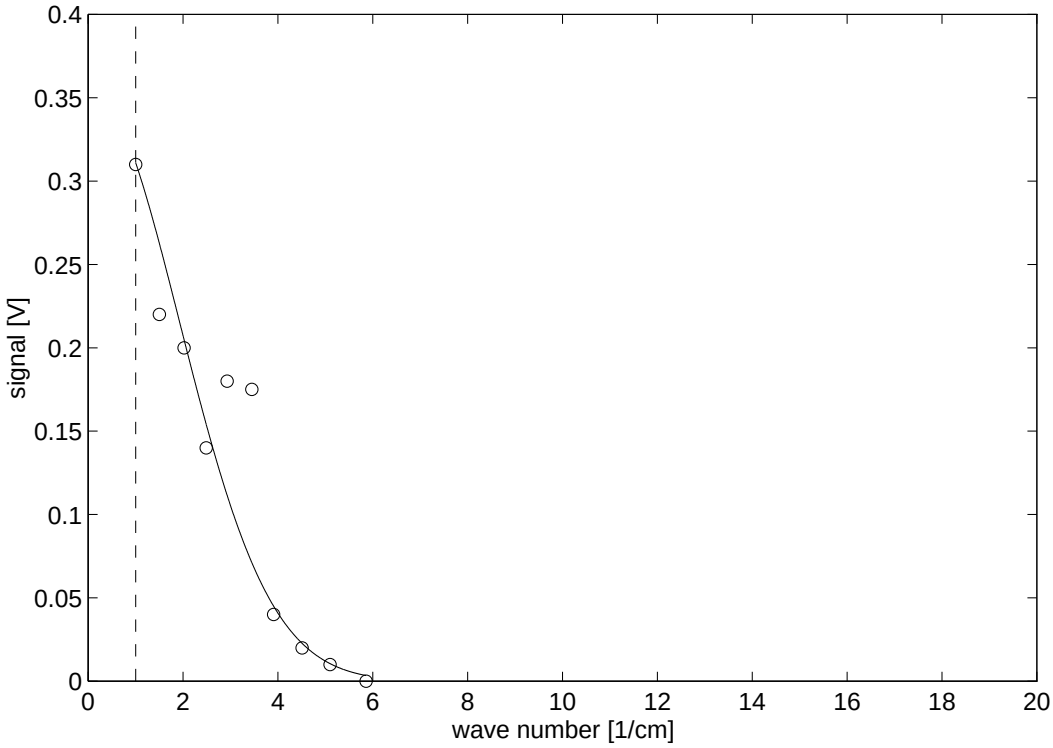

Figure 5.16: Spectrum of coherent tranistion radiation measured with the filter spectrometer. A Gaussian fit applied to the spectrum yields a bunch length of $\sigma = 2.76$ ps in the time domain.

measured value is the integral of the overlap of the known transmission curves of the filter and the radiation spectrum. Figure 5.16 shows the measured spectrum. Since the resolution of such a measurement is limited, an assumption on the bunch shape must be made. A Gaussian charge distribution which results in a Gaussian shape of the spectrum was chosen. From a Gaussian fit applied in the frequency domain, a Gaussian charge distribution in the time domain with $\sigma = 2.76$ ps is obtained. This is in good agreement with the estimate from the energy spread.

5.3.7 Measurements with Interferometer

The autocorrelation of the bunch shape was measured with the Martin-Puplett interferometer. A stepwidth of 25 μm and a total travel distance of the movable mirror of 5 mm were chosen. The mechanical path length difference can directly be transformed in an optical path length difference in terms of picoseconds. Figure 5.17 shows the interferometer scan. Each point was averaged over 30 single

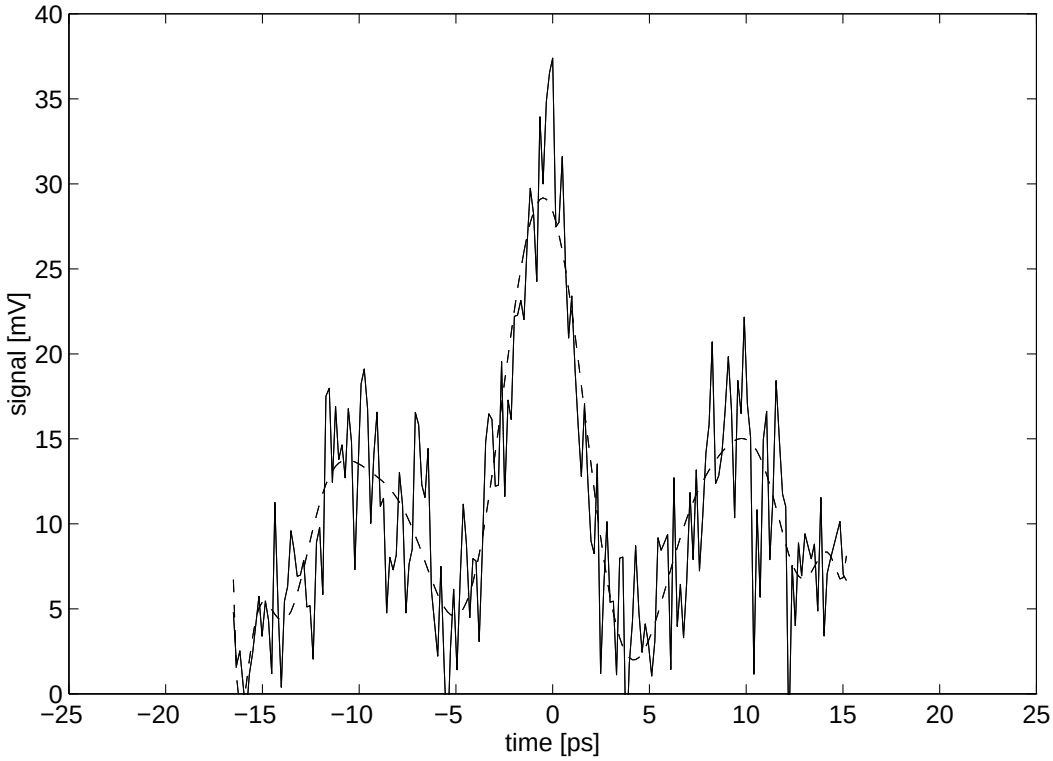

Figure 5.17: Autocorrelation of TTFL bunches. The detector output is plotted versus the optical path length difference of the interferometer arms. The solid line shows the measured data, the dashed line is a ploynomial fit which suppresses high frequent noise.

measurements. The central peak as well as two side minima are clearly seen. In order to suppress the high frequency noise, which is superimposed to the autocorrelation, a polynomal fit of order 16 is applied. The fit is shown as a dashed line in Fig. 5.17.

From the measured autocorrelation function, the spectrum can be calculated. Figure 5.18 shows the power spectrum obtained by applying a Fourier transform to the fitted curve. The low frequency cutoff is found at wave number 3 cm^{-1}. Since the cutoff due to the bandwith of the detector is expected at 1 cm^{-1}, apparently the optical setup itself causes a further limitation due to diffraction or high-pass action of components. Above cutoff, the decay of the first maximum can clearly be seen. A Gaussian fit performed to the first maximum yields a bunch length in the time domain of $\sigma = 2$ ps.

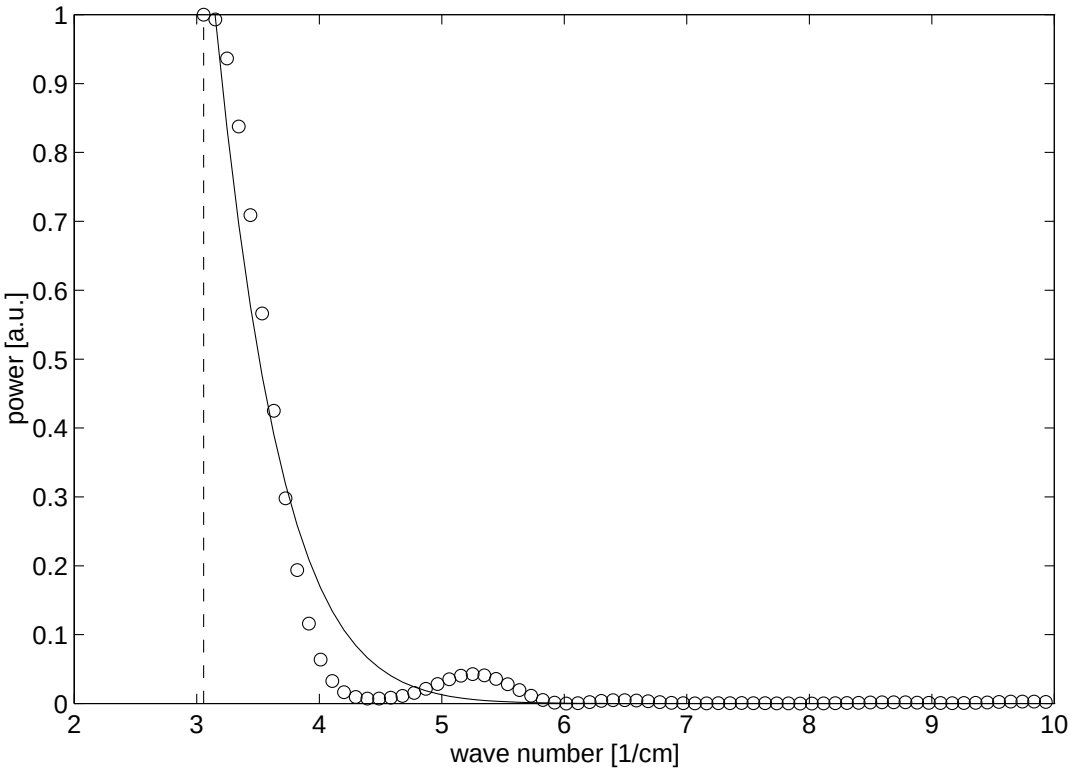

Figure 5.18: Spectrum calculated from the measured autocorrelation. The low frequency cutoff is found at $\bar{\nu} \approx 3$ cm^{-1} (vertical dashed line). The circles represent the data obtained from the Fourier transform, the solid line is a Gaussian fit. Assuming a Gaussian charge distribution, the fit yields $\sigma = 2$ ps.

Conclusion

Transition Radiation was used for diagnostics of electron beams in several linear accelerators. The visible part of the radiation can be used for optical imaging of the beam. To evaluate these techniques, a setup was built in the DESY transport line. First measurements showed that optical transition radiation is a very convenient tool to measure the transverse beam parameters.

To measure the bunch length, the coherent part of the radiation spectrum was used. For picosecond electron bunches, coherent radiation is expected at wavelengths of several millimeters. While similar measurements have been reported at a much shorter bunch length, techniques were developed for the measurement of picosecond bunches.

A photo-acoustic detector was chosen for the detection of millimeter waves. It turned out to work well for measurements of coherent transition radiation. The spectral bandwidth of the detector is wide enough to detect coherent radiation even from bunches of up to 7 ps (rms) length. However, its signal to noise ratio is not very good so that the single bunch charge must be at least 10^8 particles to get a clear detector signal. Acoustical, mechanical and electromagnetic noise as well as X-rays produce noise in the detector output and needs to be suppressed. This requires dedicated amplification, filtering and signal transmission lines.

Complementary to the photo-acoustic detector, a pyroelectric detector was used. Its sensitivity is three orders of magnitude higher than the one of the photo-acoustic detector. On the other hand, the spectral bandwidth is much more limited. In particular, its response for wavelengths longer than 100 μm is not known. It turned out that the pyroelectric detector can actually measure millimeter waves, but its efficiency is not known in that wavelength range. While the photo-acoustic detector is more appropriate to comparatively long bunches of several picoseconds, the pyroelectric detector is clearly more useful for sub-picosecond bunches.

For the use at low electron beam energy, where the large opening angle of the transition radiation does not allow the use of complicated quasi-optical systems, a filter spectrometer was designed and manufactured. It is operated with the

photo-acoustic detector. Its advantage is its simplicity. Measurements with the filter spectrometer can be done quickly. Complementary to Fourier spectroscopy, this is a direct measurement of the coherent spectrum. The resolution of the measurement is limited by the number of filters used. Therefore, such measurements give only an estimate on the bunch length and no information on the bunch shape. Measurements done with the filter spectrometer were compared with measurements in the time domain using a streak camera. The results were found to be in reasonable agreement. The filter spectrometer has therefore proven to give a good estimate on the bunch length.

For precise measurements of the coherent spectrum, a Martin-Puplett interferometer was developed and manufactured. Operated with both a photo-acoustic and a pyroelectric detector, interferograms were measured from which the bunch length could be obtained.

Using the filter spectrometer and the interferometer, the bunch length of the TESLA test facility linac was measured. The results were found in good agreement to an estimate of the bunch length from the energy spread. Measurements in the time domain using a streak camera confirmed the results obtained from the spectroscopic measurements [50].

A new method to measure spectra in the millimeter wavelength range was for the first time used for bunch length measurements [51]. The spectrometer is based on a Josephson junction. It is extremely fast and sensitive and has the potential of a non-destructive, ultrafast measurement of the bunch length. Based on this technology, a new generation of bunch length monitors will be developed [52].

Appendix A

Properties of Millimeter-Wave Materials

The relevant parameters of some millimeter-wave materials are summarized here in form of tables and transmission curves. The data have been taken from [53].

Abbreviations and colloquial names are used for some materials:

TPX	polytetramethylpentane-1
PTFE	polytetrafluorethylene (teflon)
PE	polyethylene
HDPE	high-density polyethylene
LDPE	low-density polyethylene

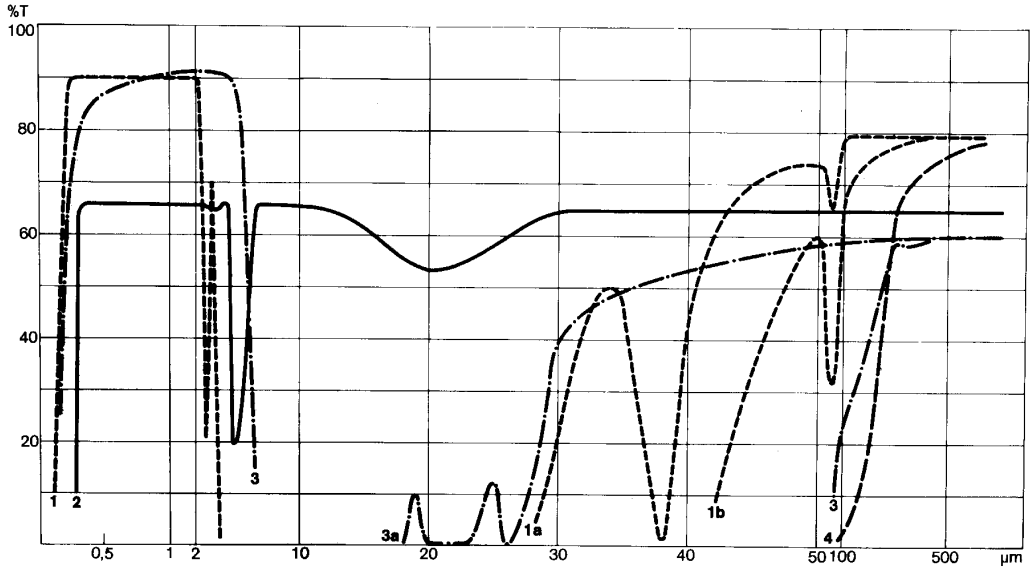

Figure A.1: Transmission of selected window materials. **1**: quartz, crystalline, 10 mm; **1a**: quartz, crystalline, 1 mm, 4 K; **1b**: quartz, crystalline, 1 mm, room temperature; **2**: diamond IIa, 1 mm; **3**: sapphire, 1 mm; **4**: quartz-glass, 1 mm.

material	SiO_2 d = 2 mm	diamond IIa d = 2 mm	Al_2O_3 d = 1 mm	quartz-glass d = 2 mm
transmission range between 50% marks [μm]	0.15 - 4 50 -	0.25 - 2.5 6.5 -	0.17 - 5.5 35 -	0.2 - 4.5 150 -
maximum transmission	90%	65%	90%	90%
reflection losses (2 surfaces)	8.2% (λ = 2 μm)	31.4%	6% (λ = 5 μm)	6.3% (λ = 2 μm)
absorption coefficient [cm^{-1}]			1.9 (λ = 1.9 μm)	
refraction index	1.167	2.41	1.63	1.491
dispersion	1.5×10^{-2}		1.4×10^{-2}	1.5×10^{-2}
density [gcm^{-3}]	2.648	3.52	3.98	2.202

Table A.1: Properties of selected window materials.

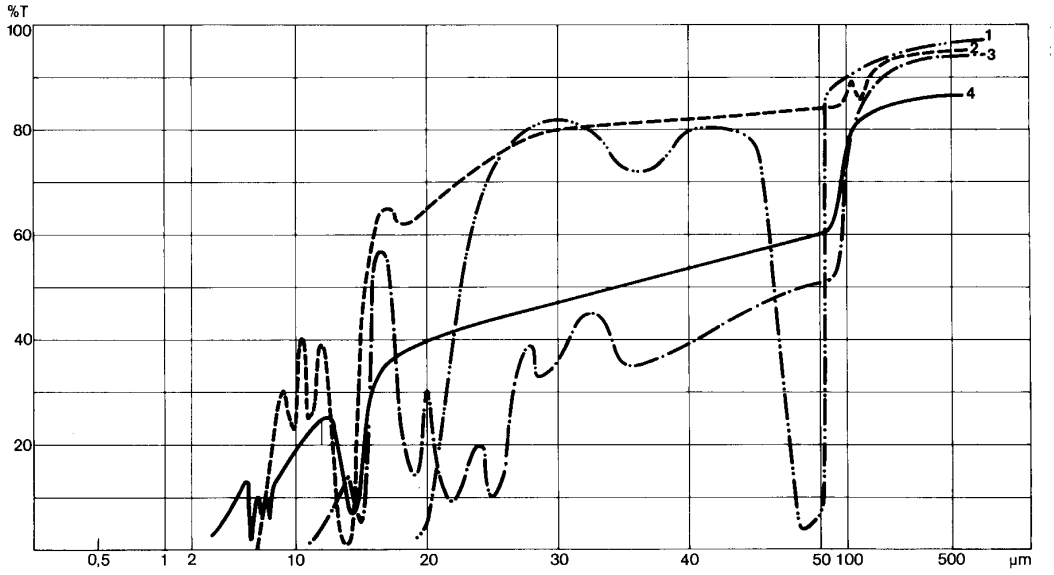

Figure A.2: Transmission of selected window materials. **1**: PTFE (teflon), 0.95 mm; **2**: HDPE, white, 1 mm; **3**: TPX, 3 mm; **4**: PE, black, 0.1 mm.

material	PTFE d = 0.95 mm	PE white d = 1 mm	PE black d = 0.1 mm	TPX d = 3 mm
transmission range between 50% marks [μm]	22 - 47	15 -	34 -	49 -
maximum transmission	$80-95\%$	$>90\%$	85%	$>90\%$
reflection losses (2 surfaces)		9%	6%	
absorption coefficient [cm^{-1}]				
refraction index	1.4	1.52	1.5	1.43
dispersion				
density [g cm^{-3}]	0.9	0.93	0.93	0.83

Table A.2: Properties of selected window materials.

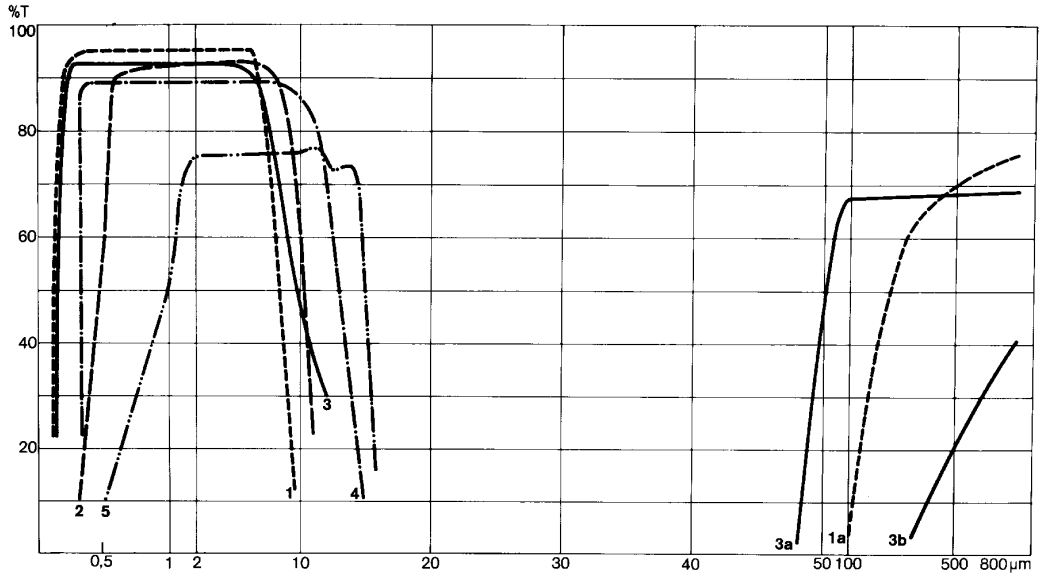

Figure A.3: Transmission of selected window materials. **1**: MgF_2, 2 mm; **1a**: MgF_2, 1 mm; **2**: CdF_2, 5 mm; **3**: CaF_2, 1 mm; **3a**: CaF_2, 1 mm, 4 K; **3b**: CaF_2, 3.5 mm; **4**: PbF_2, 2 mm; **5**: CdS, 2 mm.

material	MgF_2 d=2 mm	CdF_2 d=10 mm	CaF_2 d=1 mm	PbF_2 d=10 mm	CdS d=2 mm
transm. range b. 50% mks. [μm]	0.12 - 8 250 -	0.23 - 9.8	0.12 -12 50 -	0.25 -11	0.5 -15
max. transmission	95%	$>90\%$	$>90\%$	70%	75%
reflection losses (2 surfaces)	4.9% (λ=0.5 μm)	6.0%	5.6% (λ=4 μm)	12% (λ=0.5 μm)	12.9% (λ=1.5 μm)
absorption coefficient [cm^{-1}]	1.4×10^{-2} ($\lambda = 5.25$ μm)		3.5		3×10^{-2}
refraction index	1.23 - 1.38	1.57	1.28 - 1.47	1.62 - 1.78	2.23 - 2.6
dispersion			5×10^{-3} - 4×10^{-2}	2×10^{-2} - 3	
density [g cm^{-3}]	3.18	6.64	3.18	8.24	4.82

Table A.3: Properties of selected window materials.

Appendix B

Electronic Circuits

The following circuit diagrams show the electronics used for the measurements reported.

In detail:
Fig. B.1: amplifier for millimeter-wave detector with integrated MAX263 universal bandpass filter.
Fig. B.2: amplifier for millimeter-wave detector without filter.
Fig. B.3: setup for calibration of photo-acoustic detector.
Fig B.4: setup for transfer of detector signal to control room.

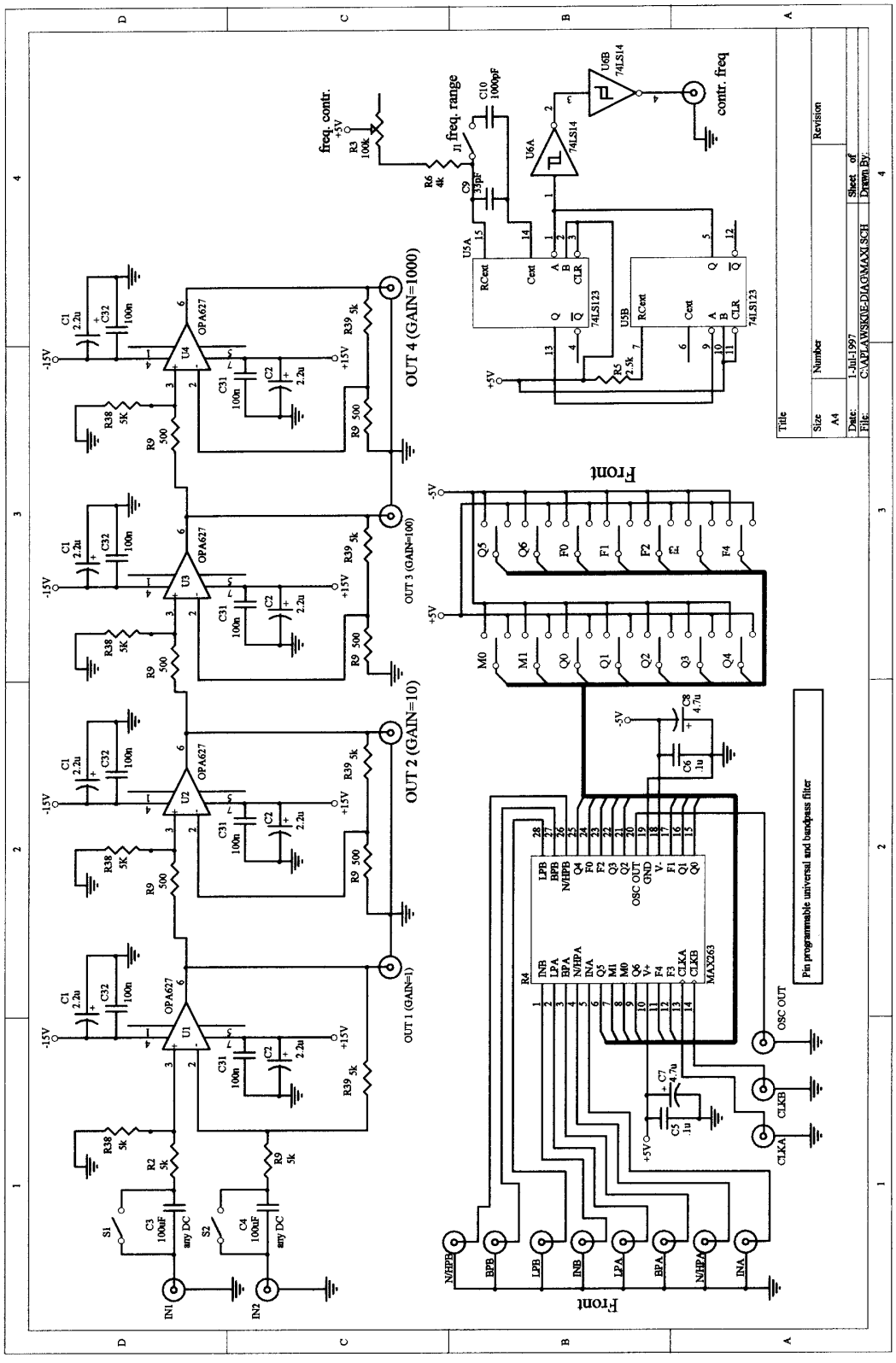

Figure B.1: Amplifier with integrated universal bandpass filter.

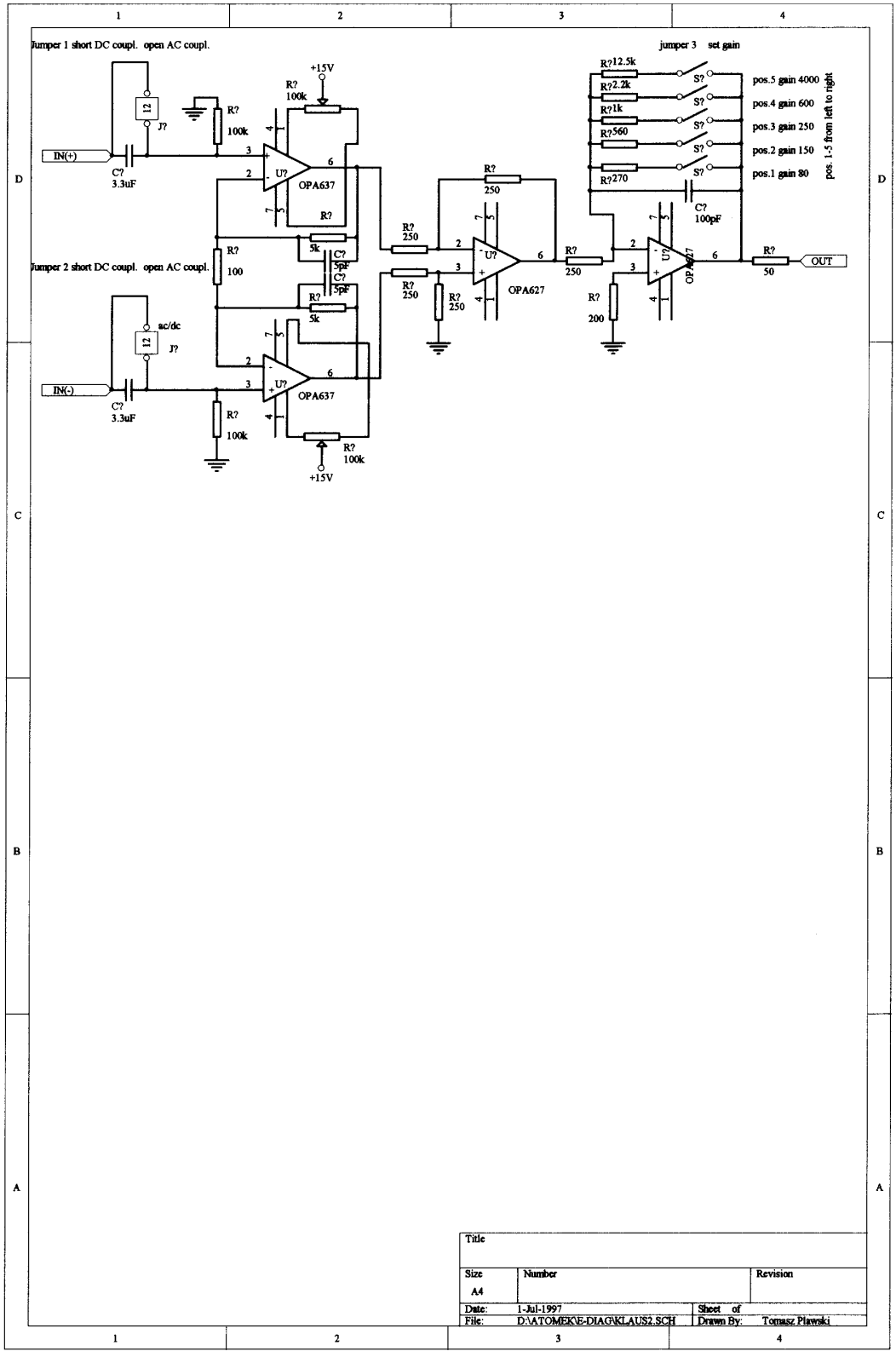

Figure B.2: Amplifier without filter.

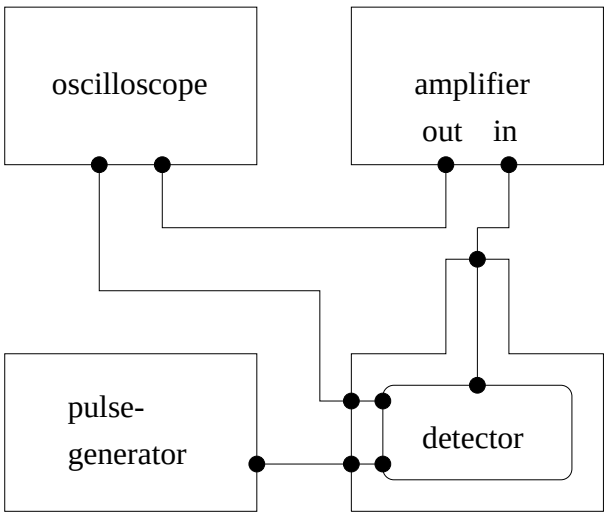

Figure B.3: Block diagram for calibration of the photo-acoustic detector. A square wave current is generated and passed through the foil of the detector. It is monitored on an oscilloscope. The detector output is amplified and monitored on the other channel of the oscilloscope. The calibration procedure is described in Chapter 5.

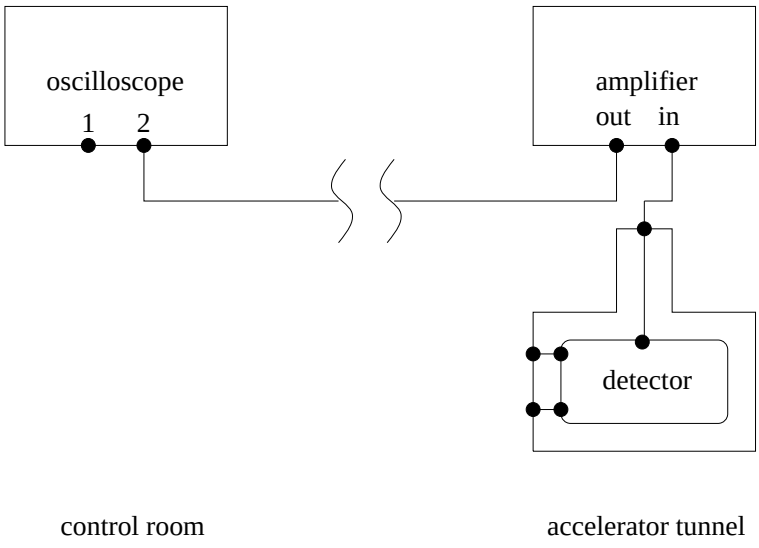

Figure B.4: Block diagram for transfer of the detector signal to the control room. The detector output is amplified in the accelerator tunnel. The analog signal is then passed to the control room via a shielded twisted-pair cable.

References

[1] M. Tigner, *A Possible Apparatus for Electron Clashing-Beam Experiments*, Nuovo Cim. 37, p. 1228 (1965).

[2] R. Brinkmann, G. Materlik, J. Rossbach, A. Wagner (editors), *Conceptual Design of a 500 GeV e^+e^- Linear Collider with Integrated X-ray Laser Facility*, DESY 1997-048.

[3] *A VUV Electron Laser at the TESLA Test Facility at DESY - Conceptual Design Report*, DESY TESLA-FEL 95-03.

[4] J. D. Jackson, Classical Electrodynamics, New York (1975).

[5] V. L. Ginzburg, Applications of Electrodynamics in Theoretical Physics and Astrophysics, Gordon and Breach Science Publishers (1989).

[6] L. D. Landau, E. M. Lifschitz, Lehrbuch der Theoretischen Physik VIII, Berlin (1985).

[7] M. L. Ter-Mikaelian, High-Energy Electromagnetic Processes in Condensed Media, Wiley Interscience, New York (1972).

[8] L. Wartski, *Étude du Rayonnement de Transition Optique produit par des Électrons d'Énergie 30 à 70 MeV. Application aux Diagnostics de Faisceaux de Particules Chargées*, Thesis Université de Paris-Sud (1976).

[9] A. Hofmann, *Theory of Synchrotron Radiation*, SSRL ACD-Note 38 (1986).

[10] A. Hofmann, *Synchrotron Radiation from the Large Electron-Positron Storage Ring LEP*, Physics Reports 64, No. 5 (1980).

[11] C. J. Hirschmugl, M. Sagurton, G. P. Williams, *Multiparticle Coherence Calculations for Synchrotron-Radiation Emission*, Physical Review A, **Vol. 44**, No. 2 (1991).

[12] J. S. Nodvick, D. S. Saxon, *Suppression of Coherent Radiation by Electrons in a Synchrotron*, Physical Review, **Vol. 96**, No. 1 (1954).

[13] E. B. Blum, U. Happek, A. J. Sievers, *Observation of Coherent Synchrotron Radiation at the Cornell Linac*, Nucl. Instr. Meth. A307 (1991).

[14] H. Lihn, D. Bocek, P. Kung, C, Settakorn, H. Wiedemann, *Measurement of Subpicosecond Electron Pulses*, Physical Review E, **Vol. 53**, No. 6 (1996).

[15] Y. Shibata, T. Takahashi, T. Kanai, K. Ishi, M. Ikezawa, J. Ohkuma, S. Okuda, T. Okada, *Diagnostics of an Electron Beam of a Linear Accelerator using Coherent Transition Radiation*, Physical Review E, **Vol. 50**, No. 2 (1994).

[16] R. Lai, U. Happek, A. J. Sievers, *Measurement of the Longitudinal Asymmetry of a Charged Particle Bunch from the Coherent Synchrotron or Transition Radiation Spectrum*, Physical Review E, **Vol. 50**, No. 6 (1994).

[17] H. A. Zahl, M. J. E. Golay, *Pneumatic Heat Detector* , The Review of Scientific Instruments, **Vol. 17**, No. 11 (1946).

[18] Installation and Operating Instructions for the TK TeraHertz Absolute Power/Energy Meter Head , Thomas Keating Ltd.

[19] Molectron Detector Inc., data sheet.

[20] Molectron Detector Inc., calibration certificate.

[21] Spezial-Electronic, data sheet MAX263.

[22] J. M. Lamarre, N. Coron, R. Courtin, G. Dambier, M. Charra, *Metallic Mesh Properties and Design of Submillimeter Filters*, Intern. Journal of Infrared and Millimeter Waves, **Vol. 2**, No. 2, p. 273 (1981).

[23] V. P. Tomaselli, D. C. Edewaard, P. Gillan, K. Möller, *Far-Infrared Bandpass Filters from Cross-Shaped Grids*, Applied Optics, **Vol. 20**, No. 8, p. 1361 (1981).

[24] T. Timusk, P. L. Richards, *Near Millimeter Wave Bandpass Filters*, Applied Optics, **Vol. 20**, No. 8, p. 1355 (1981).

[25] D. W. Porterfield, J. L. Hesler, R. Densing, E. R. Mueller, T.W. Crowe, R. M. Weikle II, *Resonant Metal-Mesh Bandpass Filters for the Far Infrared*, Applied Optics, **Vol. 33**, No. 25, p. 6046 (1994).

[26] D. A. Naylor, R. T. Boreiko, T. A. Clark, *Mylar Beam-Splitter Efficiency in Far Infrared Interferometers: Angle of Incidence and Absorption Effects*, Applied Optics, **Vol. 17**, No. 7, p. 1055 (1978).

[27] K. D. Möller, V. P. Tomaselli, J. Colosi, R. G. Zoeller, *Capacitive-Grid Beam Splitters for Far-Infrared and Millimeter-Wave Interferometers*, Applied Optics, **Vol. 23**, No. 18, p. 3075 (1984).

[28] H.-P. Gemünd, private communication.

[29] J. Lesurf, *Millimetre-Wave Optics, Devices & Systems*, Adam Hilger, Bristol (1990).

[30] F. Keilmann, *Infrared High-Pass Filter with High Contrast* , Intern. Journal of Infrared and Millimeter Waves, **Vol. 2**, No. 2, p. 259 (1981).

[31] A. Roberts, M.L. von Bibra, H.-P. Gemünd, E. Kreysa, *Thick Grids with Circular Apertures: a Comparison of Theoretical and Experimental Performance*, Intern. Journal of Infrared and Millimeter Waves, **Vol. 15**, No. 3, p. 505 (1994).

[32] N. J. Cronin, *Microwave and Optical Waveguides*, IOP Publishing, Bristol Philadelphia (1995).

[33] G. Busse, report on measurements carried out at Institut für Hochfrequenztechnik, Technische Hochschule Braunschweig, not published.

[34] J. Strong, G. A. Vanasse, *Interferometric Spectroscopy in the Far Infrared*, Journal of the Optical Society of America, **Vol. 49**, No. 9, p. 844 (1959).

[35] D. H. Martin, E. Puplett, *Polarised Interferometric Spectroscopy for the Millimetre and Submillimetre Spectrum*, Infrared Physics, **Vol. 10**, p. 105 (1969).

[36] E. Hecht, *Optics*, Addison-Wesley (1974/1987).

[37] Program package Matlab, fast Fourier transform routine.

[38] XYBION ISG-205 gated low-light-level video camera, data sheet.

[39] H. Wiedemann, *Particle Accelerator Physics* , Springer-Verlag Berlin Heidelberg New York (1993).

[40] G. Jacobs, private communication.

[41] K. Hanke, *Measurement of the Bunch Length of LEP with a Streak Camera and Comparison with Results from LEP Experiments*, Diplomarbeit RWTH Aachen, PITHA 94/1 and CERN-SL 95-65 (BI).

[42] F. Tecker, *Evaluation of the Performance of a Streak Camera in Beam Diagnostics at LEP* , Diplomarbeit RWTH Aachen, PITHA 93/7 and CERN-SL 95-66 (BI).

[43] H. H. Braun, K. Aulenbacher, R. Bossart, F. Chautard, R. Corsini, J. P. Delahaye, J. C. Godot, S. Hutchins, I. Kamber, J. H. B. Madsen, L. Rinolfi, G. Rossat, S. Schreiber, G. Suberlucq, L. Thorndahl, I. Wilson, W. Wuensch, *Results from the CLIC Test Facility*, CERN CLIC Note 310 (1996).

[44] K. Aulenbacher, H. H. Braun, F. Chautard, R. Corsini, J. H. B. Madsen, L. Rinolfi, *Bunch Compressor Performances at the CLIC Test Facility*, CERN CLIC Note 307 (1996).

[45] S. Battisti, *Measurement of the Short Bunch Length in the CLIC Test Facility (CTF)*, CERN CLIC Note 211 (1993).

[46] K. Hanke, V. Schlott, K. Aulenbacher, H. H. Braun, F. Chautard, *Beam Diagnostics using Coherent Transition Radiation at the CLIC Test Facility*, CERN CLIC Note 298 (1996).

[47] ARP (now Photonetics), Optoscope streak camera system, data sheet.

[48] D. Edwards (editor), *TESLA Test Facility Linac - Design Report*, DESY TESLA 95-01.

[49] K. L. Brown, D. C. Carey, C. Iselin, F. Rothacker, *Transport - A Computer Program for Designing Charged Particle Beam Transport Systems*, CERN 80-04.

[50] A. Variola, dissertation, in preparation.

[51] Y. Y. Divin, H. Schulz, U. Poppe, N. Klein, K. Urban, V.V. Pawlowskii, *Millimeter-wave Hilbert-transform spectroscopy with high-T_c Josephson junctions* , Appl. Phys. Lett. 68 (11) (1996).

[52] Y. Y. Divin, M. Geitz, K. Hanke, U. Poppe, to be published.

[53] L.O.T. ORIEL, *Eigenschaften optischer Materialien* (1981).

Acknowledgements

In the first place I would like to thank my thesis advisor Prof. Dr. Peter Schmüser for his interest in my work, frequent helpful discussions and his support.

I would like to thank Priv. Doz. Dr. Manfred Tonutti for involving me into accelerator physics. Without his constant support and initiative this thesis would not have been possible.

Priv. Doz. Dr. Martin Leenen introduced me into the TESLA collaboration and helped me to overcome administrative problems.

Amonog all the people from DESY and the collaborating institutes working on the TESLA test facility I would like to point out the help of Dr. Reinhard Bacher, Dr. Donald Edwards, Mark Geitz, Markus Hüning, Matthias Liepe, Lutz Lilje, Dr. Stefan Simrock and Dr. Hans Weise.

I would like to thank Dr. Michele Castellano and Dr. Luciano Catani as well as all the colleagues from INFN Frascati who provided the transition radiation setups for the TESLA test facility which served as a radiation source for the bunch length monitors.

Software problems I discussed with Andre Gössel, Olaf Henseler and Kay Rehlich.

Helpful discussions I had also with Dr. Alexandr Drozhdin, Dr. Adrian Melissinos, Holger Schlarb, Dr. Siegfried Schreiber and Dr. Daniel Schulte.

Dr. Mark Lomperski offered me the chance to take part in experiments with optical transition radiation in the DESY transport line.

I would like to thank Dr. Hans Braun for inviting me to do measurements at the CLIC test facility as well as all members of the CTF group for providing excellent experimental conditions.

The S-DALINAC group supported me a lot during several visits. Namely I would like to point out the help of Dr. Dieter Gräf, Henrik Loos and Dr. Volker Schlott.

For technical support I would like to thank Kurt Escherich, Rainer Fischer, Otto Peters, Tomasz Plawski, Bernd Sarau and Burkhard Sparr.

The workshop of the physics institute IIIA, RWTH Aachen, manufactured several parts of the experimental setup, in particular the high-pass filters.